



THE HONG KONG  
POLYTECHNIC UNIVERSITY

香港理工大學

Pao Yue-kong Library

包玉剛圖書館

---

## Copyright Undertaking

This thesis is protected by copyright, with all rights reserved.

**By reading and using the thesis, the reader understands and agrees to the following terms:**

1. The reader will abide by the rules and legal ordinances governing copyright regarding the use of the thesis.
2. The reader will use the thesis for the purpose of research or private study only and not for distribution or further reproduction or any other purpose.
3. The reader agrees to indemnify and hold the University harmless from and against any loss, damage, cost, liability or expenses arising from copyright infringement or unauthorized usage.

### IMPORTANT

If you have reasons to believe that any materials in this thesis are deemed not suitable to be distributed in this form, or a copyright owner having difficulty with the material being included in our database, please contact [lbsys@polyu.edu.hk](mailto:lbsys@polyu.edu.hk) providing details. The Library will look into your claim and consider taking remedial action upon receipt of the written requests.

**RESEARCH ON STRUCTURE PROPERTY  
RELATIONSHIPS OF MICRO-  
ARCHITECTURED METAMATERIALS**

**YONG ZEHUI**

**PhD**

**The Hong Kong Polytechnic University**

**2018**



---

---

The Hong Kong Polytechnic University

Department of Applied Physics

**RESEARCH ON STRUCTURE-PROPERTY  
RELATIONSHIPS OF MICRO-  
ARCHITECTURED METAMATERIALS**

YONG ZEHUI

A thesis submitted in partial fulfillment of the requirements  
for the Degree of Doctor of Philosophy

August 2016



---

---

## CERTIFICATE OF ORIGINALITY

I hereby declare that this thesis is my own work and that, to the best of my knowledge and belief, it reproduces no material previously published or written nor material which has been accepted for the award of any other degree or diploma, except where due acknowledgement has been made in the text.

\_\_\_\_\_ (Signed)

Yong Zehui (Name of student)



---

---

## ACKNOWLEDGEMENTS

I would like to deeply thank my supervisors, Dr. C.H. Lam, Dr. Y. Wang for their supervision throughout the whole study period.

I would also thank Drs. H. K. Chan, L. L. Shu, D. Y. Lei, L. X. He, B. Li, L. F. Fei, T. Y. Sun, M. Guo, for their invaluable advices on my research. Help from Mr. X Li, R. B. Song, H. J. Fang, C. R. Liu, L. H. Zhang, F. H. Shi, and many other colleagues in the group and the department is also highly appreciated.

I gratefully acknowledge the Hong Kong Polytechnic University for affording me this opportunity to pursue PhD degree at the Department of Applied Physics.

Most of all, I would like to thank my parents for their love, understanding and support throughout the period of my undergraduate and postgraduate studies.



---

---

# TABLE OF CONTENTS

|  |    |
|--|----|
| CERTIFICATE OF ORIGINALITY .....                     | 3  |
| ACKNOWLEDGEMENTS .....                               | 4  |
| TABLE OF CONTENTS .....                              | 5  |
| ABSTRACT.....  | 8  |
| LIST OF PUBLICATIONS .....                           | 10 |
| Chapter 1. Introduction .....                        | 12 |
| 1.1 Composites and Metamaterials .....               | 12 |
| 1.1.1 Introduction to Composite Materials.....       | 12 |
| 1.1.2 Electromagnetic and Optical Metamaterials..... | 14 |
| 1.1.3 Mechanical Metamaterials.....                  | 16 |
| 1.1.4 Terahertz Metamaterials.....                   | 18 |
| 1.1.5 Plasmonic Metamaterials.....                   | 19 |
| 1.2 Scaling Behavior in Metamaterials.....           | 20 |
| 1.3 Ashby Charts.....                                | 23 |
| 1.4 High-throughput Calculation .....                | 25 |
| 1.5 Calculation Methods .....                        | 27 |
| 1.5.1 Finite Element Method.....                     | 27 |
| 1.5.2 COMSOL software package.....                   | 28 |
| 1.5.3 Software Framework.....                        | 29 |



---

---

|   |   |    |
|---|---|----|
| 1.6   | Scope of the present work.....                                    | 30 |
| 1.7   | Statement of original contributions.....                          | 31 |
| Chapter 2. Symmetry Properties of Micro-architected Metamaterials ..... |   | 33 |
| 2.1   | Introduction.....   | 33 |
| 2.2   | Deformation and Stress – Modelling and Analysis.....              | 33 |
| 2.3   | Spherical Representation and Reduced Variables .....              | 36 |
| 2.4   | Results and Discussion .....                                      | 39 |
| 2.5   | Summary.....  | 43 |
| Chapter 3. Scaling Behavior in Micro-architected Metamaterials.....     |   | 44 |
| 3.1   | Introduction.....   | 44 |
| 3.2   | Theory and Method for Obtaining Effective Property .....          | 45 |
| 3.2.1   | Strain and Stress Tensors.....                                    | 45 |
| 3.2.2   | Elastic theory for continuous anisotropic media.....              | 49 |
| 3.2.3   | Piezoelectric theory for continuous anisotropic media.....        | 51 |
| 3.2.4   | Boundary Condition Assignments and Constant Extraction.....       | 53 |
| 3.2.5   | Dataset.....  | 55 |
| 3.3   | Scaling behavior of elastic properties .....                      | 56 |
| 3.3.1   | Young’s Modulus and Shear Modulus .....                           | 57 |
| 3.3.2   | Poisson’s Ratio and Anisotropy Factor .....                       | 61 |
| 3.4   | Scaling behavior of dielectric and piezoelectric properties ..... | 63 |
| 3.4.1   | Poling Directions .....   | 64 |



---

---

|                  |   |            |
|------------------|---|------------|
| 3.4.2            | Dielectric Properties.....                                      | 65         |
| 3.4.3            | Piezoelectric constants .....                                   | 66         |
| 3.5              | Appendix: scaling behavior of other relative parameters.....    | 69         |
| 3.6              | Summary.....  | 72         |
| Chapter 4.       | Terahertz Properties of Piezoelectric-based Metamaterials ..... | 73         |
| 4.1              | Introduction.....   | 73         |
| 4.2              | Terahertz Characterization of PMN-PT .....                      | 75         |
| 4.3              | Estimation of Terahertz Properties for PMN-PT Sample.....       | 79         |
| 4.4              | Summary.....  | 83         |
| Chapter 5.       | Optical Properties of Metal-based Metamaterials .....           | 85         |
| 5.1              | Introduction.....   | 85         |
| 5.2              | Multi-polar plasmonic modes in nanorod-type metamaterials.....  | 87         |
| 5.3              | Sensitivities of quadrupole resonances .....                    | 91         |
| 5.4              | Linewidth of quadrupole resonances .....                        | 93         |
| 5.5              | FOM (figure of merit) of quadrupole resonances .....            | 96         |
| 5.6              | Summary.....  | 97         |
| Chapter 6.       | Conclusion and future work .....                                | 99         |
| 6.1              | Conclusion .....  | 99         |
| 6.2              | Future work.....  | 101        |
| <b>REFERENCE</b> | .....   | <b>102</b> |



---

---

## ABSTRACT

Metamaterials is a type of artificial materials with properties that cannot be found in nature while gaining their properties from structure rather than composition. During the last decade, studies on metamaterials have extended from electromagnetics all the way to the fields of optics, ultrasonics, mechanics, etc. Their potential applications have been found in various industries such as wave tuning/filtering in communication, medicine, remote sensing, detection, cloaking in military guise, radiation or sound shielding, etc. In particular, the application of metamaterial in structural material designs can result in superior properties such as ultralight weight with ultrahigh stiffness, negative Poisson's ratio, for engineering uses in extreme environment.

This thesis focused on micro-architected metamaterials with an emphasis on the investigation of structure-property relationships of a wide range of physical properties including elastic, dielectric, piezoelectric as well as optical properties. Based on an understanding of the symmetry and scaling behavior of the metamaterials, some designs of metamaterials with superior properties such as high piezoelectric response, high Terahertz or optical sensitivity have been achieved. The research was mainly conducted by numerical simulation. Tools for solving the mechanical as well as the optical problems include the finite element method (FEM) using a commercial software package COMSOL, and a high-throughput calculation software framework coded with Matlab.

Some interesting results obtained in the research are detailed as follows. First, the



---

---

symmetry types of the six designed models were analyzed by applying Euler rotations to the calculated elastic tensors, from which very different anisotropic properties for the models were identified. The elastic tensors of the metamaterial designs were found to exhibit a higher degree of symmetry than that of the geometry. Second, the scaling behavior of the elastic, dielectric and piezoelectric metamaterials compared with their relative density were systematically studied, from which different scaling behavior such as “stretching-dominated”, “bending-dominated” and “immediate” type have been identified. There also exist some physical properties that do not conform to the scaling law, such as Poisson’s ratio  $\nu$ , and the piezoelectric constant  $d_{33}$ , while a super-high  $d_{33}$  of 400 has been found for the helix-network model. Third, the terahertz properties of the piezoelectric substrate PMN-PT have been experimentally characterized, from which we have fabricated metamaterial patterns and tuned the dielectric properties of the meta-surface, which can alter the THz responses by 12%. Fourth, quadrupole resonances in gold nanorod metamaterials have been found to enhance the sensing figure of merit by 82 compared to the conventional dipole type resonances, which may find potential application in high sensitive micro-assays.



---

---

## LIST OF PUBLICATIONS

1. Z. Yong, L. Shu, H. K. Chan, C. H. Lam, and Y. Wang, Symmetry and Scaling Behavior of Elastic, Dielectric and Piezoelectric Properties of Micro-architected Metamaterials, in preparation.
2. Z. Yong, L. Shu, H. K. Chan, C. H. Lam, and Y. Wang, Scaling Behavior of Mechanical Strength Properties of Micro-architected Metamaterials, in preparation.
3. Z. Yong, L. Shu, H. K. Chan, C. H. Lam, and Y. Wang, Scaling Behavior of Irregular-Shaped Micro-Architected Metamaterials, in preparation.
4. Z. Yong, D. Lei, C. H. Lam and Y. Wang, Ultrahigh Refractive Index Sensing Performance of Plasmonic Quadrupole Resonances in Gold Nanoparticles, *Nanoscale Res. Lett.*, **9**, 1 (2014).
5. Z. Yong, L. He, B. Li, M. Hu, C. H. Lam and Y. Wang, Terahertz Time-Domain Spectroscopy of  $0.73\text{PbMgNbO}_3\text{-}0.27\text{PbTiO}_3$  Single Crystal, *J. Am. Ceram. Soc.*, **97**, 1696 (2014).
6. L. Shu, Z. Yong, X. Jiang, Z. Xie, Flexoelectricity in Low Densification Materials and Its Implication. Submitted to *J. Alloys and Compounds*.
7. L. Fei, Y. Hu, Z. Yong, W. Lu and Y. Wang, Evidencing the structural Conversion of Hydrothermal-Synthesized Titanate Nanorod by in-situ Electron Microscopy. Submitted to *ACS Nano*.



- 
8. T. Sun, L. Sun, Z. Yong, H. L. W. Chan and Y. Wang, Estimation of the magnetoelectric coefficient of a piezoelectric-magnetostrictive composite via finite element analysis. *J. Appl. Phys.* **114**, 027012 (2013).
  9. M. Guo, Z. Yong, K. Xie, J. Lin, Y. Wang and H. Huang, Enhanced light harvesting in dye-sensitized solar cells coupled with titania nanotube photonic crystals: a theoretical study. *ACS Appl. Mater. Inter.* **5**, 13022 (2013).
  10. M. Guo, H. Sun, J. Zhang, L. Liu, N. Fu, Z. Yong, H. Huang and K. Xie, Broadband and omnidirectional light harvesting enhancement in photovoltaic devices with aperiodic TiO<sub>3</sub> nanotube photonic crystal. In preparation.



# Chapter 1. Introduction

## 1.1 Composites and Metamaterials

### 1.1.1 Introduction to Composite Materials

The history of composite material research is far longer than that of metamaterials. However, some important properties, or laws that governs the physics of metamaterials have already been studied long ago when they were thought of merely composite materials [1]. Figure 1-1 gives a summary of the classifications of binary composite materials. In particular, binary composites can generally be divided into two groups, one is the “structure-air composite”, which means the composite is made of one main material as the dominating part but with voids filled with air inside it; the other is the “matrix-inclusion composite”, which means the composite is made of two types of materials, one being the main part, and the other being included in the matrix.

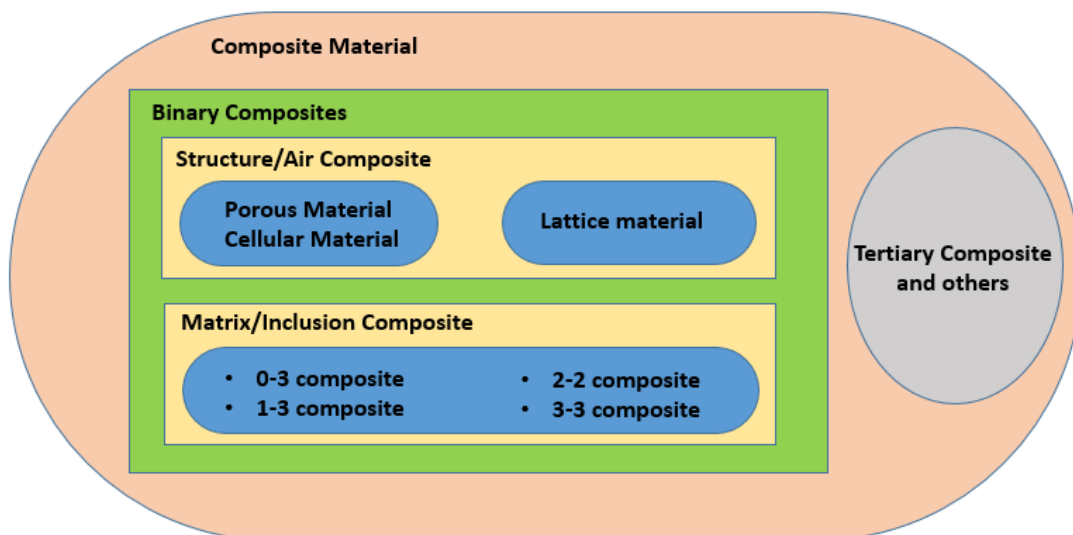


Figure 1-1. A summary of the classifications of binary composite materials.



Along the discovery of natural composites and the invention of artificial composites, different terminologies have been used. Aerogels, fiber networks, and porous or cellular materials are types of “structure-air” composites, while lattice materials is a special subcategory of cellular materials possess a spatial periodicity, resembling that of atomic crystals [2-5].

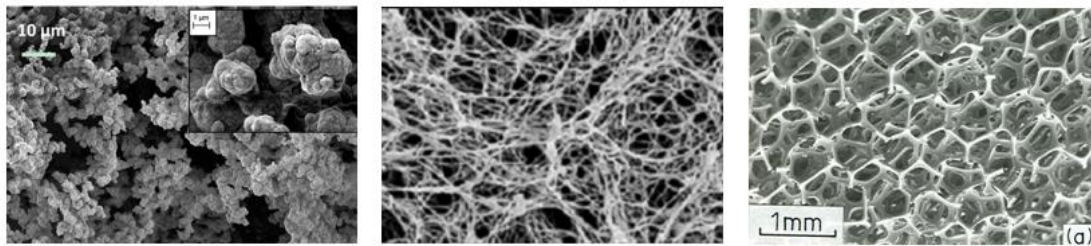


Figure 1-2. Three kinds of natural structure-air type composites, the aerogels (Left), the fiber networks (Middle), and the cellular solids (Right). (Reprinted from Ref. [2]).

Another taxonomy is to divide composites (generally two phase composites, or “matrix-inclusion” combination) by their connectivity, as 0-3 (particulates), 1-3 (fiber-reinforced), and 2-2 (laminated), 3-3 (interpenetrated) types. 0-3 materials would become porous materials if the inclusion constituents are replaced by air, from which various effective medium theories have been developed to evaluate the property of such composites [4-7]. The term “metamaterial” has been now widely used whenever the author is emphasizing the special structure that is employed, no matter for ordered, disordered, or quasi-ordered materials.

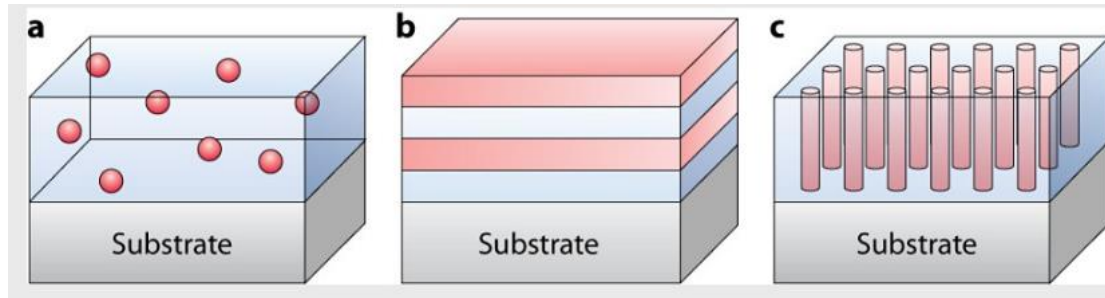


Figure 1-3. Composites with (a) 0-3 type, (b) 2-2 type, and (c) 1-3 type. (Reprinted from Ref. [5])

## 1.1.2 Electromagnetic and Optical Metamaterials

“Metamaterials” is a newly emerged term from the 2000s used to denote artificial materials with properties that do not exist for natural materials [8-15]. They have found applications for their electromagnetic all the way to mechanical properties. Classified by different types of their physical properties, metamaterials are usually referenced to “electromagnetic metamaterials”, “optical metamaterials”, “sonic metamaterials”, “ultrasonic metamaterials”, or “mechanical metamaterials”, etc. Historically, the first ever metamaterial created is a metallic rod/split-ring composite, fabricated in 2001 by Shelby *et al*, which shows negative refractive index at the microwave range [8]. Later, Pendry *et al* have theoretical predicted the cloaking device, which has been subsequently realized by Schurig *et al* at microwave frequencies [9, 10]. Fabrication of these kinds of metamaterials often only requires simple plating and etching to be done. The sizes of them range from centimeters down to hundreds of micrometers, which can only work at microwave frequencies, as shown in Figure 1-4.

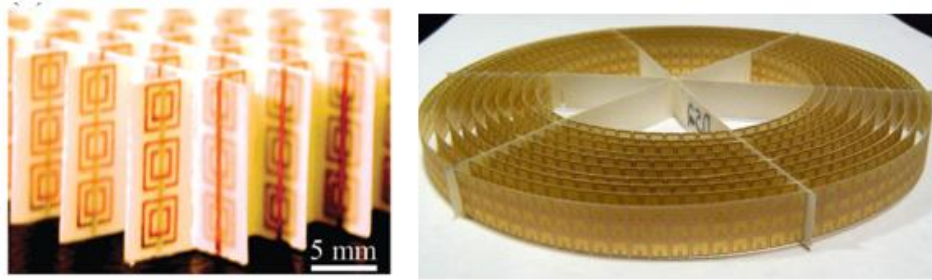


Figure 1-4. Electromagnetic metamaterials with negative refractive index, and cloaking functions at microwave frequencies. (Reprinted from Ref. [8-10])

Using some advanced nanofabrication technology, nano-sized negative index metamaterials that can work in visible light range were produced in 2007, by Shalaev *et al* [11]. In that work they have employed a technology of layer-by-layer nanolithography to implement a 3-D grid design. Cloaking at visible light range is also achieved in 2007 by Valentine *et al* [12]. Another noteworthy work is the realization of a chiral metamaterial made by nano-springs that can manipulate the polarization of light. These metamaterial designs are all shown in Fig. 1-5.

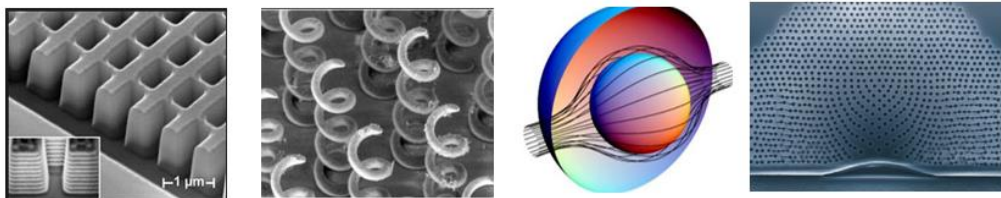


Figure 1-5. Optical metamaterials with negative refractive index, chirality and cloaking functions. (Reprinted from Ref. [11-13])

Meanwhile, Fang *et al* (2006) have designed a type of Helmholtz ring to enable negative modulus for ultrasound waves, which are called “ultrasonic metamaterials” [13]. Zhang *et al* (2011) have made broadband ultrasound cloaks [14]. Burek *et al* have invented a kind of opto-mechanical metamaterials, which can perform coupling between light and micro-vibrations [15].

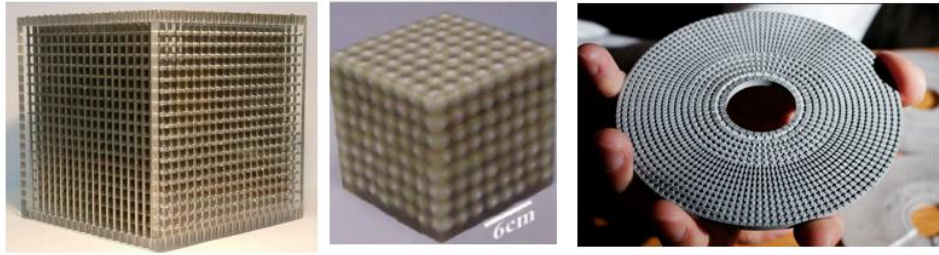


Figure 1-6. Ultrasonic metamaterials with negative refractive index, and cloaking functions. (Reprinted from Ref. [12])

### 1.1.3 Mechanical Metamaterials

Mechanical metamaterials refer to materials with certain mechanical properties (including Young's modulus, yield strength, Poisson's ratio, etc.) defined by their geometry rather than composition (including pores, trusses, and other microstructure). A lot of intriguing properties such as ultralight weight, ultrahigh stiffness, and negative Poisson's ratio etc., have been discovered, accompanied with promising application prospects in the fields of aeronautics, transportation, energy absorption, heat exchange and structural components of other industries [16-20].

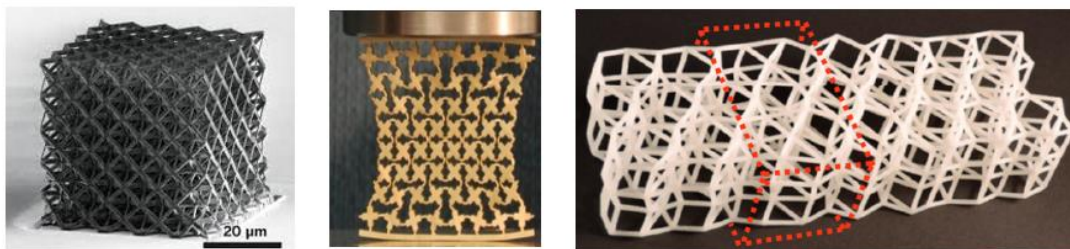


Figure 1-7. Metamaterials with ultrahigh stiffness, negative Poisson's ratio, and buckling-resistant properties. (Reprinted from Ref. [16-18])

The first groundbreaking work on mechanical metamaterials was reported in 2011 by Schaedler *et al*, who use nano-sized nickel hollow tubes in an octet-truss lattice, which displays super high stiffness and super lightweight and can be supported by a dandelion. In 2013, Cheung *et al* have designed a reversible joint cuboct lattice using



carbon reinforced polymers, which can achieve super-high elasticity and with super-high stiffness. In 2014, Bauer *et al* have fabricated 5 types of mechanical metamaterials, and compare them by their elastic and strength properties. Meza *et al* have fabricated by an aluminum version of Schaedler's structure using alumina hollow tubes. Zheng *et al*, have fabricated and compared the difference between bend-dominated and stretch-dominated structures. These structures have been predicted to have potential application in aeronautics, transportation, medical devices, etc.

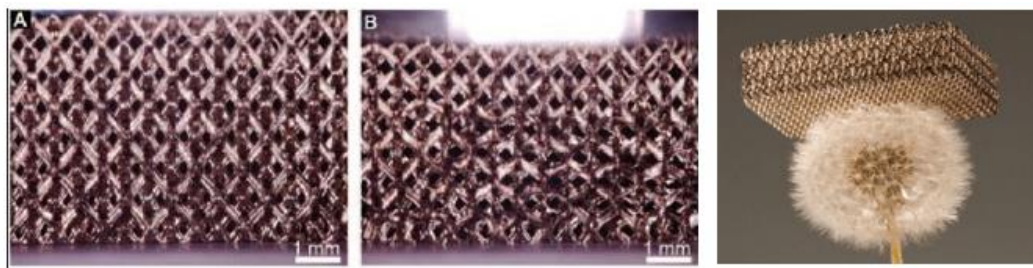


Figure 1-8. An octet-truss type mechanical metamaterial fabricated with nickel hollow tubes. (Left) The unloaded metamaterial, (Middle) the metamaterial under pressure, and (Right) the structure standing on a dandelion. (Reprinted from Ref. [19])

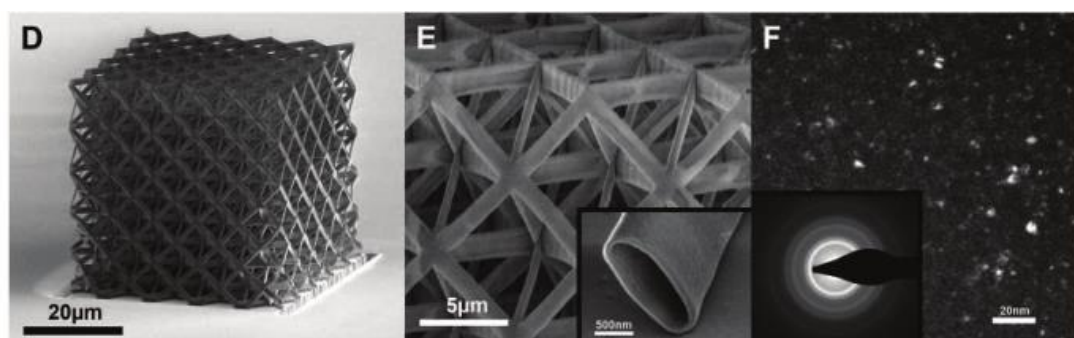


Figure 1-9. An octet-truss type mechanical metamaterial made of alumina hollow tubes. (Left) EM image of alumina octet-truss metamaterial. (Middle) Zoomed-in image of the alumina octet-truss nanolattice. (Right) TEM dark-field image with diffraction grating of the alumina nanolattice tube wall. (Reprinted from Ref. [20]).



### 1.1.4 Terahertz Metamaterials

Terahertz is a relatively unexploited electromagnetic frequency range (from 0.3THz to 3THz) that is promising for future applications in various fields of medical imaging, security, communication, manufacturing, etc. However, up to date, there still lacks tools which are required to construct devices operating within this range. Therefore, techniques to manipulate and control Terahertz waves are in large demand. metamaterials are perfect candidates to undertake the role of wave tuning and modeling. In 2006, Chen *et al* have invented an active metamaterial device that can control and manipulate THz radiation in real-time. The device involves an array of electric resonators (split-ring type metamaterial) deposited on a GaAs substrate. The two parts together can enable Terahertz modulation by a percentage of 50, an order of magnitude enhancement over previous devices.

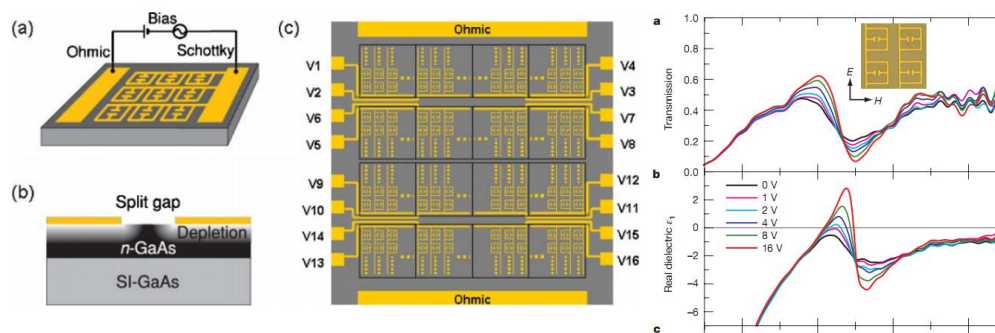


Figure 1-10. (Left) Design of the active THz metamaterial device. (Middle) Design of metamaterial-based THz modulator. (Right) Switching performance of the Terahertz metamaterial device. (Reprinted from [23])



## 1.1.5 Plasmonic Metamaterials

Plasmonic metamaterials is a group of optical metamaterial that mainly include nano-sized metals, including different forms such as nano-particles, nano-rods, nano-wires and so on. In these cases, we normally take the nanoparticles as light scatterer, where light incident on them will often excite a coupling between light itself and the electron motions inside the metal, often called surface plasmons, as shown in Figure 1-11. This excitation will absorb light energy at specific wavelength, due to the internal resistivity of metal as well as the resonance size of the metal geometry.

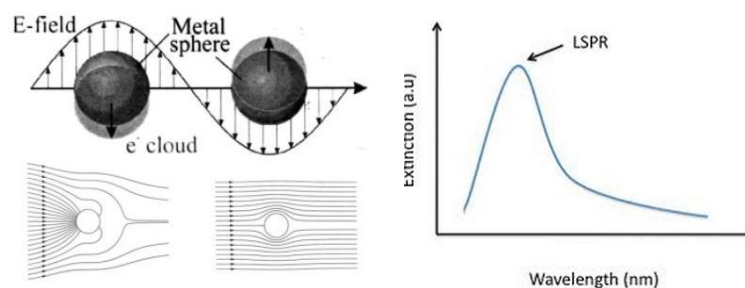


Figure 1-11. (Left) Excitation of surface plasmons. (Right) Light extinction peak. (Reprinted from [24])

The most important application of surface plasmon is to enhance the optical sensitivity of a substrate when the refractive index of that substrate will change under attachment or detachment of specific molecules (Figure 1-12). By tuning the metallic pattern on the substrate, or equivalently, tuning the metamaterial type, the sensitivity of the device will change a lot. Aside from forming metallic pattern on the substrate, there also exists simple method — to synthesis metallic nanoparticles and distribute them onto the substrate in a disordered way (as shown in Figure 1-13). This method is inexpensive and can also achieve good sensing performance.

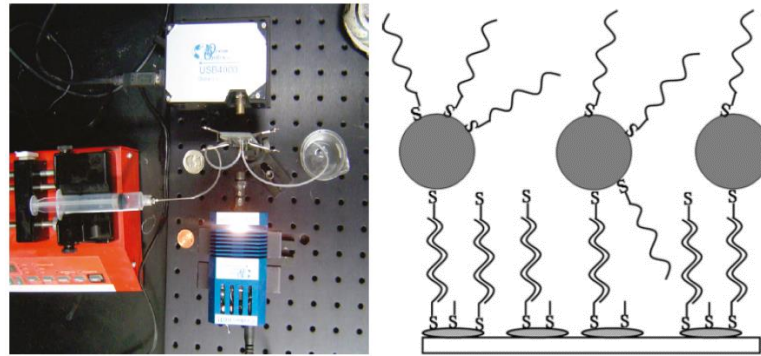


Figure 1-12. (Left) Microfluidic system using plasmonic biosensor. (Right) The mechanism of sensing. (Reprinted from [26]).

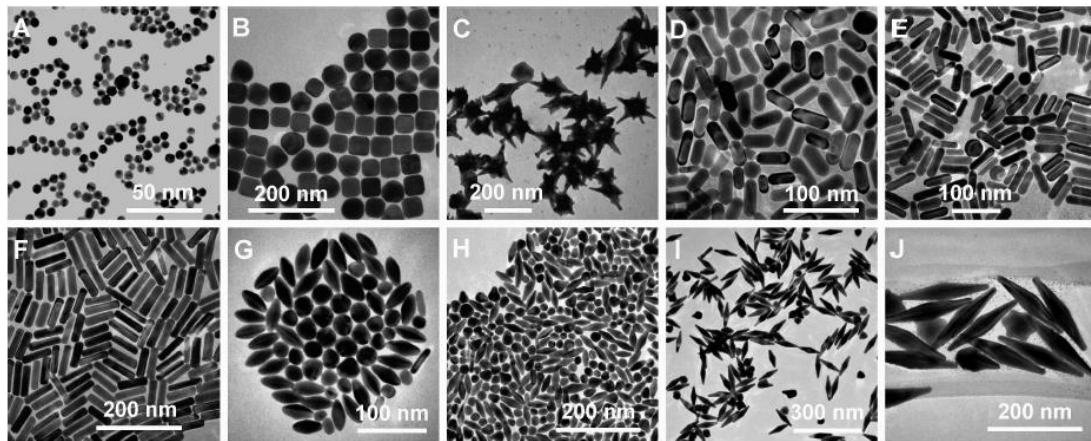


Figure 1-13. Various types of metallic nanoparticles for surface plasmonic sensing. (Reprinted from [27]).

## 1.2 Scaling Behavior in Metamaterials

Scaling laws, with the form shown in Eq. (1-1)

$$F \sim A\rho^\alpha \quad (1-1)$$

can be observed in a diversity disciplines including physics, biology, and even social sciences [21]. The phenomenon is first observed around the critical point in phase transitions. In research of metamaterials, there exist two kinds of definition for “scaling behavior”, both described by the formula Eq. (1-1). The first kind concerns the truss



---

mechanics of cellular materials (by Gibson & Ashby [22]), where  $\rho$  is determined by the corresponding truss diameters, hence we can name it as “scaling by diameter”. The second kind is more often found in aerogels or fiber networks, where  $\rho$  is determined by the quantity of generating elements (particles or fibers), hence we can name it as “scaling by generating function”, in which case  $\alpha$  can easily surpass 3. In both cases,  $\alpha$  is a material- and density-invariant coefficient, which has been proven to be a useful parameter value for determining the structure-property relationships of a wide range of metamaterials.

There are two distinct species of cellular solids, one of which is named as “bending-dominated” structures, typified by foams, while the other is named as “stretching-dominated” structure, typified by triangulated lattice structures. Foams can be made by mixing metals, glasses, polymers or ceramics with a foaming agent. Conventionally, the structure of foams can be idealized as a cell whose shape is shown in Figure 1-10 (Left). This cell usually contains cell walls that surround a void space, which will show bending behavior when loaded with pressure. Lattice structures (Figure 1-10 Right), on the opposite, are designed to suppress bending, such that when loaded the cell walls would stretch rather than bend [23].

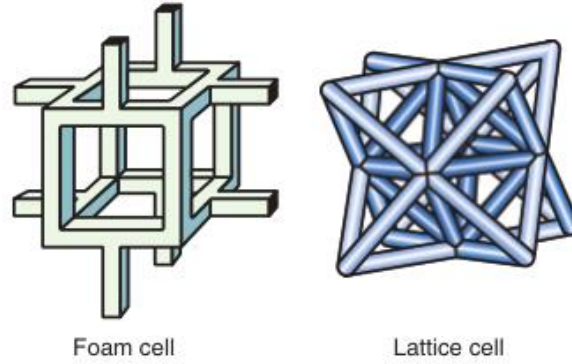


Figure 1-14. Left: an idealized cell in a low-density foam. Right: a fully triangulated lattice structure. (Reprinted from Ref. [22])

We now derive the scaling law for foam materials from the ideal model. First, we express the density of the structure as

$$\rho_r = C_1 \left( \frac{t}{L} \right)^2 \quad (1-2)$$

where  $\rho_r$  is the relative density of the foam compared to the solid,  $L$  is the length of the cell,  $t$  is the thickness, and  $C_1$  is a constant which can be approximately equal to 1. On the other hand, a compressive force  $F$  is remotely exerted on the cell edges, which would lead to a deflection  $\delta$  as

$$\delta \propto \frac{FL^3}{E_0 I} \quad (1-3)$$

where  $E_0$  is the intrinsic modulus of the foam material and  $I = t^4/12$  is the second moment of the cross section of the cell. The total compressive strain loaded on the cell is then  $\varepsilon = 2\delta/L$ . From eqs. (1-2) and (1-3) it derives the modulus  $E = \sigma/\varepsilon$  of the foam

$$E = C_2 \rho_r^2 E_0 \quad (\text{bending-dominated behavior}) \quad (1-4)$$

On the other hand, the fully triangulated structure shown in Fig. 1-10 right will only



---

---

stretch under elastic loadings. For example, on average only 1/3 of the cell edges carry tension when the triangulated structure is stretched regardless of the loading direction.

Therefore, the effective Young's modulus can be expressed as

$$\bar{E} = C_3 \rho_r E_0 \quad (\text{stretch-dominated behavior}) \quad (1-4)$$

with  $C_3 = 1/3$ . The modulus is linearly dependent on the relative density, which means that the structure is stiffer than a foam of the same density.

### 1.3 Ashby Charts

Material properties can be plotted in a Material Property Chart with log-log scale (sometimes referred to as Ashby Chart, after the material scientist MF Ashby), which is useful for material selections, and act as a guideline for a search of materials with properties as designed [24]. As an example, Figure 1-15 shows an Ashby Chart of Young's modulus plotted against density. The small bubbles show the range of the properties exhibited by a given material type (marked by small black labels). The larger colored envelopes enclose material families (marked by boldface labels) including metals, technical ceramics, composites, polymers, elastomers and foams.

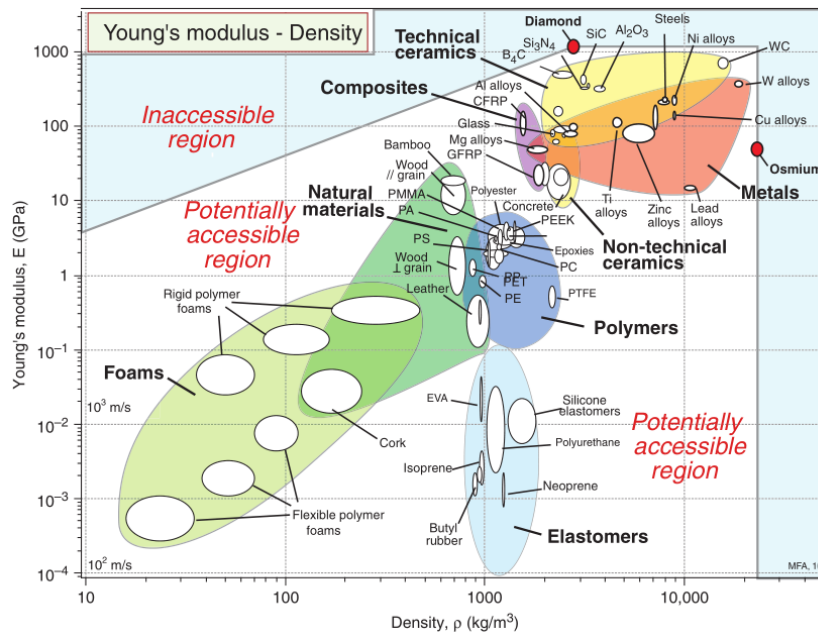


Figure 1-15. A typical Ashby Chart encapsulating all types of common materials for lookup of Young's modulus. (Reprinted from [21]).

Figure 1-16 shows an Ashby Chart of Young's modulus plotted against density for cellular structures [21]. The base material is aluminum 20% SiC(p), a type of industrial metallic foams, which is located at the upper right part within in the envelope of "Composite". The yellow marks show the calculated data for modeled Al-SiC(p) foams, and the red marks show the measured data for the real ones. Meanwhile, the green marks with red labels represent the lattice models, which lies at higher values of modulus for the same density. It is worth noting that, at a relative density  $\rho_r = 3.5\%$ , the modulus of the lattice can reach as high as 10 times over a foam of the same density. Other types of materials (over 3000 data points) including various kinds of ceramics, metals, composites, polymers and material foams are also plotted in Figure 1-16 [21]. The performance of lattice structures exceeds all of them.

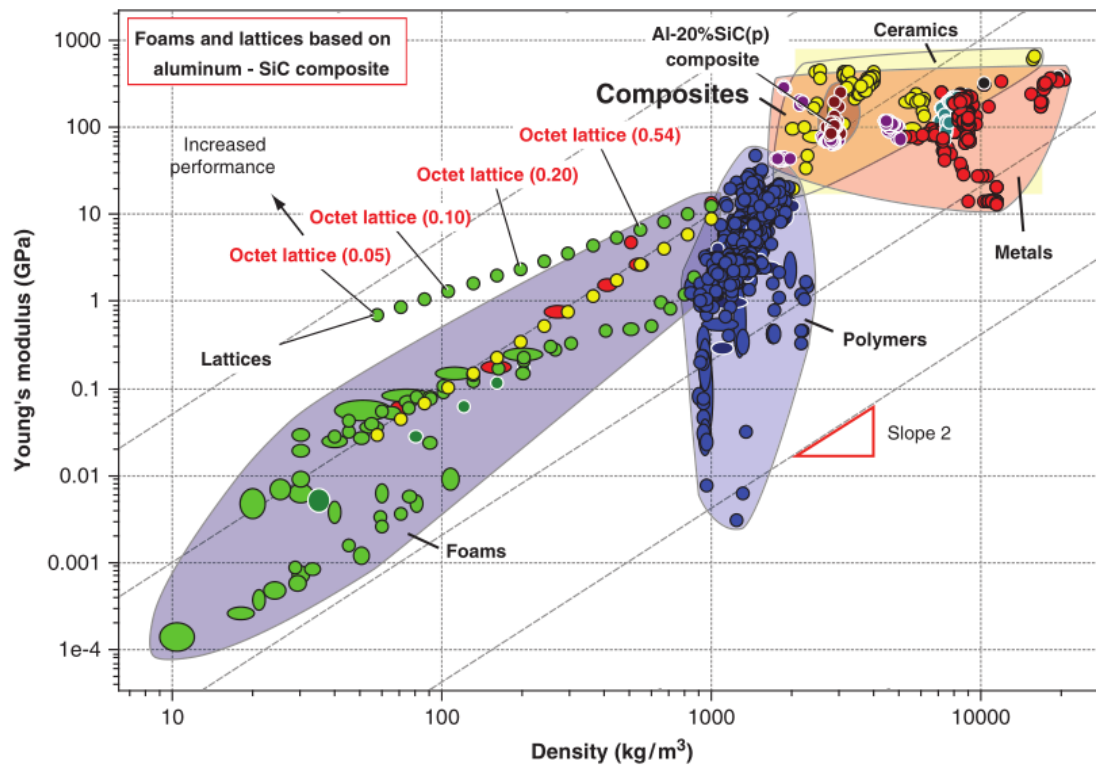


Figure 1-16. The moduli of Al – 20%SiC lattices compared with those of the other engineering materials. The values of lattices lie outside the envelope of existing materials of the chart. Numbers in brackets are relative densities. (Reprinted from [21]).

## 1.4 High-throughput Calculation

High-throughput calculation is a method to enable nowadays supercomputer power to automatically conduct heavy calculation tasks by programming [22]. For material calculations, typically, the programmed codes will contain the interfaces for input of material models, the part of paralleling and task submission to the supercomputer, the core part of doing physical analysis (by different numerical methods, such as finite element analysis, augmented plane wave methods, etc.), and finally the part of recording calculated results, etc.

In the field of material research, the most famous group is the one named “the



Materials Project”, the target of which is to enable researchers to easily lookup all the required material properties from a built-up database of material properties, and to conveniently data-mine scientific trends in materials properties. In the past two years, “the Materials Project” has successfully computed and documented the elastic and piezoelectric data of about a thousand of inorganic compounds, as shown in the figure below [23-25].

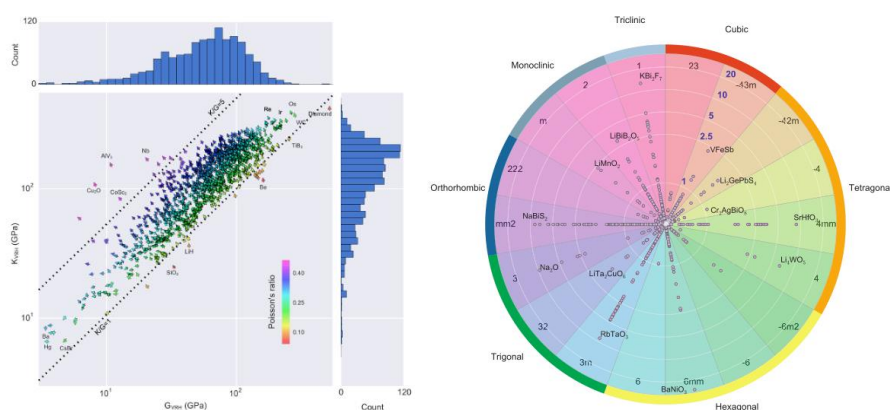


Figure 1-17. (Left) Distribution of calculated Poisson ratio, bulk modulus and shear modulus for 1181 metals, compounds and non-metals. (Right) Distribution of piezoelectric constants of 941 materials. (Reprinted from [23-25]).

Figure 1-17 (Left) shows a log-log plot of the bulk modulus versus the shear modulus for all 1181 materials. It shows that most materials lie in the region around 80 and 190 GPa for the shear and bulk moduli, respectively. In Figure 1-13 (right), piezoelectric properties of 941 materials were also calculated, where the maximum piezoelectric modulus  $\|e_{ij}\|_{\max}$  is plotted in a pie-chart. The high-throughput calculations have confirmed high piezoelectric constants for compounds such as  $\text{PbTiO}_3$ ,  $\text{BaNiO}_3$ ,  $\text{RbTaO}_3$  and  $\text{SrHfO}_3$ ; meanwhile, the study has also predicted a set of



---

---

new potent piezoelectric materials, including  $VFeSb$ ,  $Li_4WO_5$ ,  $LiMnO_2$ ,  $NaBiS_2$  and a few dozen others.

Since metamaterials (with repeating unit-cells) can be macroscopically viewed as some kind of homogenous materials, it follows natural that we can apply the same research methodology to metamaterials. However, the extra freedoms of choosing the internal structure of a metamaterial have made it difficult to arrive at a general understanding of the structure-property relations of metamaterials. New methods must be developed to categorize certain topological features to reduce the complexity of the problem. Some candidates can be symmetry properties and scaling behavior studied in the present work, which is a small step toward this goal.

## **1.5 Calculation Methods**

### **1.5.1 Finite Element Method**

Finite element method (FEM) is a numerical technique to divide up a complex geometry into amounts of small and simple elements that the physical fields inside the elements can be solved (often by solving PDEs) in parallel with consideration of coupling terms with each other [26-28]. The whole domain under FEM often consists of smaller and simpler subdomains (called finite elements) connected to each other in a finite number of points (called nodes). Basically, the FEM is conducted via the following steps: 1) the continuum is divided into a finite number of elements of



---

geometrically simple shape. 2) Find out a finite number of nodes that connect the elements. 3) Define the unknowns to be solved, e.g., the displacement  $\mathbf{u}(u, v, w)$  field, or the voltage field ( $V$ ) of the nodes. 4) Choose some polynomial interpolation functions describe the unknown field values at each point of the elements related to the corresponding field values at the nodes. 5) The forces (or other boundary loads) applied to the whole domain are replaced by an equivalent system of forces applied to the nodes. 6) PDE for all the elements or nodes is constructed as a large matrix form. 7) The PDE is solved using fast algorithms. 8) Other derivative field values are derived from the unknown field values. FEM has been proved to be an ideal tool for solving the problem of partial derivative equations.

## 1.5.2 COMSOL software package

This research employed COMSOL software package to compute all the elastic, dielectric, piezoelectric and optical properties of different designs of metamaterials. In this section the basic usage and operation of the relevant modules include the “Solid Mechanics”, “Electrostatics”, “Wave Optics” will be introduced.

### 1) Solid Mechanics and Electrostatics

**Material Assignments:** in this module, the elastic properties should be defined, for anisotropic materials, the total number of elastic tensor amounts to 36 parameters; for anisotropic piezoelectric materials, the whole tensor with 81 entries should be input as parameters.



---

**Boundary Conditions:** either displacement or loaded stress should be applied on the outer boundary of the simulation domain. When electrostatics is considered, proper electrical ground boundary should also be applied.

## 2) Wave Optics

**Material Assignments:** in this module, the only important material property is the dielectric constant (or relative permittivity)  $\epsilon$  of the simulated material. For example, usual dielectric substrate such as organic epoxy has a dielectric constant  $\epsilon = 2.5$  at Terahertz frequencies. Sometimes we should also assign frequent-dependent variables to this property when the dispersion effect is severe, such as permittivity of gold under optical frequencies.

**Boundary Conditions:** optical module involves, in the current work (both for terahertz and optical frequencies), the source of the light is selected to be plane wave, and the simulation domain should be larger than 3 times of the scatterer.

### 1.5.3 Software Framework

High-throughput calculation is a method to enable nowadays supercomputer power to automatically conduct heavy calculation tasks by programming. For material calculations, typically, the programmed codes will contain the interfaces for input of material models, the part of paralleling and task submission to the supercomputer, the core part of doing physical analysis (by different numerical methods, such as finite element analysis, augmented plane wave methods, etc.), and finally the part of



recording calculated results, etc.

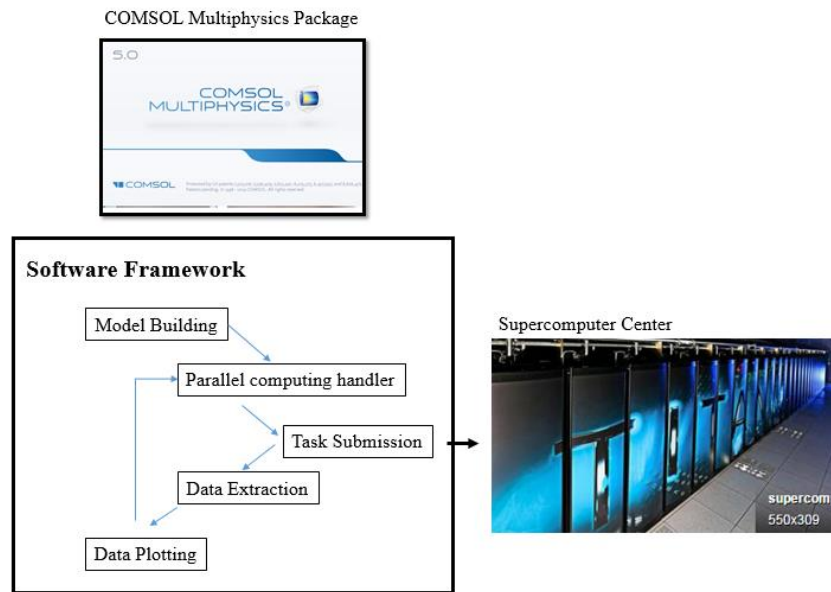


Figure 1-18. The software framework for high-throughput calculation in this work.

## 1.6 Scope of the present work

As discussed above, this study will help to promote a full understanding of the structure-property relation of metamaterials, and may lead to significant contributions to the development of the fields of aeronautics, transportation, and medication, etc. The research work conducted for this thesis focuses on the elastic and piezoelectric properties of various type of metamaterials, and also includes some new models of terahertz and optical metamaterials. This introducing chapter is followed by 6 other chapters:

Chapter 2 focuses on the symmetry properties of various as-designed metamaterial structures. Chapter 3 includes the study of the elastic properties of metamaterials, including the Young's modulus, shear modulus, and the Poisson's ratio, in which some



---

---

non-conventional properties such as structural cross-overs, which have not been reported in literature. Chapter 3 also includes the study of piezoelectric properties of metamaterials, including the dielectric constants, poling directions, piezoelectric constants, which found some laws to generate ultra-high piezoelectric properties. Chapter 4 introduces a metamaterial design on piezoelectric material, to tune their terahertz properties. Chapter 5 describes the different resonating mode for optical metamaterials. Conclusion and suggestion for future work are given in Chapter 6.

## 1.7 Statement of original contributions

For both elastic and piezoelectric materials, extensive computational efforts have been made by others via theoretical modelling and numerical analysis. Some typical work include 1) A. P. Robert *et al*'s numerical study of open- and closed-cell foams, and 2) Deshpande *et al*'s design and analysis of architected lattice materials, 3) MacKintosh *et al*'s modelling and analysis of fiber networks, 4) Venkatesh *et al*'s parametric study of piezoelectric foam materials, and 5) Sun *et al*'s work on 0-3 type magneto-electric composites. However, there still remains much room for improvements that my work can contribute importantly to a general theoretical understanding of metamaterials, especially for the establishment of the picture of structure-property relation.

To the best of my knowledge, the present work has made the following original contributions: 1) previous studies on lattice materials are constrained to truss-like



---

structures, while the current work has employed structures with curved geometries, which has brought in some new physics; 2) since the building block of metamaterials – the “meta-atoms” – acting like unit cells in crystals, symmetry issues has been considered; 3) there exists possibilities for scaling constant beyond the  $1 < \alpha < 2$  bounds, and the reason for this variation should be clarified; 4) the tool of Ashby Chart has been extended to piezoelectricity, and other functional properties. Generally speaking, scientifically, we need to construct a comprehensive picture depicting the structure-property relationship to get insights into the complexity of metamaterials; while technically, it is necessary to design new structures to fill out the holes of the “material property space”, and to enrich future material selections in the metamaterial range. Meanwhile, in light of the current 3D printing technologies – which have proved their potential in getting complex structures printed in hours – experimental verification of our numerical predictions would hopefully be easily accomplished in the near future.



---

---

# Chapter 2. Symmetry Properties of Micro-architected Metamaterials

## 2.1 Introduction

Crystals are categorized into 230 space groups according to their symmetry types, which are strongly associated with their physical properties [31]. For the reason symmetry is also an important consideration in the study of metamaterials. This Chapter presents an analysis of six types of models of metamaterials in terms of their geometric symmetries, corresponding deformation behavior and stress mechanisms, as well as the degrees of symmetry of their elastic properties.

## 2.2 Deformation and Stress – Modelling and Analysis

We consider 6 types of micro-architectures of metamaterials, with three of them being conventional models in the research field of cellular metals, namely the cubic truss (CT), the octet truss (OT), and the ideal open-cell foam (IF) model, where a detailed comparison between them cannot be found in the literature. The other three models, namely the gyroid (GR), the wave-network (WN) and the helix-network (HN) models, are self-designed models with some additional degrees of freedom of bending and waviness and they are not necessarily cubic symmetric (Figure 3-1). Each modelling process typically involves a designing of the model's geometry (i.e. for our

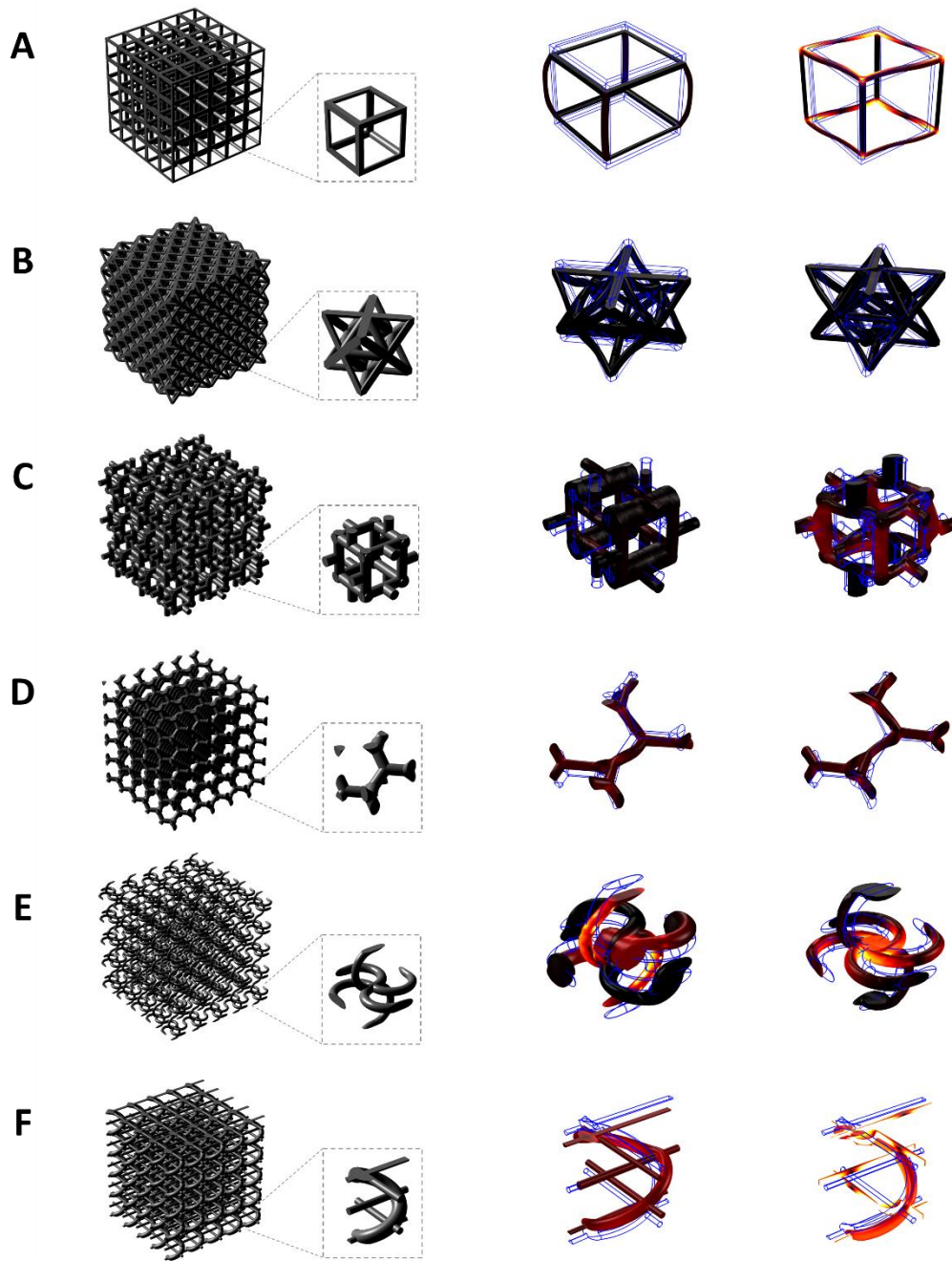


Figure 2-1. Schematic diagrams of 6 models of micro-architected metamaterials, namely (a) the cubic truss, (b) the octet truss, (c) the ideal open-cell foam, (d) the gyroid, (e) the wave network, and (f) the helix network. For each of these models, the 1st, 2nd, 3rd and 4th column from the left show, respectively, the design of the model's geometry, the corresponding unit cell, the deformation behavior under uniaxial compression along the z direction, as well as that under shear stress along the x-y plane.



self-designed models) as well as a selection of the system size and of the stress applied to each surface, and each simulation is chosen to be conducted on a sufficiently large simulation domain (also referred to as the “representative volume element”) of  $5 \times 5 \times 5$  cubic unit cells so as to minimize any finite-size effect on the system’s mechanical properties [41].

Geometric details of the six models are shown in Figure 2-1, with matrix and unit-cell representations, as well as their deformation patterns under normal and shear stresses. The surface color represents the internal von Mises stress distribution, with the brighter regions bearing more stresses and thereby more prone to yield. A detailed comparisons of the symmetry properties of these different models is presented in Table 2-1.

Table 2-1. Summary of symmetry properties.

| Model Type                      | Point Group Symmetry<br>(Geometric) | Point Group Symmetry<br>(Elastic) | Particulars                |
|---------------------------------|-------------------------------------|-----------------------------------|----------------------------|
| CT<br>(Cubic Truss)             | $O_h$                               | $O_h$                             | Unstable Shear<br>Response |
| OT<br>(Octet Truss)             | $O_h$                               | $O_h$                             | Most Tough                 |
| IF<br>(Ideal open-cell<br>foam) | $D_2$                               | $O_h$                             | -                          |
| GR<br>(Gyroid)                  | $C_2$                               | $O_h$                             | -                          |
| WN<br>(Wave-network)            | $C_i$                               | $C_{2h}$                          | Auxetic                    |
| HN<br>(Helix-network)           | $C_1$                               | $D_{4h}$                          | Most Brittle               |



## 2.3 Spherical Representation and Reduced Variables

According to the reference 43, elastic properties  $F$  along any directions can be described as functions of the Euler angles  $F = F(\varphi, \theta, \psi)$ , which are  $E$  (Young's modulus),  $G$  (shear modulus), or  $\nu$  (Poisson's ratio), and  $(\varphi, \theta, \psi)$  are the rotation angles of a new coordinate frame  $(x', y', z')$  relative to an original frame  $(x, y, z)$ .

We begin with a consideration of Hooke's law. First, the components of the elastic strain tensor  $\varepsilon_{ij}$  are related to the stress components  $\sigma_{km}$  by

$$\varepsilon_{ij} = S_{ijkl} \sigma_{km} \quad (2-1)$$

where  $S_{ijkl}$  is referred to as the compliance tensor. The primed compliance tensor in the new coordinate frame can be expressed by a transformation equation

$$S'_{ijkl} = A_{im} A_{jn} A_{kp} A_{lq} S_{mnpq} \quad (2-2)$$

where the indices  $(i, j, k, l, m, n, p, q)$  of the direction cosines  $A$  can be 1, 2, and 3 (following the summation convention). For the case of cubic symmetry, Thomas *et al.* showed that the transformation takes the form [31]

$$S'_{ijkl} = S_{1122} \delta_{ij} \delta_{kl} + S_{1212} (\delta_{ik} \delta_{jl} + \delta_{il} \delta_{jk}) + (S_{1111} - S_{1122} - 2S_{1212}) A_{iu} A_{ju} A_{ku} A_{lu} \quad (2-3)$$

where  $\delta_{ij}$  is the Kronecker delta, the indice  $u$  runs over 1, 2, and 3. The angular dependence is also considered within a set of only three compliances coefficients instead of the 81 compliance coefficients of equation (2-2). The three most used elastic



coefficients can be derived from the compliance tensor as:

$$\text{Young's modulus: } E'_i = 1 / S'_{iii} \quad (2-4)$$

$$\text{Shear modulus: } G'_{ij} = 1 / 4S'_{ijj} \quad (i \neq j) \quad (2-5)$$

$$\text{Poisson's ratio: } \nu'_{ij} = -S'_{ijj} / S'_{iii} \quad (i \neq j) \quad (2-6)$$

The position coordinate  $x'$  in the new coordinate frame is related to that in the original frame by

$$x'_i = A_{iu} x_u = (W_\theta V_\beta U_\alpha)_{iu} x_u \quad (2-7)$$

Direction cosines  $A_{st}$  can be written in terms of Eulerian angles  $\theta$ ,  $\varphi$  and  $\psi$ , which are defined in Figure 2-2.

$$[A_{st}] = \begin{bmatrix} A & B & C \\ (D \sin \psi + E \cos \psi) & (F \sin \psi + G \cos \psi) & H \sin \psi \\ (D \sin \psi - E \cos \psi) & (F \sin \psi - G \cos \psi) & H \cos \psi \end{bmatrix} \quad (2-8)$$

where

$$\begin{aligned} A &= \cos \varphi \cos \theta & E &= -\sin \varphi \\ B &= \sin \varphi \cos \theta & F &= -\sin \varphi \sin \theta \\ C &= \sin \theta & G &= \cos \varphi \\ D &= -\cos \varphi \sin \theta & H &= \cos \theta \end{aligned} \quad (2-9)$$

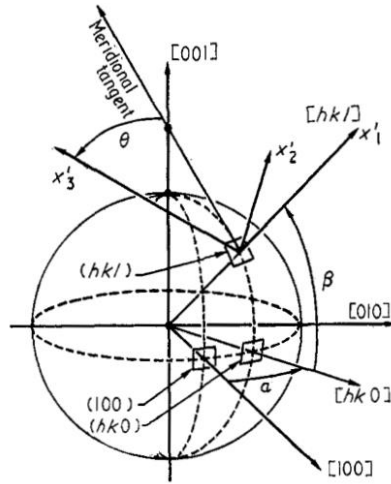


Figure 2-2. Transformation of coordinate frame and the related Eulerian angles. (Reprinted from [30])

In general, for anisotropic materials,  $E$ ,  $G$ , and  $\nu$  are all tensor parameters which cannot be directly visualized, hence for convenience, we have adopted three reduced variables  $\|E\|$ ,  $\|G\|$  and  $\|\nu\|$  (as shown by different columns in Fig. 2-1), which are all scalar parameters defined as follows:

- 1) For each new coordinate frame  $(x', y', z')$  resulting from a rotation by  $(\varphi, \theta, \psi)$ ,  $\|E\|$  is simply the longitudinal Young's modulus  $E_{z'}$ ;
- 2)  $\|G\| = (G_{z'x'} + G_{z'y'})/2$  is a measure of the resistance against any shear stress applied onto the  $z'$ - surface;

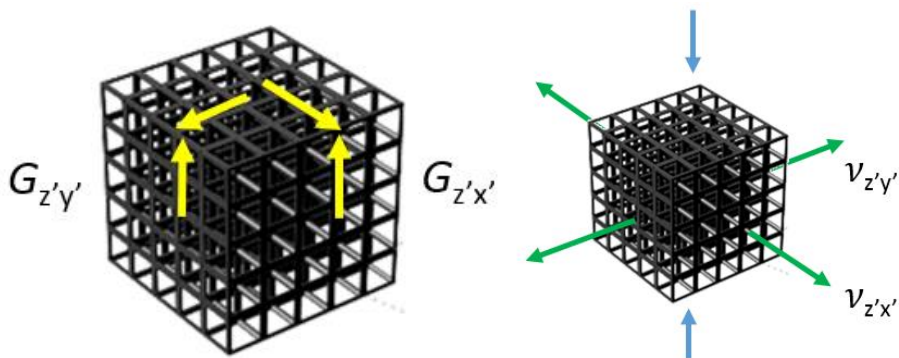


Figure 2-3. Schematics for  $\|G\|$  and  $\|\nu\|$ .



---

3)  $\|v\| = (v_{z'x'} + v_{z'y'})/2$  is a measure of the lateral contraction or extension when a  $z'$ -directional tension or pressure is applied.

Practically,  $\|E\|$  and  $\|v\|$  are invariant about the “roll angle”  $\psi$  so we can just plot the bivariate function  $F(\varphi, \theta)$  in spherical coordinates. In contrast,  $\|G\|$  cannot be fully represented on a spherical surface, so we choose to plot out its extrema,  $\|G\|_{\max} = \max(\|G(\theta, \varphi)\|, \psi)$  and  $\|G\|_{\min} = \min(\|G(\theta, \varphi)\|, \psi)$ , where the difference between will also be plotted.

## 2.4 Results and Discussion

Each row in Figures 2-4 and 2-5 show the  $F$ -plots of the different models (from CT to HN), in which all the three plots of  $\|E\|$ ,  $\|G\|$ , and  $\|v\|$  exhibit the same type of point symmetry as indicated by the contour shapes. We refer to this symmetry as “elastic symmetry”, to be distinguished from the “geometric symmetry” observed in Figure 2-1. For some perfect cubic models such as CT and OT, the elastic symmetry remained the same as the geometric symmetry (from  $O_h$  to  $O_h$ , or written as CT:  $O_h \rightarrow O_h$  and OT:  $O_h \rightarrow O_h$ ); while for other models, the higher degree of symmetry for their elastic properties compared with their geometric counterparts are obviously observed, namely, IF:  $D_2 \rightarrow O_h$ , GR:  $C_2 \rightarrow O_h$ , WN:  $C_1 \rightarrow C_{2h}$ , and HN:  $C_1 \rightarrow D_{4h}$ . The left-most column lists the forms of stiffness tensors for each model, which are exactly the matrix representations for corresponding point symmetry groups. As a special case, the  $F$ -plots of WN is seen to be tilted from the orthogonal lattice vectors by an angle  $\theta$ . This effect is originated from the topological property of wave shapes, and can also be described



by an additional term of  $C_{16}$  in the corresponding matrix.

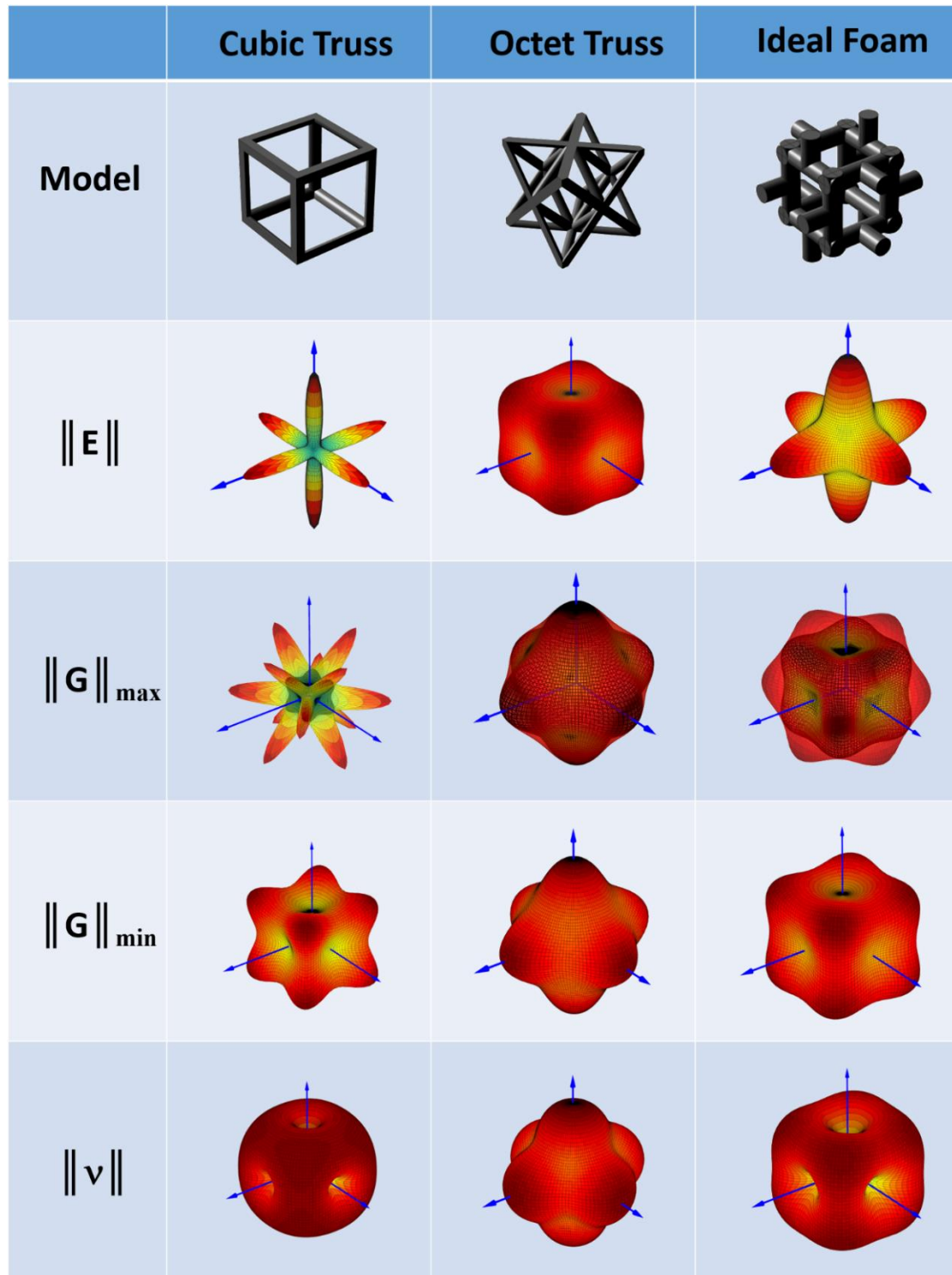


Figure 2-4. Symmetry of Micro-architected Metamaterials. The 1<sup>st</sup>, 2<sup>nd</sup>, 3<sup>rd</sup>, 4<sup>th</sup> and 5<sup>th</sup> rows show the elastic tensor matrix, the F-plots of  $\|E\|$ ,  $\|G\|_{\max}$ ,  $\|G\|_{\min}$  and  $\|v\|$ , respectively, for geometry type of the cubic truss, the octet truss, the ideal open-celled foam, respectively. Relative density are set to be 0.2.

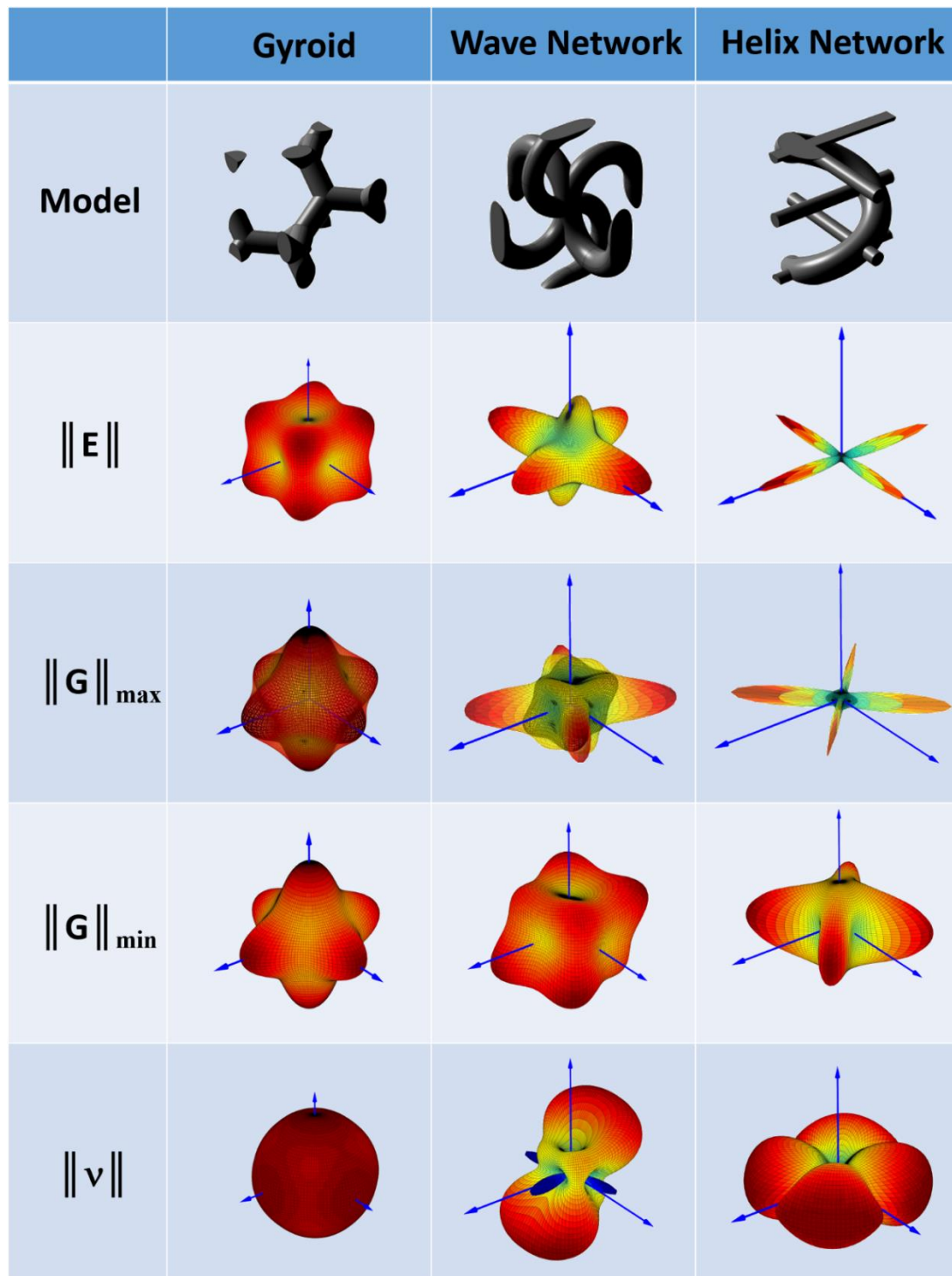


Figure 2-5. Symmetry of Micro-architected Metamaterials. The 1<sup>st</sup>, 2<sup>nd</sup>, 3<sup>rd</sup>, 4<sup>th</sup> and 5<sup>th</sup> rows show the elastic tensor matrix, the F-plots of  $\|E\|$ ,  $\|G\|_{\max}$ ,  $\|G\|_{\min}$  and  $\|\nu\|$ , respectively, for geometry type of the gyroid, the wave network, the helix network, respectively. Relative density are set to be 0.2.



The anisotropy of all models, as reflected by their  $F$ -plots of  $\|E\|$  and  $\|G\|$ , is also strongly dependent on the difference  $\Delta G = \|G\|_{\max} - \|G\|_{\min}$ . For those 4 models with  $O_h$  – symmetry we can rank their anisotropy via their anisotropy factor  $A^U$  in increasing order as  $OT < GR < IF < CT$ . The relatively weak anisotropy of OT has constituted part of the reason for its popularity in engineering [45]. Moreover, all the 6  $F$ -plots exhibit different characteristics of convexity or concavity along different directions, and the convexity or concavity of the  $\|G\|$ - and  $\|v\|$ - plots is often opposite to that of the  $\|E\|$ - plots. For example, OT exhibits concave  $\langle 100 \rangle$  and convex  $\langle 111 \rangle$  shapes for its  $\|E\|$ - plot, but convex  $\langle 111 \rangle$  and concave  $\langle 100 \rangle$  shapes for its  $\|G\|$ - and  $\|v\|$ - plot. An extreme condition occurs for WN when its  $\|v\|$  value get too concave such that it becomes negative (or auxetic) for the  $[100]$  and  $[010]$  directions. This auxeticity is caused by the rotation coupling of x- and y- arms, which is analogous to that in the missing-rib model [47].

For the various  $O_h$  – symmetric models CT, OT, IF and GR, the stiffness matrix was accidentally found to be of the following form

$$\begin{bmatrix} C_{33} & C_{12} & C_{12} & 0 & 0 & 0 \\ C_{12} & C_{33} & C_{12} & 0 & 0 & 0 \\ C_{12} & C_{12} & C_{33} & 0 & 0 & 0 \\ 0 & 0 & 0 & C_{44} & 0 & 0 \\ 0 & 0 & 0 & 0 & C_{55} & 0 \\ 0 & 0 & 0 & 0 & 0 & C_{66} \end{bmatrix} \quad (2-10)$$

For the WN model, the stiffness matrix is given by



---

---

$$\begin{bmatrix} C_{11} & C_{12} & 0 & 0 & 0 & C_{16} \\ C_{12} & C_{11} & 0 & 0 & 0 & -C_{16} \\ 0 & 0 & C_{33} & 0 & C_{35} & 0 \\ 0 & 0 & 0 & C_{44} & 0 & 0 \\ 0 & 0 & C_{35} & 0 & C_{44} & 0 \\ C_{16} & -C_{16} & 0 & 0 & 0 & C_{66} \end{bmatrix} \quad (2-11)$$

And for HN model, the stiffness matrix is given by

$$\begin{bmatrix} C_{11} & C_{12} & 0 & 0 & 0 & 0 \\ C_{12} & C_{11} & 0 & 0 & 0 & 0 \\ 0 & 0 & C_{33} & 0 & 0 & 0 \\ 0 & 0 & 0 & C_{44} & 0 & 0 \\ 0 & 0 & 0 & 0 & C_{44} & 0 \\ 0 & 0 & 0 & 0 & 0 & C_{66} \end{bmatrix} \quad (2-12)$$

## 2.5 Summary

The following conclusions can be drawn from a study of the elastic responses and symmetry of various metamaterial models, there are several points that can be concluded: 1) the elastic tensors are found to be more symmetric than their geometric counterparts – the elastic properties can exhibit cubic symmetry even though the original geometry is not cubic; 2) the different elastic tensors of any models share the same type of elastic symmetry; 3) for the WN model, auxeticity occurs only along specific directions.



---

---

# Chapter 3. Scaling Behavior in Micro-architected Metamaterials

## 3.1 Introduction

One approach to get physical insights into the structural variations of metamaterials is to study their scaling behavior, i.e., the phenomena that their mechanical properties generally obeys the law  $F \propto A\rho^\alpha$ , where  $\alpha$  is the scaling constant,  $\rho$  is the relative density, and  $F$  can be the indicator of stiffness, or strength, etc. It is evident that the exponent  $\alpha$  is only related to the geometry, but not constituent materials. This property has made  $\alpha$  a useful tool for structural characterization of metamaterials. A conventional dichotomy is to classify the geometry into being bending-dominated or stretch-dominated, with  $\alpha = 1$  or  $2$ , respectively. Practically, an intermediate value of  $\alpha$  between 1 and 2 is often the case, sometimes interpreted as a combined effect of stretching and bending. This theory has been extensively verified from different types of material structures, including open- and closed- cell foams, fiber networks, and also architected lattice materials. Current research on mechanical metamaterials focuses on a pursuit of metamaterials in the high modulus limit of  $\alpha = 1$ , to attain stiffer and stronger metamaterials at lower densities, among which the structure of “octet-truss” lattice built with hollow nanotubes is a good candidate. However, for research on “low-modulus-limit” and “non-truss-like” structures, few work have been done.

Different from purely elastic materials which are only concerned for their stiffness or strength, piezoelectric materials are also expected to exhibit excellent performance



---

---

on electro-mechanical energy conversions. To acquire piezoelectric properties exceeding monolithic ones, various approaches like constructing layered, porous, or particulate piezoelectric composites have been applied. However, in most samples, pores or particulates are randomly distributed while the distribution patterns are not under control (only limited to a few pore shapes and porosity), which has hindered further understanding about the structure-property relationship in piezoelectric foams. In this field, the only work of numerical modelling is Venkatesh *et al*'s studies on pore shape effects. Although the work is constrained to regular type pores, it has paved the basis for further study of other complex geometries.

Here in the following sections, we attempt to make a thorough analysis on the scaling behavior of meta-atoms defined in Chapter 2, for building a comprehensive understanding of the elastic, dielectric as well as piezoelectric properties for the overall metamaterials with random shape designs. The new findings in these studies include a classification method for property types, and a new high piezoelectric constant discovered in helix meta-atom design.

## **3.2 Theory and Method for Obtaining Effective Property**

### **3.2.1 Strain and Stress Tensors**

Generally, the displacement as well as the deformation of an infinitesimal material element can be described using the displacement (vector)  $\mathbf{u} = (u_x, u_y, u_z)$  and the



displacement gradient (2nd order tensor)

$$\Delta \mathbf{u} = \begin{pmatrix} \frac{\partial u_x}{\partial x} & \frac{\partial u_x}{\partial y} & \frac{\partial u_x}{\partial z} \\ \frac{\partial u_y}{\partial x} & \frac{\partial u_y}{\partial y} & \frac{\partial u_y}{\partial z} \\ \frac{\partial u_z}{\partial x} & \frac{\partial u_z}{\partial y} & \frac{\partial u_z}{\partial z} \end{pmatrix}. \quad (3-1)$$

Figure 3-1 shows the illustration of the deformation pattern of a 2-dimensional material element. From the figure we can find the deformation along different directions are

$\frac{\partial u_x}{\partial x} dx$ ,  $\frac{\partial u_y}{\partial x} dx$ ,  $\frac{\partial u_x}{\partial y} dy$ ,  $\frac{\partial u_y}{\partial y} dy$ , respectively. The pattern is the same for 3-

dimensional cases.

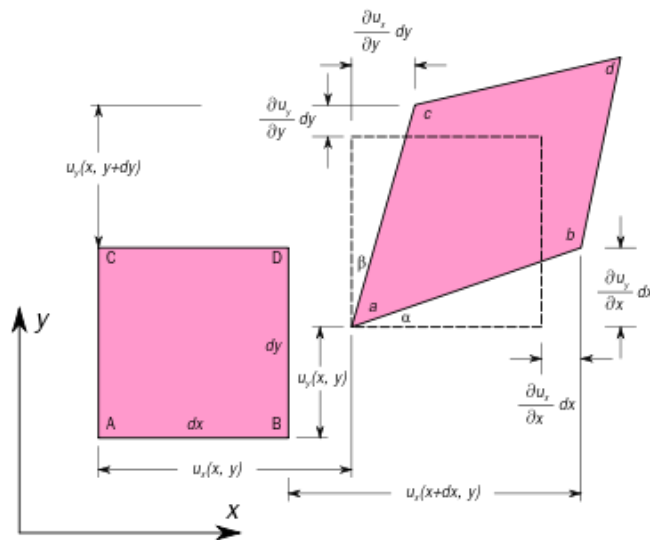


Figure 3-1. 2D deformation of an infinitesimal material element. (Reprinted from [40]).

When the displacement gradient is small compared to unity, it is convenient to define an infinitesimal strain tensor  $\epsilon$ , or Cauchy's strain tensor, with its 9 components

$\epsilon_{ij}$  as



$$\begin{aligned} \varepsilon_{ij} &= \frac{1}{2}(u_{i,j} + u_{j,i}) = \begin{bmatrix} \varepsilon_{11} & \varepsilon_{12} & \varepsilon_{13} \\ \varepsilon_{21} & \varepsilon_{22} & \varepsilon_{23} \\ \varepsilon_{31} & \varepsilon_{32} & \varepsilon_{33} \end{bmatrix} \\ &= \begin{bmatrix} \frac{\partial u_1}{\partial x_1} & \frac{1}{2}\left(\frac{\partial u_1}{\partial x_2} + \frac{\partial u_2}{\partial x_1}\right) & \frac{1}{2}\left(\frac{\partial u_1}{\partial x_3} + \frac{\partial u_3}{\partial x_1}\right) \\ \frac{1}{2}\left(\frac{\partial u_1}{\partial x_2} + \frac{\partial u_2}{\partial x_1}\right) & \frac{\partial u_2}{\partial x_2} & \frac{1}{2}\left(\frac{\partial u_2}{\partial x_3} + \frac{\partial u_3}{\partial x_2}\right) \\ \frac{1}{2}\left(\frac{\partial u_1}{\partial x_3} + \frac{\partial u_3}{\partial x_1}\right) & \frac{1}{2}\left(\frac{\partial u_2}{\partial x_3} + \frac{\partial u_3}{\partial x_2}\right) & \frac{\partial u_3}{\partial x_3} \end{bmatrix} \end{aligned} \quad (3-2)$$

or using different notation:

$$\begin{bmatrix} \varepsilon_{xx} & \varepsilon_{xy} & \varepsilon_{xz} \\ \varepsilon_{yx} & \varepsilon_{yy} & \varepsilon_{yz} \\ \varepsilon_{zx} & \varepsilon_{zy} & \varepsilon_{zz} \end{bmatrix} = \begin{bmatrix} \frac{\partial u_x}{\partial x} & \frac{1}{2}\left(\frac{\partial u_x}{\partial y} + \frac{\partial u_y}{\partial x}\right) & \frac{1}{2}\left(\frac{\partial u_x}{\partial z} + \frac{\partial u_z}{\partial x}\right) \\ \frac{1}{2}\left(\frac{\partial u_x}{\partial y} + \frac{\partial u_y}{\partial x}\right) & \frac{\partial u_y}{\partial y} & \frac{1}{2}\left(\frac{\partial u_y}{\partial z} + \frac{\partial u_z}{\partial y}\right) \\ \frac{1}{2}\left(\frac{\partial u_x}{\partial z} + \frac{\partial u_z}{\partial x}\right) & \frac{1}{2}\left(\frac{\partial u_y}{\partial z} + \frac{\partial u_z}{\partial y}\right) & \frac{\partial u_z}{\partial z} \end{bmatrix} \quad (3-3)$$

The overall stress at a point inside a body can be evaluated by considering all the stress vectors  $\mathbf{T}^{(n)}$  associated with all planes (with normal vector  $\mathbf{n}$ ) that pass through that point. Following Cauchy's stress theorem,  $\mathbf{T}$  can be expressed as a linear function of  $\mathbf{n}$ , as

$$\mathbf{T}^{(n)} = \mathbf{n} \cdot \boldsymbol{\sigma} \quad \text{or} \quad T_j^{(n)} = \sigma_{ij} n_i. \quad (3-4)$$

where  $\boldsymbol{\sigma} = \boldsymbol{\sigma}(\mathbf{x})$  is a second-order tensor field independent of  $\mathbf{n}$ , called the Cauchy's stress tensor, which completely defines the state of stress at a point;  $n_i$  ( $i = 1, 2, 3$ ) indicates the component of  $\mathbf{n}$  along the three basis vectors  $\mathbf{e}_1$ ,  $\mathbf{e}_2$ , and  $\mathbf{e}_3$ . This second-order tensor (which includes 9 components) takes the following form



$$\sigma = \sigma_{ij} = \begin{pmatrix} \sigma_{11} & \sigma_{12} & \sigma_{13} \\ \sigma_{21} & \sigma_{22} & \sigma_{23} \\ \sigma_{31} & \sigma_{32} & \sigma_{33} \end{pmatrix} \equiv \begin{pmatrix} \sigma_{xx} & \sigma_{xy} & \sigma_{xz} \\ \sigma_{yx} & \sigma_{yy} & \sigma_{yz} \\ \sigma_{zx} & \sigma_{zy} & \sigma_{zz} \end{pmatrix} \quad (3-5)$$

where  $\sigma_{11}$ ,  $\sigma_{22}$ , and  $\sigma_{33}$  are normal stresses, and  $\sigma_{12}$ ,  $\sigma_{13}$ ,  $\sigma_{21}$ ,  $\sigma_{23}$ ,  $\sigma_{31}$ , and  $\sigma_{32}$  are shear stresses. The index  $i$  and  $j$  indicate the normal direction of the plane in which the stress acts on, and the direction in which the stress acts along, respectively. Also, the stress tensor  $\mathbf{T}^{(n)}$  can be decomposed into 3 components  $\mathbf{T}^{(e1)}$ ,  $\mathbf{T}^{(e2)}$ , and  $\mathbf{T}^{(e3)}$  as:

$$\mathbf{T}^{(n)} = \mathbf{T}^{(e_1)}n_1 + \mathbf{T}^{(e_2)}n_2 + \mathbf{T}^{(e_3)}n_3 = \sigma_{ij}n_i\mathbf{e}_j. \quad (3-6)$$

Alternatively, in matrix form we have

$$\begin{pmatrix} T_1^{(n)} & T_2^{(n)} & T_3^{(n)} \end{pmatrix} = \begin{pmatrix} n_1 & n_2 & n_3 \end{pmatrix} \begin{pmatrix} \sigma_{11} & \sigma_{12} & \sigma_{13} \\ \sigma_{21} & \sigma_{22} & \sigma_{23} \\ \sigma_{31} & \sigma_{32} & \sigma_{33} \end{pmatrix} \quad (3-7)$$

An illustration of these tensors acting on a material element is shown in Figure 3-2.

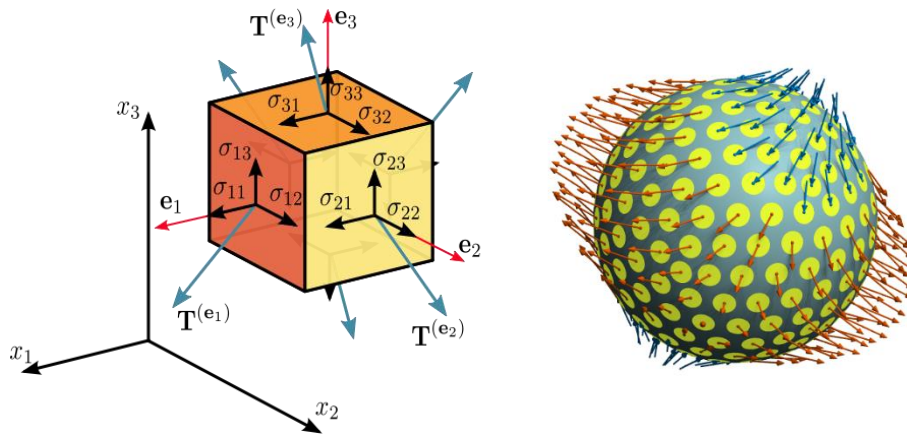


Figure 3-2. (Left) component of stress in three dimension. (Right) illustration of typical stress distribution across surface elements on the boundary of a sphere in a homogeneous material under uniform tri-axial stress. The normal stresses on the principal axes are +5, +2, and -3 units. (Reprinted from [40])



### 3.2.2 Elastic theory for continuous anisotropic media

The symmetry of the Cauchy stress tensor ( $\sigma_{ij} = \sigma_{ji}$ ) and the generalized Hooke's laws ( $\sigma_{ij} = c_{ijkl}\varepsilon_{kl}$ ) implies that  $c_{ijkl} = c_{jikl}$ . Meanwhile, the symmetry of the Cauchy strain tensor ( $\varepsilon_{ij} = \varepsilon_{ji}$ ) implies that  $c_{ijkl} = c_{ijlk}$ . Therefore, it is a convention to take Voigt notation to reduce the number of indices from 9 to 6 (and also for elastic constants it's from 81 to 36), and to write them as vectors with 6 components in an orthonormal coordinate system ( $\mathbf{e}_1, \mathbf{e}_2, \mathbf{e}_3$ ) as

$$[\boldsymbol{\sigma}] = \begin{bmatrix} \sigma_{11} \\ \sigma_{22} \\ \sigma_{33} \\ \sigma_{23} \\ \sigma_{13} \\ \sigma_{12} \end{bmatrix} \equiv \begin{bmatrix} \sigma_1 \\ \sigma_2 \\ \sigma_3 \\ \sigma_4 \\ \sigma_5 \\ \sigma_6 \end{bmatrix}; \quad [\boldsymbol{\varepsilon}] = \begin{bmatrix} \varepsilon_{11} \\ \varepsilon_{22} \\ \varepsilon_{33} \\ 2\varepsilon_{23} \\ 2\varepsilon_{13} \\ 2\varepsilon_{12} \end{bmatrix} \equiv \begin{bmatrix} \varepsilon_1 \\ \varepsilon_2 \\ \varepsilon_3 \\ \varepsilon_4 \\ \varepsilon_5 \\ \varepsilon_6 \end{bmatrix} \quad (3-8)$$

In addition, since the displacement gradient and the Cauchy stress are work conjugate, the stress–strain relation can be derived from a strain energy density functional ( $U$ ), then

$$\sigma_{ij} = \frac{\partial U}{\partial \varepsilon_{ij}} \Rightarrow c_{ijkl} = \frac{\partial^2 U}{\partial \varepsilon_{ij} \partial \varepsilon_{kl}} \quad (3-9)$$

In Eq. (3-9) the order of differentiation can be freely changed, which implies that  $c_{ijkl} = c_{klij}$ . All the three kinds of symmetry of the stiffness tensor reduce the number of elastic constants from 36 to 21. Then the stiffness tensor ( $\mathbf{C}$ ) can be expressed as



$$[\mathbf{C}] = \begin{bmatrix} c_{1111} & c_{1122} & c_{1133} & c_{1123} & c_{1131} & c_{1112} \\ c_{2211} & c_{2222} & c_{2233} & c_{2223} & c_{2231} & c_{2212} \\ c_{3311} & c_{3322} & c_{3333} & c_{3323} & c_{3331} & c_{3312} \\ c_{2311} & c_{2322} & c_{2333} & c_{2323} & c_{2331} & c_{2312} \\ c_{3111} & c_{3122} & c_{3133} & c_{3123} & c_{3131} & c_{3112} \\ c_{1211} & c_{1222} & c_{1233} & c_{1223} & c_{1231} & c_{1212} \end{bmatrix} \equiv \begin{bmatrix} C_{11} & C_{12} & C_{13} & C_{14} & C_{15} & C_{16} \\ C_{12} & C_{22} & C_{23} & C_{24} & C_{25} & C_{26} \\ C_{13} & C_{23} & C_{33} & C_{34} & C_{35} & C_{36} \\ C_{14} & C_{24} & C_{34} & C_{44} & C_{45} & C_{46} \\ C_{15} & C_{25} & C_{35} & C_{45} & C_{55} & C_{56} \\ C_{16} & C_{26} & C_{36} & C_{46} & C_{56} & C_{66} \end{bmatrix} \quad (3-10)$$

and the Hooke's law is

$$[\boldsymbol{\sigma}] = [\mathbf{C}][\boldsymbol{\varepsilon}] \quad \text{or} \quad \sigma_i = C_{ij}\varepsilon_j. \quad (3-11)$$

The compliance tensor ( $\mathbf{S}$ ) is

$$[\mathbf{S}] = \begin{bmatrix} s_{1111} & s_{1122} & c_{1133} & 2s_{1123} & 2s_{1131} & 2s_{1112} \\ s_{2211} & s_{2222} & c_{2233} & 2s_{2223} & 2s_{2231} & 2s_{2212} \\ s_{3311} & s_{3322} & c_{3333} & 2s_{3323} & 2s_{3331} & 2s_{3312} \\ 2s_{2311} & 2s_{2322} & 2s_{2333} & 4s_{2323} & 4s_{2331} & 4s_{2312} \\ 2s_{3111} & 2s_{3122} & 2s_{3133} & 4s_{3123} & 4s_{3131} & 4s_{3112} \\ 2s_{1211} & 2s_{1222} & 2s_{1233} & 4s_{1223} & 4s_{1231} & 4s_{1212} \end{bmatrix} \equiv \begin{bmatrix} S_{11} & S_{12} & S_{13} & S_{14} & S_{15} & S_{16} \\ S_{12} & S_{22} & S_{23} & S_{24} & S_{25} & S_{26} \\ S_{13} & S_{23} & S_{33} & S_{34} & S_{35} & S_{36} \\ S_{14} & S_{24} & S_{34} & S_{44} & S_{45} & S_{46} \\ S_{15} & S_{25} & S_{35} & S_{45} & S_{55} & S_{56} \\ S_{16} & S_{26} & S_{36} & S_{46} & S_{56} & S_{66} \end{bmatrix}, \quad (3-12)$$

another form of Hooke's law can be written as

$$[\boldsymbol{\varepsilon}] = [\mathbf{C}][\boldsymbol{\sigma}] \quad \text{or} \quad \varepsilon_i = C_{ij}\sigma_j. \quad (3-13)$$

In materials with special symmetry, the transformation relation can be simplified.

For example, in orthotropic materials, the basis vectors ( $\mathbf{e}_1, \mathbf{e}_2, \mathbf{e}_3$ ) are normal to the planes of symmetry. Therefore, the number of elastic constant is further reduced from 21 to 9, which implies a new transformation relation



$$\begin{bmatrix} \sigma_1 \\ \sigma_2 \\ \sigma_3 \\ \sigma_4 \\ \sigma_5 \\ \sigma_6 \end{bmatrix} = \begin{bmatrix} C_{11} & C_{12} & C_{13} & 0 & 0 & 0 \\ C_{12} & C_{22} & C_{23} & 0 & 0 & 0 \\ C_{13} & C_{23} & C_{33} & 0 & 0 & 0 \\ 0 & 0 & 0 & C_{44} & 0 & 0 \\ 0 & 0 & 0 & 0 & C_{55} & 0 \\ 0 & 0 & 0 & 0 & 0 & C_{66} \end{bmatrix} \begin{bmatrix} \varepsilon_1 \\ \varepsilon_2 \\ \varepsilon_3 \\ \varepsilon_4 \\ \varepsilon_5 \\ \varepsilon_6 \end{bmatrix} \quad (3-14)$$

The inverse of this relation is (written in coordinate frame  $x, y$  and  $z$ )

$$\begin{bmatrix} \varepsilon_{xx} \\ \varepsilon_{yy} \\ \varepsilon_{zz} \\ 2\varepsilon_{yz} \\ 2\varepsilon_{zx} \\ 2\varepsilon_{xy} \end{bmatrix} = \begin{bmatrix} 1/E_x & -\nu_{yx}/E_y & -\nu_{zx}/E_z & 0 & 0 & 0 \\ -\nu_{xy}/E_x & 1/E_y & -\nu_{zy}/E_z & 0 & 0 & 0 \\ -\nu_{xz}/E_x & -\nu_{yz}/E_y & 1/E_z & 0 & 0 & 0 \\ 0 & 0 & 0 & 1/G_{yz} & 0 & 0 \\ 0 & 0 & 0 & 0 & 1/G_{zx} & 0 \\ 0 & 0 & 0 & 0 & 0 & 1/G_{xy} \end{bmatrix} \begin{bmatrix} \sigma_{xx} \\ \sigma_{yy} \\ \sigma_{zz} \\ \sigma_{yz} \\ \sigma_{zx} \\ \sigma_{xy} \end{bmatrix} \quad (3-15)$$

where  $E_i$  is the Young's modulus along axis  $i$ ,  $G_{ij}$  is the shear modulus in direction  $j$  on the plane with normal vector in direction  $i$ ,  $\nu_{ij}$  is the Poisson's ratio corresponding to a contraction in direction  $j$  when tension is applied in direction  $i$ . Therefore, the three groups of elastic constants can be derived from the ( $\mathbf{S}$ ) tensor via the following equation:

$$E'_i = \frac{1}{S'_{iii}}, \quad G'_{ij} = \frac{1}{4S'_{ijj}} (i \neq j), \quad \nu'_{ij} = \frac{-S'_{ijj}}{S'_{iii}} (i \neq j) \quad (3-16)$$

where  $i, j$  run over 1, 2, 3.

### 3.2.3 Piezoelectric theory for continuous anisotropic media

According to material mechanics, the general constituent equation for piezoelectric materials can be written as tensor forms



$$\begin{bmatrix} \boldsymbol{\sigma} \\ \mathbf{D} \end{bmatrix} = \begin{bmatrix} \mathbf{c}^E & -\mathbf{e}^T \\ \mathbf{e} & \kappa^\varepsilon \varepsilon_0 \end{bmatrix} \begin{bmatrix} \boldsymbol{\varepsilon} \\ \mathbf{E} \end{bmatrix} \quad (\text{strain-charge form}) \quad (3-17)$$

$$(\text{stress-charge form}), \quad (3-18)$$

where piezoelectric tensors  $d_{ij}$  (stress-charge form) and  $e_{ij}$  (strain-charge form) can

be defined as  $6 \times 3$  tensors, complying to the relation  $D = d\sigma + \kappa^\sigma \varepsilon_0 E$  and  $D$

$= \varepsilon e + \kappa^\varepsilon \varepsilon_0 E$ . The full matrix forms of Eqs. (3-17) and (3-18) are,

$$\begin{pmatrix} \sigma_1 \\ \sigma_2 \\ \sigma_3 \\ \sigma_4 \\ \sigma_5 \\ \sigma_6 \\ D_1 \\ D_2 \\ D_3 \end{pmatrix} = \begin{pmatrix} c_{11}^E & c_{12}^E & c_{13}^E & 0 & 0 & 0 & 0 & 0 & -e_{31} \\ c_{12}^E & c_{22}^E & c_{23}^E & 0 & 0 & 0 & 0 & 0 & -e_{32} \\ c_{13}^E & c_{23}^E & c_{33}^E & 0 & 0 & 0 & 0 & 0 & -e_{33} \\ 0 & 0 & 0 & c_{44}^E & 0 & 0 & 0 & -e_{24} & 0 \\ 0 & 0 & 0 & 0 & c_{55}^E & 0 & -e_{15} & 0 & 0 \\ 0 & 0 & 0 & 0 & 0 & c_{66}^E & 0 & 0 & 0 \\ 0 & 0 & 0 & 0 & e_{15} & 0 & \kappa_1^S \varepsilon_0 & 0 & 0 \\ 0 & 0 & 0 & e_{24} & 0 & 0 & 0 & \kappa_2^S \varepsilon_0 & 0 \\ e_{31} & e_{32} & e_{33} & 0 & 0 & 0 & 0 & 0 & \kappa_3^S \varepsilon_0 \end{pmatrix} \begin{pmatrix} \varepsilon_1 \\ \varepsilon_2 \\ \varepsilon_3 \\ \varepsilon_4 \\ \varepsilon_5 \\ \varepsilon_6 \\ E_1 \\ E_2 \\ E_3 \end{pmatrix} \quad (3-19)$$

and

$$\begin{pmatrix} \varepsilon_1 \\ \varepsilon_2 \\ \varepsilon_3 \\ \varepsilon_4 \\ \varepsilon_5 \\ \varepsilon_6 \\ D_1 \\ D_2 \\ D_3 \end{pmatrix} = \begin{pmatrix} s_{11}^E & s_{12}^E & s_{13}^E & 0 & 0 & 0 & 0 & 0 & d_{31} \\ s_{12}^E & s_{22}^E & s_{23}^E & 0 & 0 & 0 & 0 & 0 & d_{32} \\ s_{13}^E & s_{23}^E & s_{33}^E & 0 & 0 & 0 & 0 & 0 & d_{33} \\ 0 & 0 & 0 & s_{44}^E & 0 & 0 & 0 & d_{24} & 0 \\ 0 & 0 & 0 & 0 & s_{55}^E & 0 & d_{15} & 0 & 0 \\ 0 & 0 & 0 & 0 & 0 & s_{66}^E & 0 & 0 & 0 \\ 0 & 0 & 0 & 0 & d_{15} & 0 & \kappa_1^T \varepsilon_0 & 0 & 0 \\ 0 & 0 & 0 & d_{24} & 0 & 0 & 0 & \kappa_2^T \varepsilon_0 & 0 \\ d_{31} & d_{32} & d_{33} & 0 & 0 & 0 & 0 & 0 & \kappa_3^T \varepsilon_0 \end{pmatrix} \begin{pmatrix} \sigma_1 \\ \sigma_2 \\ \sigma_3 \\ \sigma_4 \\ \sigma_5 \\ \sigma_6 \\ E_1 \\ E_2 \\ E_3 \end{pmatrix}, \quad (3-20)$$

respectively.

In material engineering, the most concerned piezoelectric properties are the stress-charge forms, including the longitudinal piezoelectric constant  $d_{33}$ , transverse



---

piezoelectric constant  $d_{31}$ , shear-deformation piezoelectric constant  $d_{15}$ , as well as the hydrostatic piezoelectric constant  $d_h = d_{31} + d_{33}$ . These constants are important parameters for application of piezoelectricity in sensors, actuators, and transformers. Meanwhile, the strain-charge forms  $e_{ij}$  are rarely seen in experimental studies. However, for completeness, we have considered both for comparison. Interesting results have been found that, while the  $e_{ij}$ s strongly scales with relative densities (log-log relation),  $d_{ij}$ s do not – or in other words,  $e_{ij}$ s are extensive properties,  $d_{ij}$ s are intrinsic ones. The relationship between these two sets of parameters can be derived from Eqs. (3-17) and (3-18) as follows

$$\mathbf{d} = \mathbf{s}^E \mathbf{e} \quad (3-21)$$

The other parameter shown in the matrix, the dielectric constant  $\kappa$ , is found to be just trivially linearly-dependent on the relative density.

### 3.2.4 Boundary Condition Assignments and Constant Extraction

Different from monolithic materials, the boundary conditions applied on meta-atoms with infinite periodicity cannot be assumed as simple “clamped” or “free”. To retain the periodicity, the displacement of six boundaries of each unit cell should conform to the constraints  $u_{i-} = u_{i+}$ , for  $i = x, y$  or  $z$  faces, and  $i-$ ,  $i+$  represent two opposite faces of the same direction, respectively. Specifically, for the “applied strain” condition, the displacements  $u_i$  can be simply defined as



---

---

$$u_i = \varepsilon_{ij}x_j, \quad (3-22)$$

where  $x_j$  are the spatial coordinates of the boundary  $j$ , since the strain tensor  $\varepsilon_{ij}$  is a pre-imposed value. For the “applied stress” condition, however, the strain tensor is undefined, but its average value experienced by a face  $j$  can be calculated as

$$\varepsilon_{ij} = \frac{1}{A_j} \iint \frac{du_i}{dx_j} dA, \quad (3-23)$$

where  $A_j$  denotes the surface area of  $j$ . Combination of Eqs. (3-20) and (3-21) can give out flat boundary surfaces with square-cuboid (for normal strain) or rhombohedral shapes (for shear strain). Practically, the boundaries of unit-cells cannot be strictly flat under internal stress conditions. Therefore, we apply the stimuli at the outermost boundary of the simulation domain, while extract the responses from the unit-cell boundaries, in order to eliminate size aberrancies. For example, in extraction of piezoelectric matrix for the “applied strain” condition, 9 different models with distinct boundary constraints (which are x-normal, y-normal, z-normal, yz-shear, xz-shear, and xy-shear strain constraints respectively) are calculated in sequence. For each model assigned with number  $j$ , we can get a  $9 \times 9$  destination matrix  $D$  with each component  $D_{ij}$  to be the  $i$ th strain-voltage component (which are  $\sigma_1, \sigma_2, \sigma_3, \sigma_4, \sigma_5, \sigma_6, D_1, D_2, D_3$ , respectively, in Voigt notation) retrieved from unit-cell boundaries, and also a source matrix  $S$  with each component  $S_{ij}$  to be the  $j^{\text{th}}$  stress-charge component (which are  $\varepsilon_1, \varepsilon_2, \varepsilon_3, \varepsilon_4, \varepsilon_5, \varepsilon_6, E_1, E_2, E_3$ , respectively) retrieved from unit-cell boundaries. The overall effective piezoelectric matrix  $T$  can then be derived via the matrix quotient.



### 3.2.5 Dataset

For all the studied models, the intrinsic properties of the material are set to be  $E = 1$  for Young's modulus, and  $\nu = 0.3$  for Poisson's ratio. For piezoelectric part, the piezoelectric matrix is set as stress-charge form of

$$\begin{pmatrix} c_{11}^E & c_{12}^E & c_{13}^E & 0 & 0 & 0 & 0 & 0 & -e_{31} \\ c_{12}^E & c_{22}^E & c_{23}^E & 0 & 0 & 0 & 0 & 0 & -e_{32} \\ c_{13}^E & c_{23}^E & c_{33}^E & 0 & 0 & 0 & 0 & 0 & -e_{33} \\ 0 & 0 & 0 & c_{44}^E & 0 & 0 & 0 & -e_{24} & 0 \\ 0 & 0 & 0 & 0 & c_{55}^E & 0 & -e_{15} & 0 & 0 \\ 0 & 0 & 0 & 0 & 0 & c_{66}^E & 0 & 0 & 0 \\ 0 & 0 & 0 & 0 & e_{15} & 0 & \kappa_3 \epsilon_0 & 0 & 0 \\ 0 & 0 & 0 & e_{24} & 0 & 0 & 0 & \kappa_3 \epsilon_0 & 0 \\ e_{31} & e_{32} & e_{33} & 0 & 0 & 0 & 0 & 0 & \kappa_3 \epsilon_0 \end{pmatrix} \quad (3-24)$$

with  $cE_{11} = cE_{22} = cE_{33} = 100$  [GPa],  $cE_{12} = cE_{13} = cE_{23} = 50$  [GPa],  $cE_{44} = cE_{55} = cE_{66} = 20$  [GPa],  $e_{33} = 10$  [C/m<sup>2</sup>],  $e_{31} = e_{32} = -3$  [C/m<sup>2</sup>],  $e_{15} = e_{24} = 7$  [C/m<sup>2</sup>],  $\kappa_1 = \kappa_2 = \kappa_3 = 1000$ ,  $\epsilon_0$  the vacuum permittivity, and from which the intrinsic longitudinal piezoelectric modulus is derived as  $d_{33} = 180$  [pC/N]. It is noted that the ratio  $cE_{33} : e_{33} : \kappa_3$  is about  $10$  [GPa] :  $1$  [C/m<sup>2</sup>] :  $100$ , while too much deviation from this ratio will result in weird results (calculations not shown). As a result, it is impossible to solely define piezoelectricity without defining the electric and dielectric part, which implies intrinsic relationship between these values from the molecular level.



---

---

### 3.3 Scaling behavior of elastic properties

In following sections (section 3.3.1 and 3.3.2), elastic properties and their scaling behavior of the studied metamaterials are plotted as “ $F$  vs.  $\rho$ ” line arrays in Ashby Charts, where  $F$  can stand for previously defined reduced variables of Young’s modulus  $\|E\|$ , shear modulus  $\|G\|_{\max}$ , Poisson’s ratio  $\|v\|$ , or the anisotropy factor  $A^U$  (which is a scalar value despite of directions, defined as  $A^U = 5G_V/G_R + K_V/K_R - 6$ , with  $G_V$ ,  $G_R$ ,  $K_V$ ,  $K_R$  defined in Ref. 20), respectively.

For  $\|E\|$ -,  $\|G\|_{\max}$ - and  $A^U$ - plots, the curves are all plotted in log-log scale, featured by their scaling exponent  $\alpha$ . However, in the  $\|v\|$ - plot the curves can only be drawn in linear form, since  $\|v\|$  is an intensive parameter which cannot scale with the system size. Instead of  $\alpha$ , these curves can be identified by their lower density limits  $v_c$ . Moreover, for the CT and OT models, the effect of anisotropy is also demonstrated, by continuously changing the estimation direction from  $\langle 100 \rangle$  to  $\langle 110 \rangle$  and then to  $\langle 111 \rangle$  in 3-D surface plots. Meanwhile, the “ $F$  vs.  $\rho$ ” plots for  $\langle 100 \rangle$  and  $\langle 111 \rangle$  directions, and the “direction vs.  $F$ ” plots at  $\rho \approx 0.05$  are also shown separately on the side walls of the figure (see later in next sections). A brief introduction of the presentation method is listed as follow.



Table 3-1. List of evaluated parameters.

| <i>parameter</i> | <i>definition</i>                      | <i>section</i> | <i>type</i> | <i>scale type</i> |
|------------------|--|----------------|-------------|-------------------|
| $\ E\ $          | $E_z$                                  | 3.3.1          | extensive   | log-log           |
| $\ G\ _{\max}$   | $\max\{(G_{zx} + G_{zy})/2, \varphi\}$ | 3.3.1          | extensive   | log-log           |
| $\ v\ $          | $(v_{zx} + v_{zy})/2$                  | 3.3.2          | intensive   | linear            |
| $A^U$            | $5G_V/G_R + K_V/K_R - 6$               | 3.3.2          | intensive   | log-log           |

### 3.3.1 Young's Modulus and Shear Modulus

Figs. 3-3 shows the scaling behavior of Young's modulus  $\|E\|$ , shear modulus  $\|G\|_{\max}$ , along the directions  $\langle 100 \rangle$ , respectively. For cubic-symmetric models CT, OT, IF and GR, the six directions of  $\langle 100 \rangle$  are the same, hence only one direction (such as  $[100]$ ) needs to be plotted; for WN and HN models, we choose to plot the value along  $[001]$  directions.

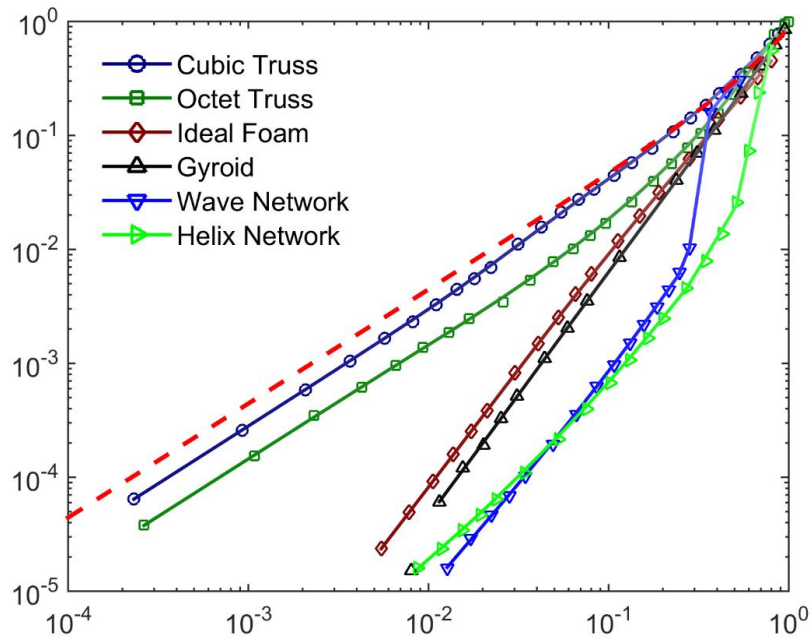


Figure 3-3. Scaling behavior of Young's modulus  $\|E\|$ .

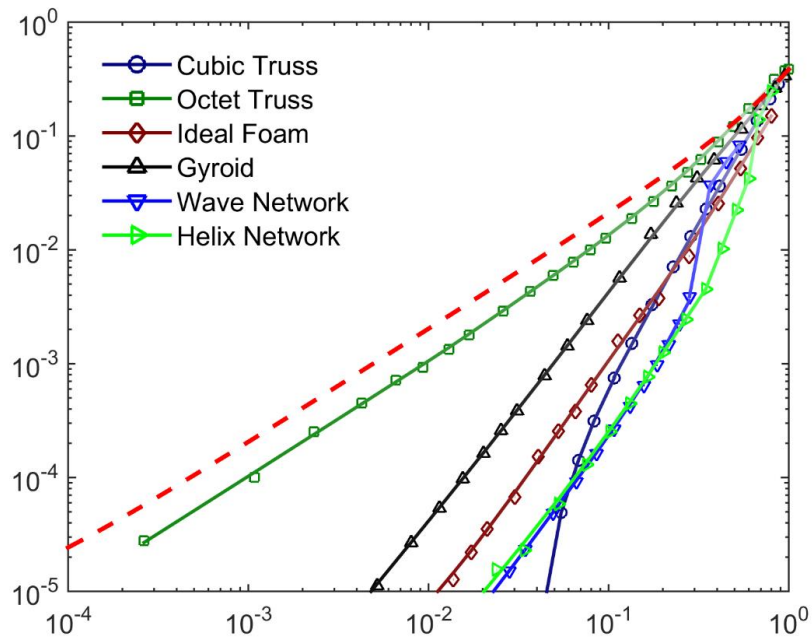


Figure 3-4. Scaling behavior of shear modulus  $\|G\|_{\max}$ .

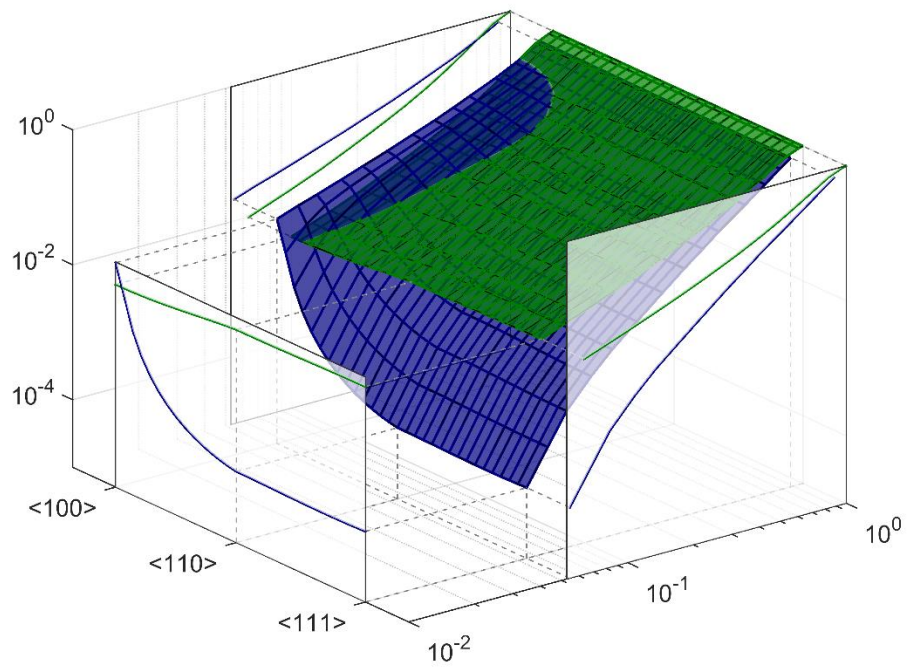


Figure 3-3. Scaling behavior of Young's modulus  $E$  for different directions.

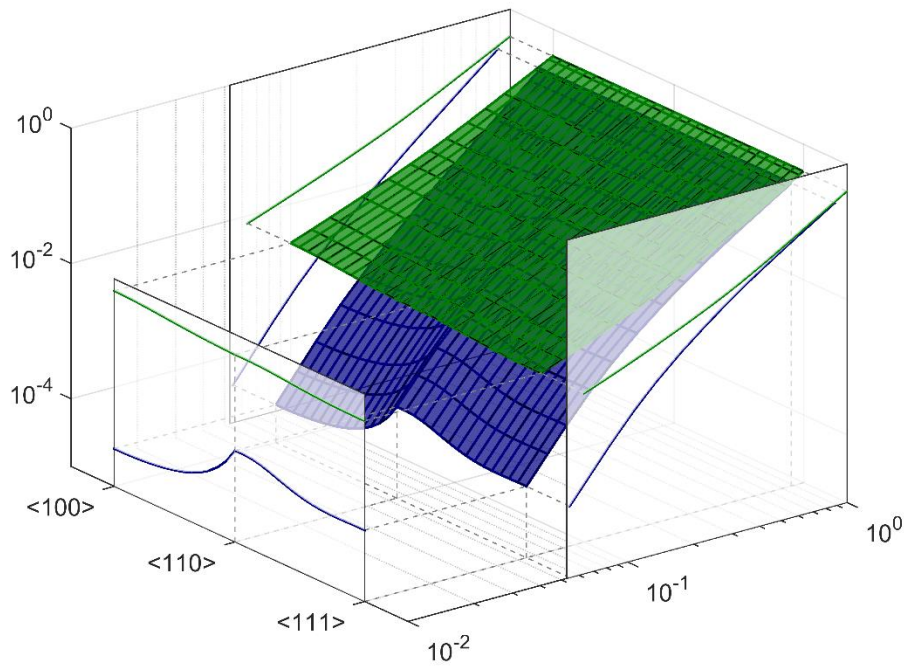


Figure 3-6. Scaling behavior of shear modulus  $G$  for different directions.

From the observation of  $\|E\|$  - and  $\|G\|_{\max}$  - plots the models shown in Figures 3-3 and 3-5 can be classified according to different scaling behaviors, including the “stretching” ( $\alpha \sim 1$ ), “bending” ( $\alpha \sim 2$ ), “intermediate” ( $1 < \alpha < 2$ ), and “cut-off” types (by “cut-off” I mean the curve is no longer a straight-line in the log-log plot). The bending magnitudes for each model have been visualized in Chapter 3.

In Figure 3-4, it is seen that the “cut-off” phenomenon is only observed at directions other than  $\langle 111 \rangle$ , corresponding to the concavity in the symmetry graph in Chapter 3, and the curve changes smoothly from “cut-off” to normal scaling. However, for  $\|G\|_{\max}$  of CT model (Figure 3-6), “cut-off” phenomenon is present for all directions,



---

---

since this model under shear stress is structurally unstable. Evidently, the stiffness of metamaterials is strongly related to the scaling exponent  $\alpha$  – with a smaller  $\alpha$  value corresponding to a greater stiffness (or equivalently, a larger  $\alpha$  corresponding to a larger compliance). However, structural cross-overs can also significantly alter the materials' stiffness, as observed in HN and WN models, at  $\rho = 0.8, 0.85$ , respectively (Figures 4-3 and 4-5). Actually, the main part of “softness” is contributed by this crossover, which make these two models much softer than the “bending” type structure such as IFs at the lower density limit.

The upper bounds of the lines are also plotted, which are defined by the Hashin-Shtrikman (H-S) formula,  $K_{HS} = K_0 + (1 - \nu_0) / [3\nu_0 / (3K_0 + 4G_0) - 1/K_0]$ ,  $G_{HS} = G_0 + (1 - \nu_0) / [6\nu_0(K_0 + 2G_0) / 5G_0 - (3K_0 + 4G_0) - 1/K_0]$  and the elastic relation  $E = 8KG / (3K + G)$ , where  $K$  stands for bulk modulus, subscript “0”, “HS” stand for instinct material property and H-S upper bound, respectively. At the lower density part, the H-S plot is also linear, with a scaling exponent  $\alpha = 1$ ; that means for any models, scaling behavior with  $\alpha < 1$  is impossible. The lower H-S bound is near zero hence omitted in the graph.

### 3.3.2 Poisson's Ratio and Anisotropy Factor

As discussed before,  $\|\nu\|$  - plots cannot be fitted into the scaling formula, but linearly approach definite values  $\nu_c$  at the lower density limits. Accordingly, we can categorize them into 3 types as “over-coupled” ( $\nu_c \geq \nu_0$ , for OT and GR), “de-coupled” ( $\nu_c \sim 0$ , for CT, IF and HN), or “auxetic” ( $\nu_c < 0$ , for WN) types, which means their



lateral responses to normal stresses are enhanced (compared to the monolithic material), diminished, or reversed, respectively. The  $A^U$ -plot demonstrates the magnitude of anisotropy for models, which have been visualized in Fig. 2. They can be coarsely grouped into “isotropic-like” ( $A^U \sim 1$ ), “mildly anisotropic” ( $A^U > 2$ ), and “directed” ones ( $A^U > 100$ ). For the last type the modulus along some direction is much larger than the others by magnitudes, such as  $\langle 100 \rangle$  directions for CT and the  $[001]$  direction for HN. Except for CT, the  $A^U$  of other models also conform to the scaling law. Evidently, the two “over-coupled” models, OT and GR, are identical to the “isotropic-like” models, since mode-coupling of x- and y- displacement can lead to a smoothing out of the anisotropic differences.

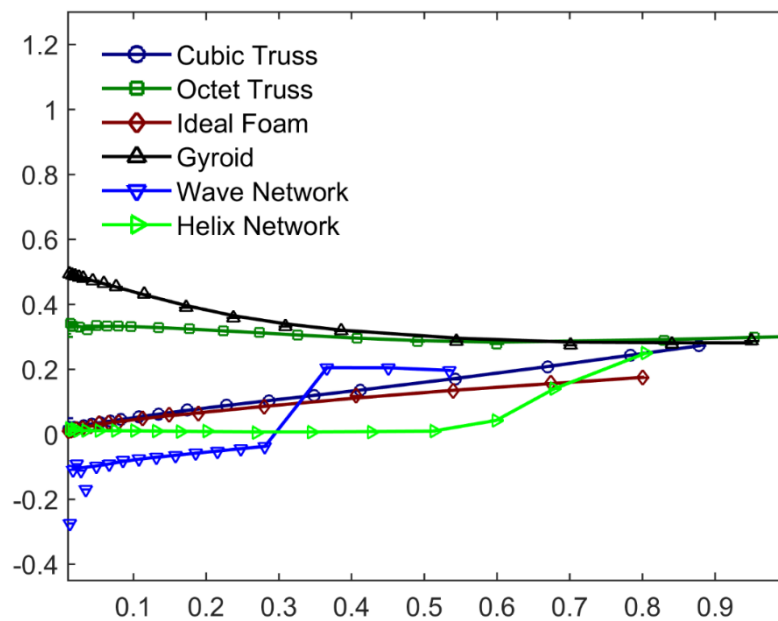


Figure 3-7. Variation of Poisson's ratio (vs. density).

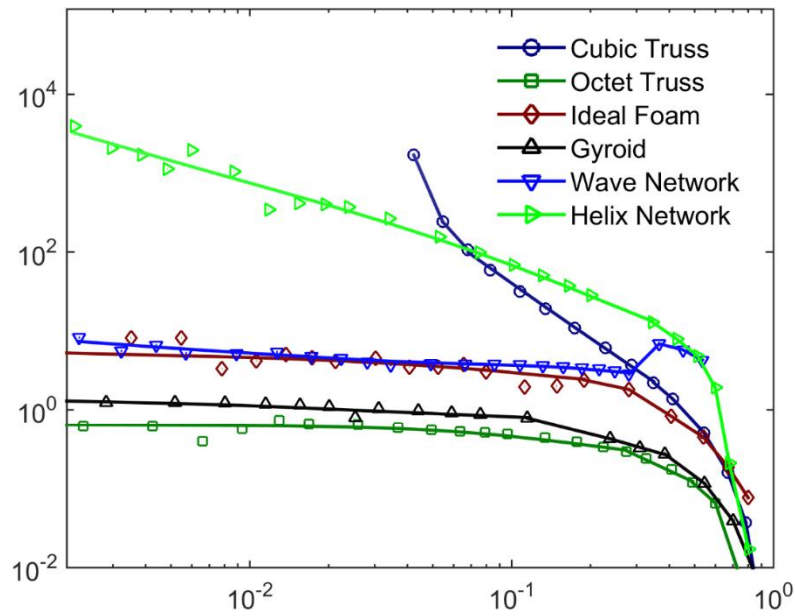


Figure 3-8. Variation of anisotropy factor  $A^U$  (vs. density).

### 3.4 Scaling behavior of dielectric and piezoelectric properties

Different from purely elastic materials which are only concerned for their stiffness or strength, piezoelectric metamaterials are also expected to exhibit excellent performance on electro-mechanical energy conversions. To acquire piezoelectric properties exceeding monolithic ones, various approaches like constructing layered, porous, or particulate piezoelectric composites have been applied. However, in most samples, pores or particulates are randomly distributed while the distribution patterns are not under control (only limited to a few pore shapes and porosity), which has hindered further understanding about the structure-property relationship in piezoelectric foams. In this field, the only work of numerical modelling is Venkatesh *et*



---

---

*al*'s studies on pore shape effects. Although the work is constrained to regular type pores, it has paved the basis for further study of other complex geometries.

### 3.4.1 Poling Directions

Piezoelectric materials are intrinsically anisotropic and the poling direction can significantly influence their apparent properties. For complex architected metamaterials, their internal structures can lead to a non-uniform distribution of poling directions, which would make the situation more complicated. Here we adopted two types of poling distribution, one is the conventional “z-poling” which assumes a uniform distribution of poling directions along the z-axis, the other is the “real-poling”, which resembles the real condition that for each point in space the poling direction is the same as the electric field distribution when a poling voltage is applied on the upper and lower boundary of the structure. Distribution of “real-poling” directions is illustrated in Fig. 4(a). For OT, GR, WN and HN models it can be seen the poling directions are almost along the structure curve, although with a little deviation; while for the other two models, CT and IF – featured with totally straight structures – no significant difference compared with the “z-poling” ones can be found.

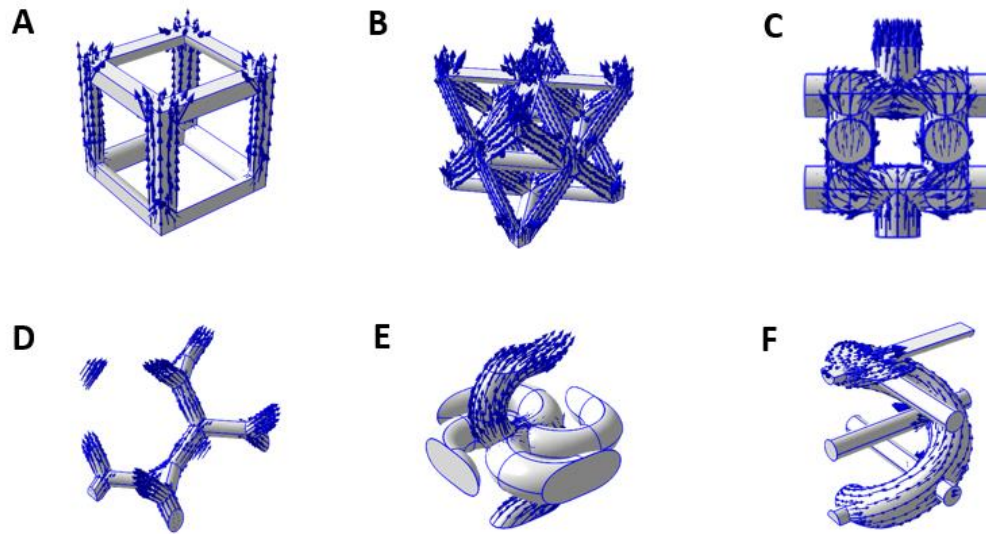


Figure 3-9 Distribution of poling directions under “real-poling” condition.

### 3.4.2 Dielectric Properties

In this section we report our results on the scaling behavior of the dielectric constant  $\kappa_3$  (Figures 3-10 & 3-11). It can be seen that the scaling behavior of  $\kappa_3$  is nearly independent of the structure of metamaterial, as well as of the type of poling employed.

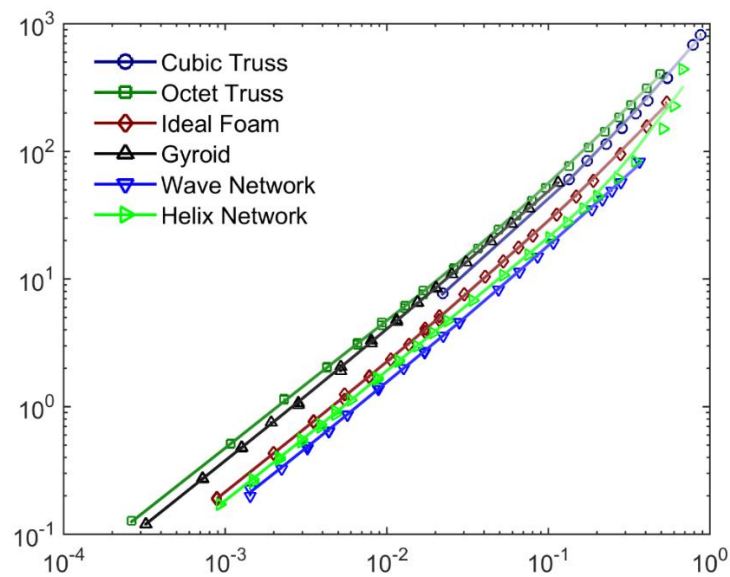


Figure 3-10. Scaling behavior of  $\kappa_3$  for “z-poling” condition.

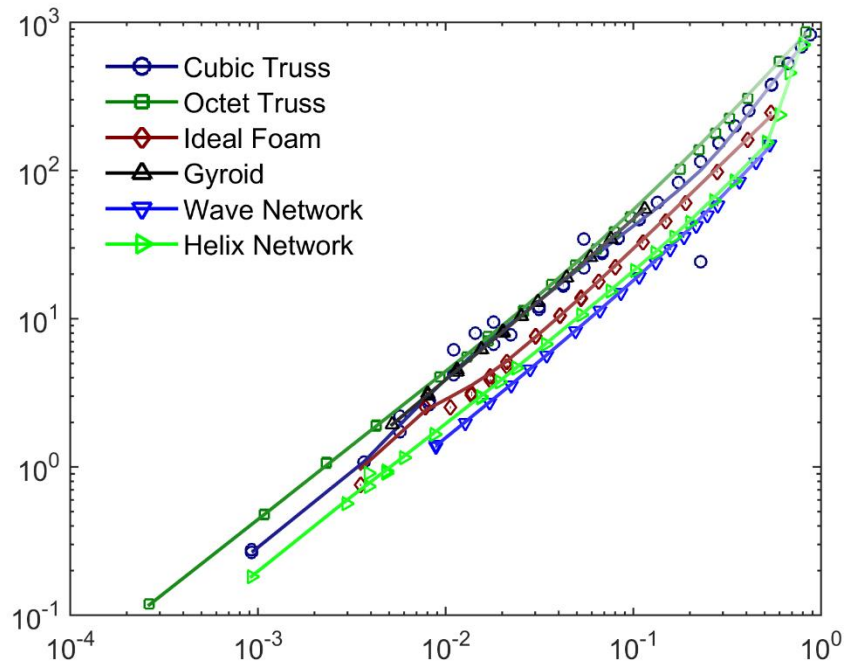


Figure 3-11. Scaling behavior of  $\kappa_3$  for “real-poling” condition.

### 3.4.3 Piezoelectric constants

Similar to the analysis of elastic properties, we demonstrate the symmetry behavior of the reduced variable  $\|d\| = d_{33}$ , while show the scaling behavior of dielectric constant  $\varepsilon^s_3$ , and the strain-charge/stress-charge form of piezoelectric constant  $e_{33}/d_{33}$  in Fig. 5, for all the six geometries.

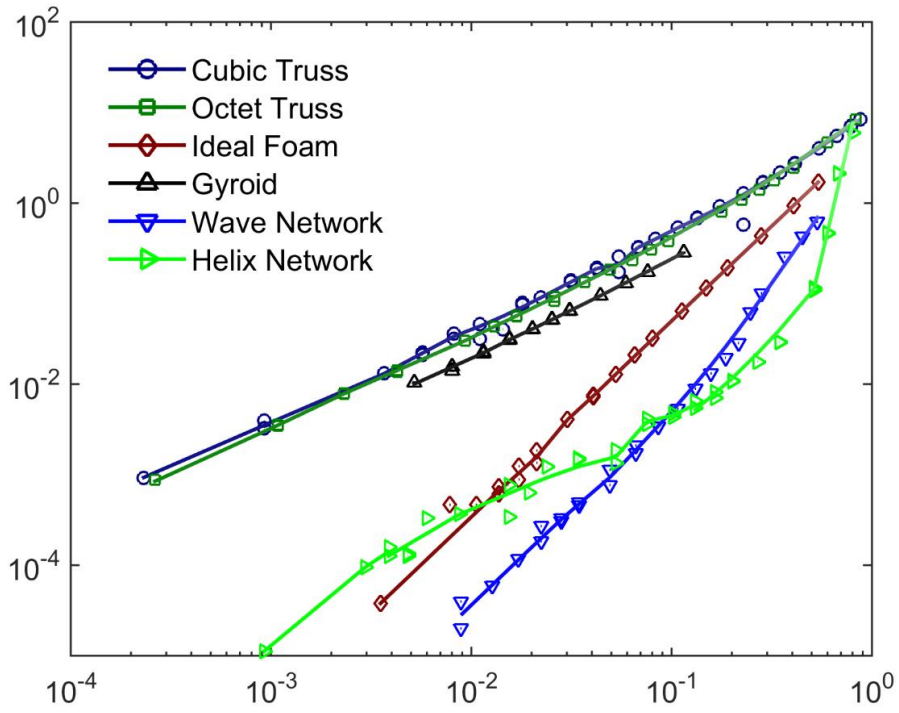


Figure 3-12. Scaling behavior of  $\epsilon_{33}$  for “z-poling” condition.

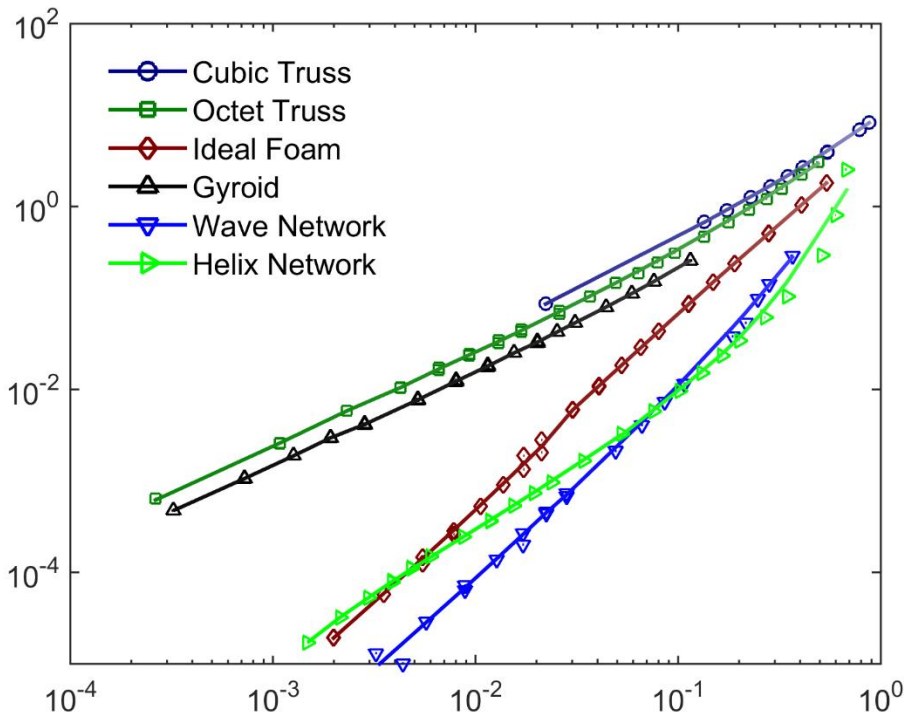


Figure 3-13. Scaling behavior of  $\epsilon_{33}$  for “real-poling” condition.

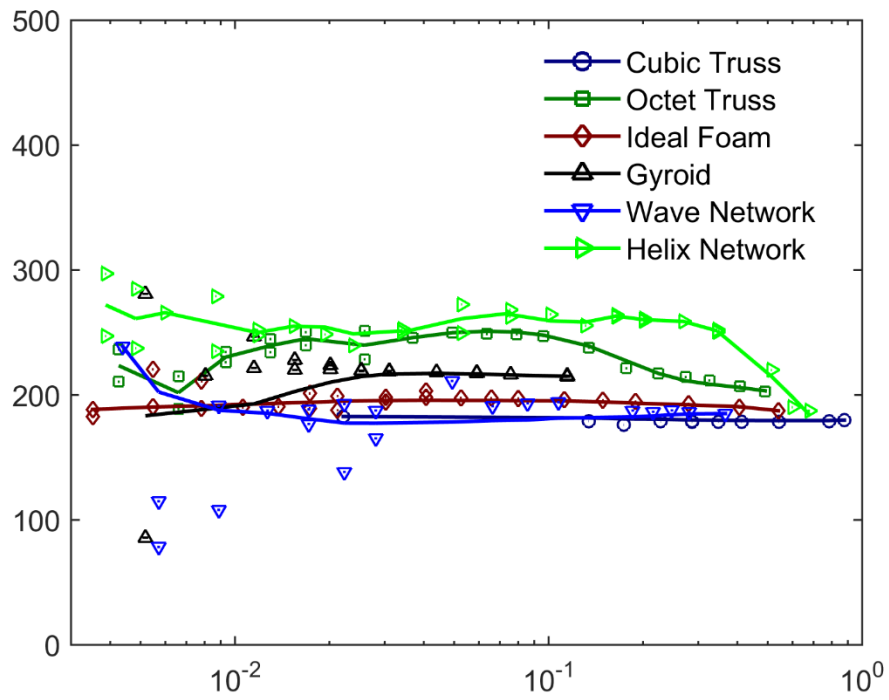


Figure 3-14. Variation of  $d_{33}$  (vs. density) for “z-poling” condition.

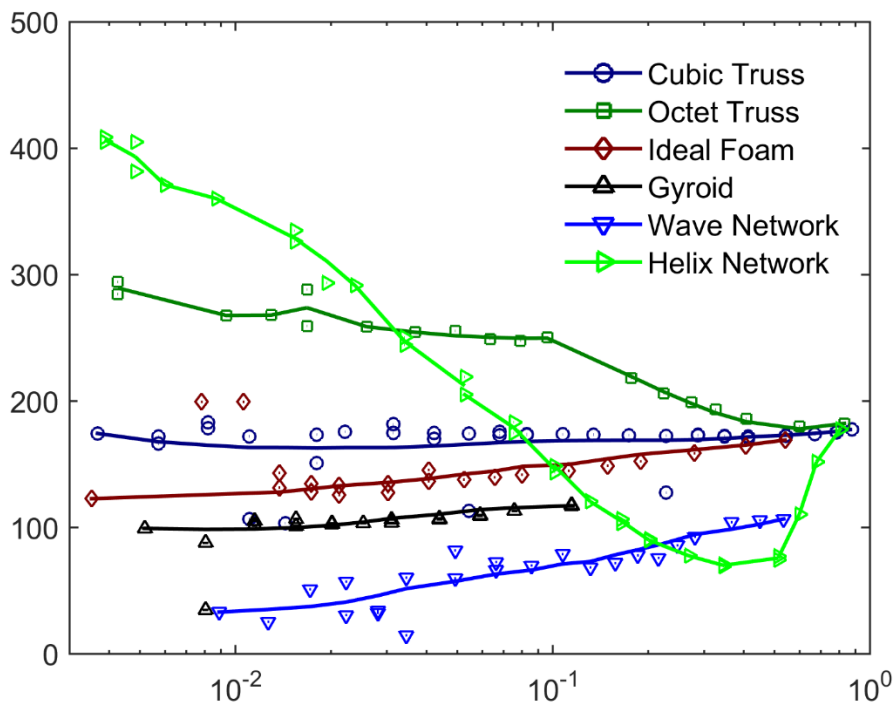


Figure 3-15. Variation of  $d_{33}$  (vs. density) for “real-poling” condition.



---

As shown in Figures 3-12 to 3-15,  $e_{33}$  and  $d_{33}$  are seen to exhibit different type of properties, the former conforms to a scaling behavior, strongly dependent to the relative density; while the other just exhibit limited changes. In practice,  $e_{33}$  is calculated via Eq. (3-2) using the “applied-strain” boundary condition, while  $d_{33}$  is calculated via Eq. (3-3) using the “applied-stress” boundary condition, while the two sets of values can be double-verified by the relation  $\mathbf{d} = \mathbf{s}^E \mathbf{e}$ . Being same as an elastic analysis, two types of scaling behavior have also been identified for  $e_{33}$ , with  $\alpha = 1$  and  $\alpha = 2$ , respectively, where there isn’t much difference between the two types of poling. However, results for  $d_{33}$  are very much different between the two types of poling. In real-poling, the HN model can have a  $d_{33}$  value as high as 400 pC/N of  $d_{33}$  value, which doubles the intrinsic value, thus showing much potential in future applications in ultralight transducers or sensors.

### 3.5 Appendix: scaling behavior of other relative parameters

The above-mentioned constants such as the uniaxial Young’s modulus  $E_z$ , and shear modulus  $G_{xy}$  (in x-y plane), are only parameters characterizing the property of material along one specific direction, which is variable when the angle of inspection changes. Besides, there also exist elastic parameters that can show average material property without specifying any direction, which are  $K_V$  (bulk modulus Voigt average),  $K_R$  (bulk modulus Reuss average),  $G_V$  (shear modulus Voigt average),  $G_R$  (shear modulus Reuss average),  $K_{VRH}$  (bulk modulus VRH average),  $G_{VRH}$  (shear modulus VRH average).



average). Meanwhile, beside the longitudinal piezoelectric constants  $e_{33}$  and  $d_{33}$ , other types of constants are also important for piezoelectric applications, including transverse piezoelectric constants,  $e_{31}$  and  $d_{31}$ , shear piezoelectric constants  $d_{15}$  and  $e_{15}$ , hydrostatic piezoelectric constant  $d_h$ , etc. A list of these parameters are shown below in Tabel 3-5. Fig. 3-6 to Fig. 3-10 have given

Table 3-3. List of evaluation parameters (appendix)

| parameter    | definition   | directional | property type | scale type |
|--------------|--|-------------|---------------|------------|
| $K_V$        | $(C_{11}+C_{22}+C_{33}) + 2(C_{12}+C_{23}+C_{31}) / 9$                               | No          | extensive     | log-log    |
| $K_R$        | $1 / [(s_{11}+s_{22}+s_{33}) + 2(s_{12}+s_{23}+s_{31})]$                             | No          | extensive     | log-log    |
| $K_{VRH}$    | $(K_V + K_R)/2$  | No          | extensive     | log-log    |
| $G_V$        | $[(C_{11}+C_{22}+C_{33}) - (C_{12}+C_{23}+C_{31}) + 3(C_{44}+C_{55}+C_{66})] / 15$   | No          | extensive     | log-log    |
| $G_R$        | $15 / [4(s_{11}+s_{22}+s_{33}) - 4(s_{12}+s_{23}+s_{31}) + 3(s_{44}+s_{55}+s_{66})]$ | No          | extensive     | log-log    |
| $G_{VRH}$    | $(G_V + G_R)/2$  | No          | extensive     | log-log    |
| $\ e_{31}\ $ | $e_{31}$   | Yes         | extensive     | log-log    |
| $\ e_{15}\ $ | $e_{15}$   | Yes         | extensive     | log-log    |
| $\ d_{31}\ $ | $d_{31}$   | Yes         | intrinsic     | linear     |
| $\ d_{15}\ $ | $d_{15}$   | Yes         | intrinsic     | linear     |
| $d_h$        | $d_{33} + d_{31}$  | No          | intrinsic     | linear     |

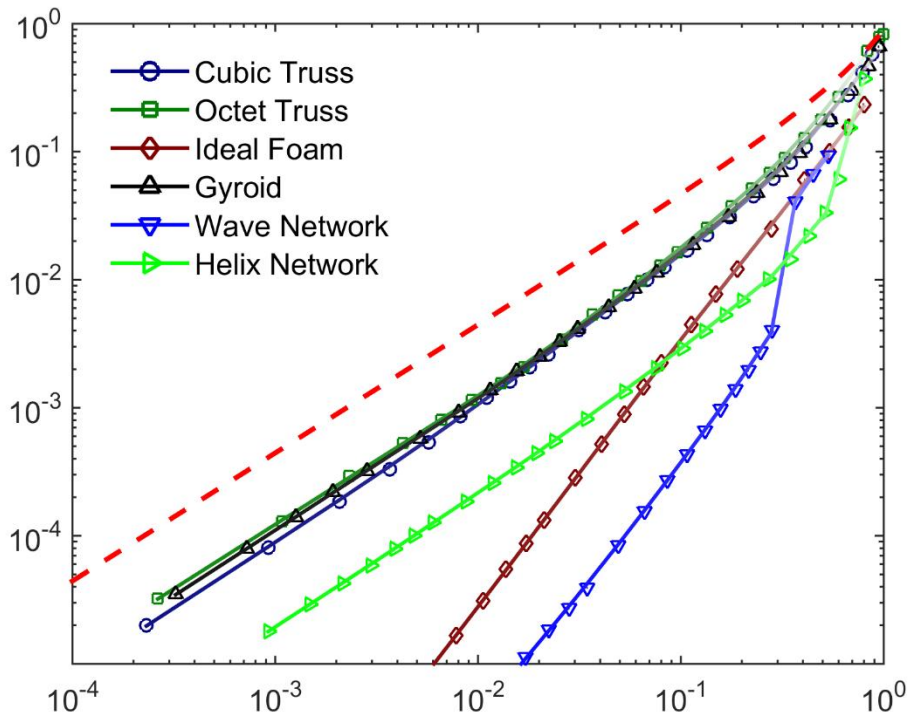


Figure 3-16. Scaling behavior of bulk modulus  $K_{VRH}$ .

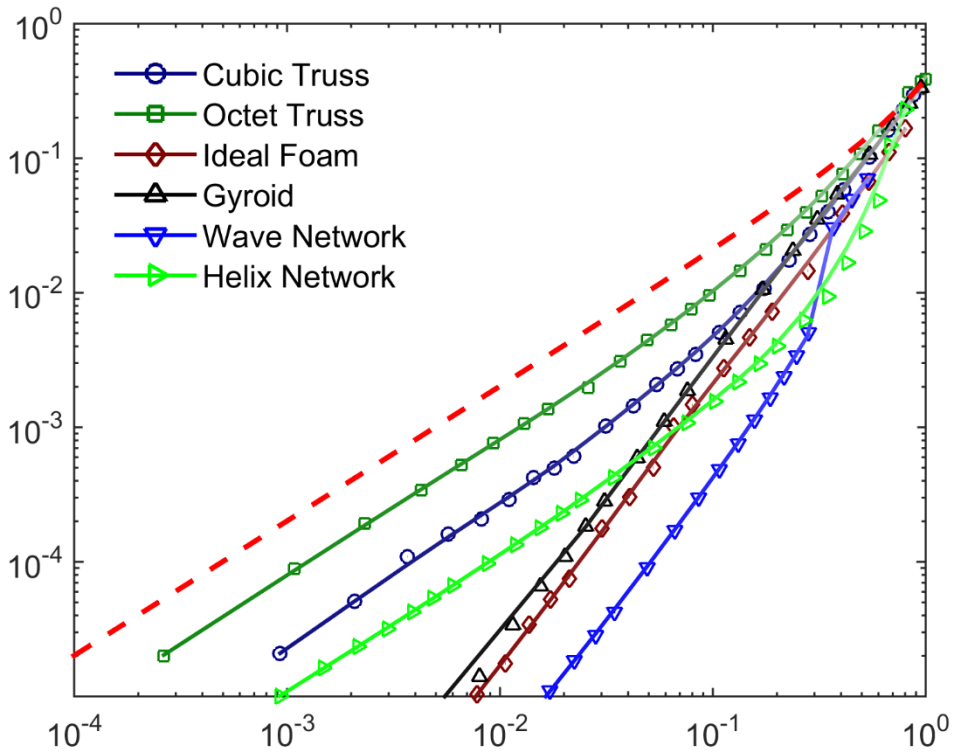


Figure 3-17. Scaling behavior of shear modulus  $G_{VRH}$ .



---

### 3.6 Summary

In summary, the current chapter has made a comprehensive numerical study on the behavior of various elastic, dielectric and piezoelectric properties of different types of metamaterial designs on the variation of the relative density of the structure. Scaling behaviors have been found for the relation between Young's modulus  $E$  (and shear modulus  $G$ , dielectric constant  $\kappa_3$ , piezoelectric constant (strain-charge form)) and  $\rho$ , while scaling exponent  $a$  is distributed between the values of 1 and 2, which indicates the a change of mechanism between “stretching-dominated” and “bending-dominated”. For other constants, include Poisson's ratio  $\nu$ , the anisotropic factor  $A^U$ , and also the piezoelectric constant (stress-charge form)  $d_{33}$ . For the piezoelectric case, we have analyzed two different types of poling condition “real-poling” and “z-poling”, where the electric field distribution inside the structure will change a lot. The  $d_{33}$  value changes a lot between the two types of poling, and by the “real-poling” we have found a super-high  $d_{33}$  value of 400 for the HN model.



---

---

## Chapter 4. Terahertz Properties of Piezoelectric-based Metamaterials

This chapter reports on characterization, simulation and design of piezoelectric metamaterials for terahertz applications. The studied object was focused on Lead magnesium niobate titanate, an important ferroelectric material. In the first part, the terahertz (THz) transmission properties of a  $0.73\text{Pb}(\text{Mg}_{1/3}\text{Nb}_{2/3})\text{O}_3 - 0.27\text{PbTiO}_3$  single crystal were investigated using a time-domain spectroscopy method. Complex refractive index and dielectric dispersion functions were determined from the amplitude and phase information derived from time-domain responses. Based on calculations, it was concluded that the room-temperature dielectric constant of the single crystal equal to  $\sim 30$  at 1 THz. This result could be a useful reference for development of ferroelectric-material-based THz components and devices. In the second part, the design of PMN-PT with microstructural features – which has formed piezoelectric metamaterials, has been designed and simulated, which has shown good performance in Terahertz applications.

### 4.1 Introduction

Solid solutions of lead magnesium niobate–lead titanate (abbreviated as PMN–PT) have attracted extensive interest mainly due to their excellent dielectric, ferroelectric, piezoelectric and pyroelectric properties, and potential applications in the electronic industry. [51] At the morphotropic phase boundary (with PMN: PT (70:30), for example, a PMN–PT single crystal presents an extraordinarily large electromechanical response



---

(piezoelectric coefficient of  $\sim 2500\text{pC/N}$ ) and a low hysteresis behavior, which makes it distinct from and superior to other piezoelectric materials in making high-performance sensors and actuators. [52-55] PMN–PT is also attractive for its puzzling microstructure and rich phase transitions, which lead to complicated dielectric behaviors. In the literature, experiments have been conducted to determine the dielectric constant of PMN–PT over a frequency range from tens of hertz to that of visible light. [58-61] At low frequencies (up to MHz), PMN–PT (both single crystals and polycrystalline) behave either like a normal ferroelectric crystal (when the content of PT is large) or like a relaxor (when the content of PT is small) mainly due to complex domain structures, with a typical dielectric constant of several thousand at room temperature. [62-66] As the frequency increases, the dielectric constant of PMN–PT gradually decreases, followed by a fast drop when the frequency approaches the GHz range, due to the reduced contribution from ferroelectric domains and other structure features. In the infrared and visible frequencies (i.e. the electro-optical behaviors) the value of the relative dielectric constant becomes even smaller. [67-69] The dielectric constant as a function of the direct current (DC) bias, temperature, and time has also been extensively studied. [70-72] Nevertheless, there are few experimental attempts on the dielectric measurement of PMN–PT in the terahertz (THz) range.

THz radiation is an electromagnetic wave with frequency falling in between microwave and infrared radiations. THz technology is believed to hold promises in medical imaging, security detection, nondestructive testing, etc. [73] Due to technical



---

difficulties in generation, detection and modulation of THz waves, however, the study of dielectric behaviors of ferroelectric materials in this frequency range remains rather limited, despite of preliminary results of a few ferroelectric materials (including barium titanate and strontium titanate). [74] More extensive results are required to bridge the gap between microwave and infrared data and to study the soft mode behaviors of these materials. In light of the situation, we chose to work on the THz dielectric characterization of a single crystal of  $0.73\text{Pb}(\text{Mg}_{1/3}\text{Nb}_{2/3})\text{O}_3 - 0.27\text{PbTiO}_3$  using the THz-TDS method.

## 4.2 Terahertz Characterization of PMN-PT

Carefully polished PMN–27PT single crystals of sizes  $5\text{ mm} \times 5\text{ mm} \times 0.4\text{ mm}$  and  $5\text{ mm} \times 5\text{ mm} \times 0.2\text{ mm}$  were used in the experiment. THz transmission measurements were performed at room temperature by using a THz time-domain spectroscopy system (from Ekspla in Lithuania), pumped by a Ti: Sapphire femtosecond laser (Coherent, CA), the working principle of which has been described in the literature. [75] The THz emitter and detector features a microstrip photoconductive antenna fabricated on a low-temperature grown GaAs substrate.

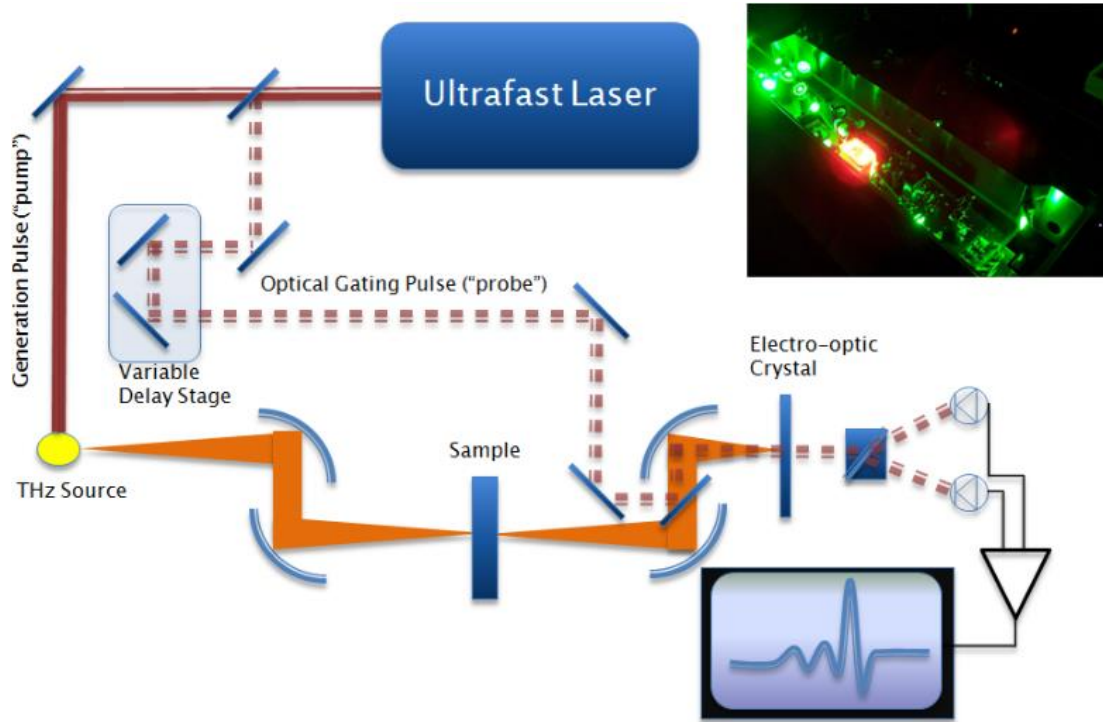


Figure 4-1. Schematics of Terahertz Time-domain Spectroscopy.

The transfer function of a single plate by a normal incidence of THz ray can be formulated as [76]:

$$T(\omega) = \frac{4N}{(1+N)^2} \times e^{-i(N-1)\omega d/c} \times FP(\omega) \quad (4-1)$$

where  $N$  and  $d$  are the complex refractive index and the thickness of the sample plate,  $\omega$  and  $c$  are the angular frequency and the speed of the light,  $FP(\omega)$  is the contribution of Fabry–Perot effects for low absorptive or thin samples, respectively. The transmittance  $T$  can be further resolved into a transmission amplitude  $A$  and a phase delay  $\varphi$ , following  $T = Ae^{i\varphi}$ . Also the complex refractive index  $N$  can be expressed in terms of the refractive index  $n$  and the extinction coefficient  $j$ , as  $N = n - ik$ . The relationship between these values can be derived from Eq. (4-1) as follows:



---

---

$$\phi = \tan^{-1} \left( \frac{\kappa(n^2 + \kappa^2 - 1)}{n[(n+1)^2 + \kappa^2] + 2\kappa^2} \right) - \frac{(n-1)\omega d}{c} + 2p\pi, \quad (4-2)$$

where  $p$  is an arbitrary integer, and

$$\ln A = \ln \left[ \frac{4\sqrt{n^2 + \kappa^2}}{(n+1)^2 + \kappa^2} \right] - \frac{\kappa\omega d}{c}. \quad (4-3)$$

For nondispersive materials, Eqs. (4-2) and (4-3) are both linear with respect to  $x$ , with slopes proportional to  $(n - 1)$  and  $\kappa$ , respectively. These equations are accurate provided:

(1) the generated THz light is a plane wave; (2) both surfaces of the sample plates are optically smooth; (3) the air gaps adjacent to the two ends of samples are long enough and non-absorptive; and (4) the samples are highly absorptive or thick so that the Fabry–Perot effect can be ignored.

The results acquired from THz-TDS are shown in Fig. 4-2, for PMN–PT and air reference, respectively. In Fig. 4-2, the signal to noise ratio is relatively low because of the high absorption of the sample. The original pulse is modulated into two pulses, where the first one is the main pulse, and the second one may be subjected to a weaker birefringence effect (Fabry–Perot effects can be excluded because of the high absorption of the sample plates). A slight DC shift between the two curves can be ignored because it is irrelevant to spectral analysis. In contrast to the thicker sample, measurements on the thinner sample in Fig. 4-3 show lower noise, and perfect consistency.

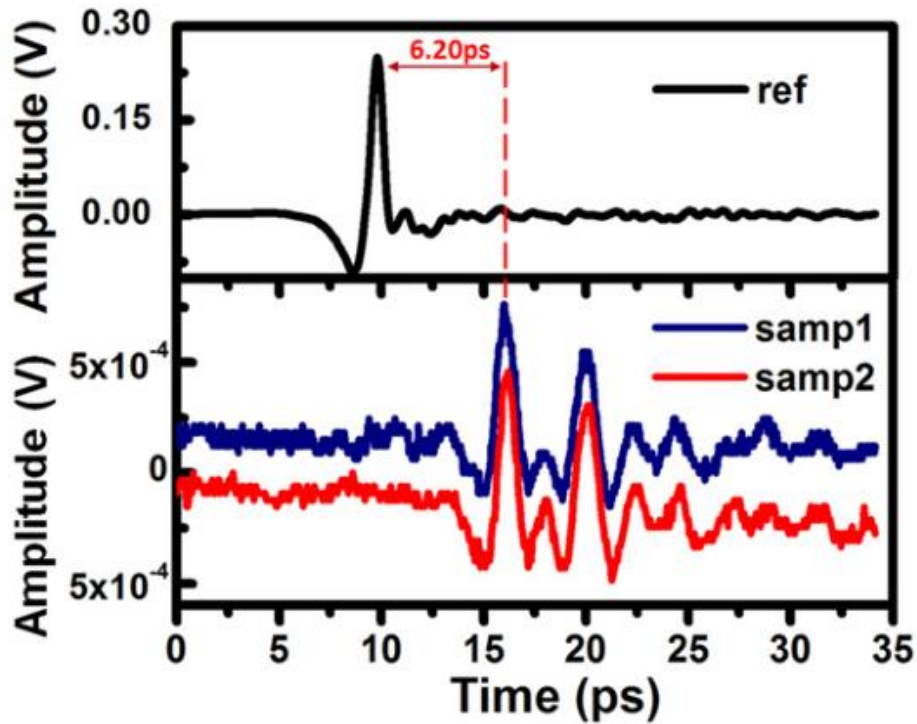


Figure 4-2. The time-domain responses of reference (air) and samples (0.73PMN – 0.27PT single crystals) with thickness of 0.4 mm.

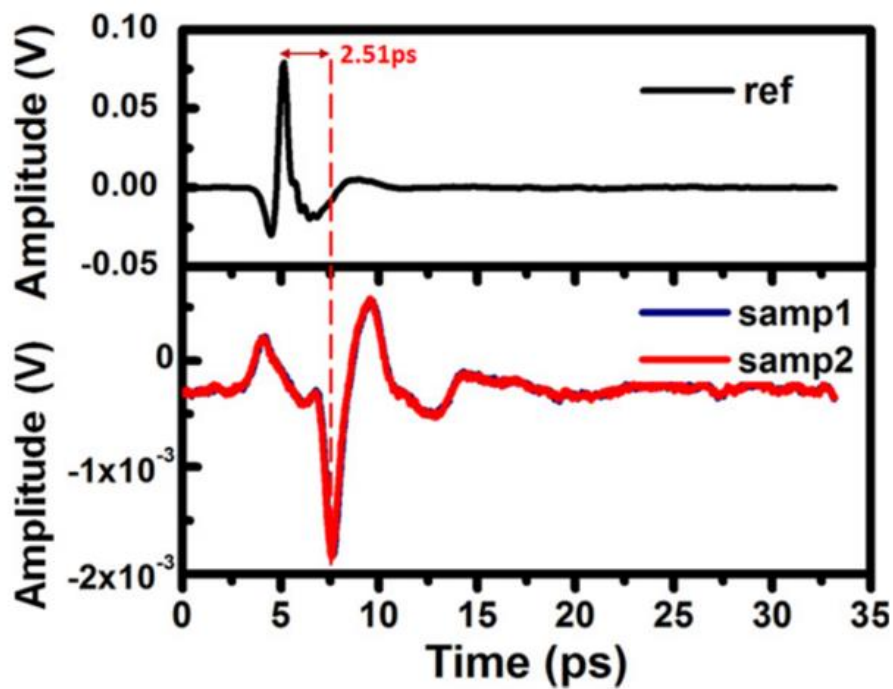


Figure 4-3. The time-domain responses of reference (air) and samples (0.73PMN–0.27PT single crystals) with thickness of 0.2 mm. The two curves almost overlap.



---

---

### 4.3 Estimation of Terahertz Properties for PMN-PT Sample.

One method for estimating the refractive index  $n$  can be derived by considering the time delay  $\Delta t$  of the peak signal caused by the higher refractive index of the sample. The relationship is written as  $n = c\Delta t/d + 1$ , where the thickness  $d$  is 0.4 and 0.2 mm for the two sets of samples. From Fig. 4-2, the time delay (for the main pulse) is 6.20 ps, whereas from Fig. 4-3 it is 2.51 ps, resulting in a value of 5.65 and 4.77, respectively.

The frequency responses are derived from time-domain data by using fast Fourier transform algorithm. As shown in the Fig. 4-3, the amplitude information is shown in the log scale, whereas the phase data are shifted by multiples of  $2\pi$  to ensure that the absolute differences between adjacent values are no more than  $\pi$ . The phase data show an obvious linear dependence at a wide frequency range, which strongly correlates with the second term in Eq. (4-2). Poor linearity out of the frequency range is possibly due to the high dispersion of the material. The linear parts of the data are fitted by dashed lines, the slopes of which are compared with Eq. (4-2), as  $s = 2\pi(n - 1) d/c$ . We found  $s = 39.11$  rad/THz from Fig. 4-3, and  $s = 15.62$  rad/THz from Fig. 4, resulting in another pair of estimation of  $n$ , 5.67 and 4.73. These results are consistent with previous ones derived from time delay. The refractive indices are further substituted into Eq. (4-2), together with values of log amplitudes to estimate the extinction coefficient  $\kappa$ , which is solved using an inverse problem solver “trust-region-dogleg” algorithm built in Matlab software. After that, the two sets of estimations of  $n$  and  $\kappa$  are applied as initial values in solving another inverse problem governed by Eqs. (4-2) and (4-3). To define the



convergence condition, we employ an error function  $d$  for simultaneously fitting the log amplitude and the phase delay as  $\delta(n, \kappa) = (\phi - \phi')^2 + (\ln A - \ln A')^2$ , where  $\phi$  and  $\ln A$  are calculated from Eqs. (4-2) and (4-3) by substituting the initial values of  $n$  and  $\kappa$ , whereas  $\phi_0$  and  $\ln A_0$  are the measurement values, as those presented in Fig. 4-4. [82] This time we apply an Levenberg–Marquardt algorithm, because the target equation system is nonlinear.

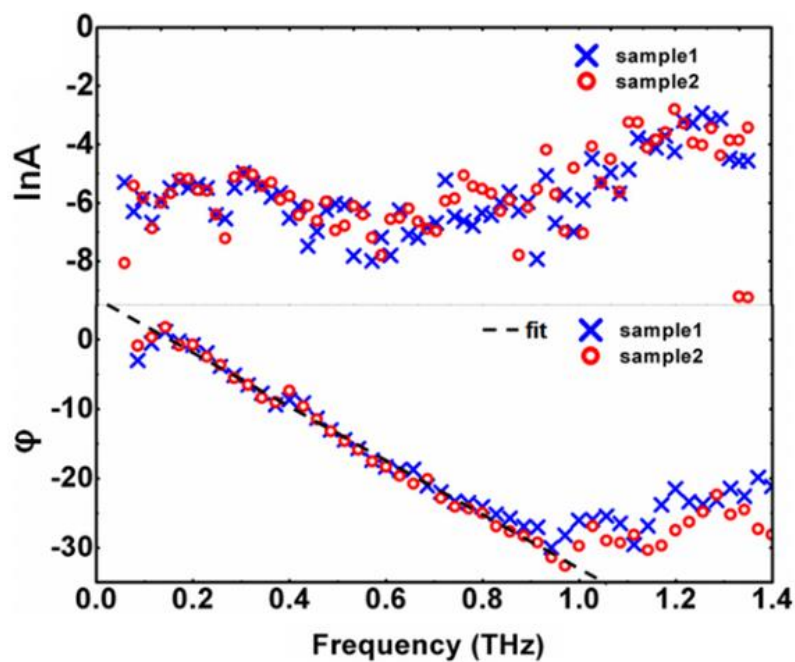


Figure 4-4. The frequency-domain responses of two sets of samples (0.73PMN–0.27PT single crystals) with thickness of 0.4 mm. The lower graph is shifted by a factor of  $2p\pi$  so that they show a linear feature. The dashed lines are linear fits of the phase data.

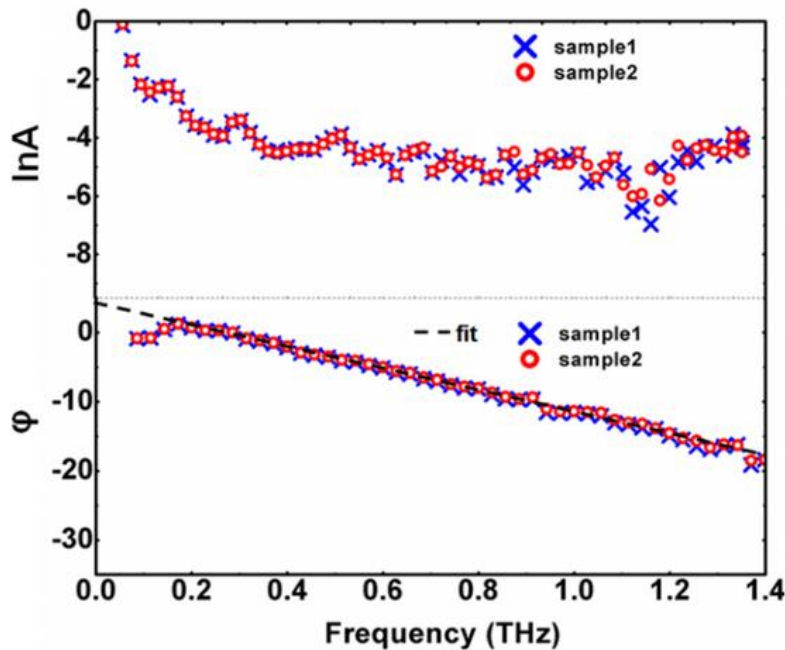


Figure 4-5. The frequency-domain responses of two sets of samples (0.73PMN–0.27PT single crystals) with thickness of 0.2 mm, respectively. The lower graph is shifted by a factor of  $2p\pi$  so that they show a linear feature. The dashed lines are linear fits of the phase data.

The calculated results of  $n$  and  $\kappa$  are shown in Fig. 4-5. Across the frequency range from 0.23 to 1.3 THz, the retrieved values of  $n$  for the four samples are lying at  $5.0 \pm 1.0$ . The values of  $\kappa$  above 0.7 THz are mainly at  $1.0 \pm 0.3$ , and are slightly higher at lower frequencies. The four sets of data are roughly matched with each other at ranges 0.23 ~ 1.3 THz, with small deviations. The deviations are attributed to various disturbances in the measurements, such as scattering effects from the roughness of sample surfaces, or deviations from perfect plane wave condition. The complex dielectric constant  $\varepsilon = N^2 = \varepsilon' - i\varepsilon''$  can also be derived, whose real and imaginative parts are shown in Fig. 4-7. Due to the large divergence, the lower and higher ends of the dielectric function are not included in the calculations. It was found that the value of  $\varepsilon_0$  of our sample is  $\sim 30$ .

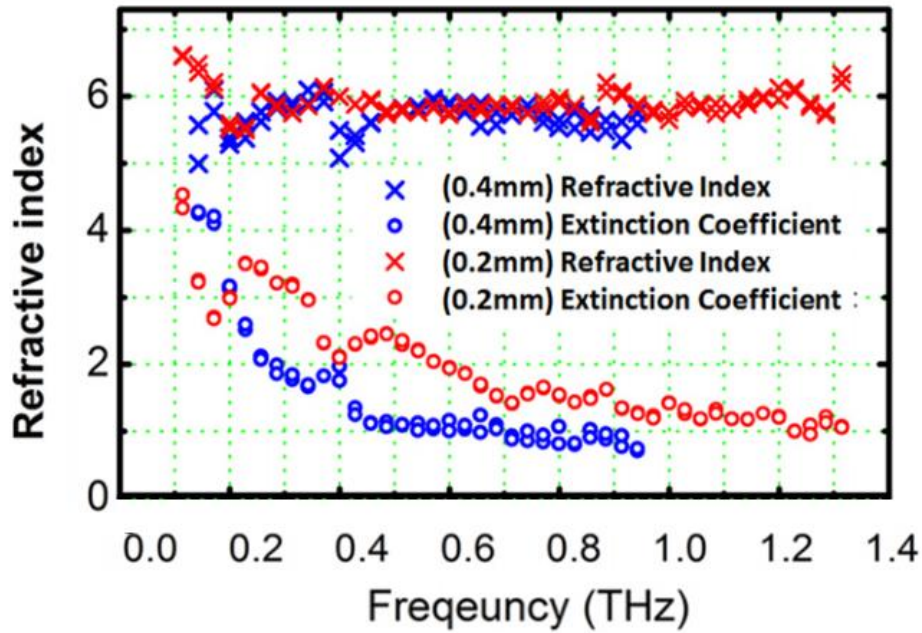


Figure 4-6. The frequency-domain responses of two sets of samples (0.73PMN–0.27PT single crystals) with thickness of 0.2 mm, respectively. The lower graph is shifted by a factor of  $2p\pi$  so that they show a linear feature. The dashed lines are linear fits of the phase data.

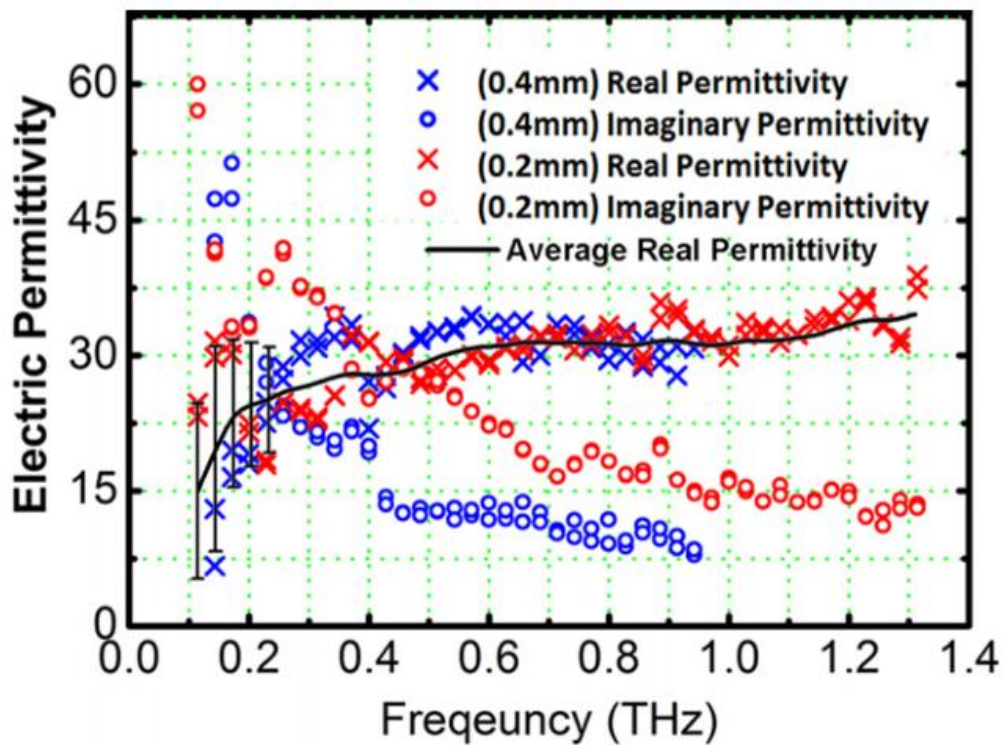


Figure 4-7. The frequency-domain responses of two sets of samples (0.73PMN–0.27PT single crystals) with thickness of 0.2 mm, respectively. The lower graph is shifted by a factor of  $2p\pi$  so that they show a linear feature. The dashed lines are linear fits of the phase data.



---

For perovskite ferroelectrics, the complex dielectric function is governed by phonon vibrations in infrared range, and polar nanoregion (PNR) relaxations in microwave range. Our inspection range (0.1 ~ 1.4 THz) is at the intersection of these two ranges. Previous studies of broadband spectroscopy [70] suggested that, for frequencies near 1 THz, the  $TO_1$  phonon mode (soft mode) is most critical. This mode describes mainly the vibration of Pb cations against the  $BO_6$  octahedra framework, and is generally split into two modes of  $A_1(TO_1)$  (~2.3 THz) and  $E(TO_1)$  (~0.7 THz) due to the rhombohedral symmetry of PNRs at room temperature. At lower ends (~30 GHz), a relaxation mode R1 due to the expansion/shrinking of PNRs also has significant effects on the THz range responses. Due to the complicated mode characteristics, the dielectric constant of PMN–PT can be very sensitive to the composition, crystallinity, and temperature. [73] These may explain why  $\epsilon$  of our PMN–27PT is in same order of but not exactly equal to the  $\epsilon$  (~50) for PMN–29PT in the literature. [74] One possible way to improve the measurement accuracy could be through using ultrathin sample. For example,  $BaTiO_3$  single crystal with a thickness of 32  $\mu\text{m}$  (prepared by  $H_3PO_4$  etching) was used in the literature. [76] For PMN–PT single crystal, however, it is difficult to thin it to this level because of its poor mechanical strength. It is also important all the measurement methods involve multistep data treatments which inevitably could introduce some error. [77-80].

## 4.4 Summary

In summary, we have performed THz-TDS study on a PMN–0.27PT single crystal.



---

The dielectric constant of the material was found to be  $\sim 30$  at 1 THz. This result as well as the measurement methodology could be used as a reference for the future study of THz dielectric behaviors of ferroelectric materials.



---

---

## Chapter 5. Optical Properties of Metal-based Metamaterials

This chapter reports on a simulation and design of nano-sized metallic metamaterials for optofluidic applications. The refractive index sensing properties of plasmonic resonances in gold nanoparticles (nanorods and nanobipyramids) are investigated through numerical simulations. We find that the quadruple resonance in both nanoparticles shows much higher sensing figure of merit (FOM) than its dipolar counterpart, which is attributed mainly to the reduction in resonance linewidth. More importantly, our results predict that at the same sensing wavelength, the sensing FOM of the quadrupole mode can be significantly boosted from 3.9 for gold nanorods to 7.4 for gold nanobipyramids as a result of the geometry-dependent resonance linewidth, revealing a useful strategy for optimizing the sensing performance of metal nanoparticles.

### 5.1 Introduction

Localized surface plasmon resonances (LSPRs) are optical phenomena that occur in metallic nanoparticles in which collective charge motions confined at metal-dielectric interfaces can be driven into a resonant state by an incident light at a given wavelength and polarization state. Their unique properties such as an enhanced absorption or scattering cross section and enhanced local electromagnetic fields make them extremely versatile in a wide range of applications in nanophotonics [75] and biochemical sensing [76]. For example, one typical application of LSPRs is the



---

---

refractive index (RI) sensing, which utilizes the peak shift in the extinction spectrum of metal nanoparticles due to the RI change of the surrounding environment. A widely used figure of merit (FOM) parameter that characterizes the LSPR sensing capability is given by [77,78].

$$FOM = \frac{1}{\Delta\lambda} \frac{d\lambda_{sp}}{dn} \quad (7-1)$$

where  $\lambda_{sp}$  and  $n$  are the resonance wavelength and the surrounding RI, respectively;  $d\lambda_{sp}/dn$  and  $\Delta\lambda$  are the RI sensing sensitivity and the resonance linewidth, respectively. It is well known that the LSPR is highly sensitive to the size, material, and the shape of nanoparticles [91]. This property has triggered a great deal of efforts in the search of optimal nanoparticle geometries for LSPR sensing. In general, it is believed that nanoparticles of irregular shapes perform better than conventional nanospheres, particularly for those with sharp tips [93]. For example, it has been shown that the sensing FOM of gold nanobipyramids (1.7 ~ 4.6) [94] and nanostars (3.8 ~ 10.7) [95] is much larger than that of ordinary shapes such as nanospheres (0.6 ~ 1.5) and nanorods (1.3 ~ 2.1) [96]. However, practical applications are facing a trade-off between synthesis difficulties and the sensing performance, since synthesis of complex morphologies often needs delicate controls over the reaction conditions and usually results in a low reproducibility [97]. Other approaches for better RI sensing include introducing nanocavities [98], or fabricating particularly designed nanoparticles [100], where even more complicated fabrication efforts are required. Therefore, it is beneficial to search for new routes to improve the sensing performance of LSPRs. In the past, LSPR sensing



---

---

studies have mostly focused on the use of the fundamental dipole mode, while higher order resonances have received relatively little attention due to the fact that chemical synthesis tends to produce small-sized (compared to wavelength) nanoparticles. Some pioneering studies on exploration of higher order resonances include dipole-quadrupole interactions [101], Fano resonance [102], and also dipole-propagating mode coupling [103]. In this chapter, we show, through comprehensive numerical studies, that higher order resonances in gold nanoparticles (particularly the quadruple mode in gold nanobipyramids) are significantly superior to dipolar resonances in LSPR sensing, thus avoiding assiduous tailoring of nanoparticle geometries.

The optical properties of gold nanoparticles are solved numerically in the frequency domain using the scattered field formulation. Field analysis was performed using a commercially available finite-element-method package (COMSOL Multiphysics 4.3a). The simulation method has been well documented in [104]. The extinction cross section is simply defined as the sum of absorption and scattering cross sections of the nanoparticles. More specifically, the dielectric function of gold used in the simulations is extracted by interpolation of Johnson and Christy's results [105], and the nanoparticles are placed in a homogeneous medium resembling water, whose RI can be changed from 1.33 to 1.37 for comparison.

## **5.2 Multi-polar plasmonic modes in nanorod-type metamaterials**

Excitations of plasmonic higher order modes such as quadrupole and sextupole



resonances in metallic nanoparticles require a particular incident angle and polarization state. Figure 5-1 shows an angle-dependent excitation of a gold nanorod (length 500 nm, diameter 40 nm) in water ( $n=1.33$ ) by a TM-polarized plane wave.

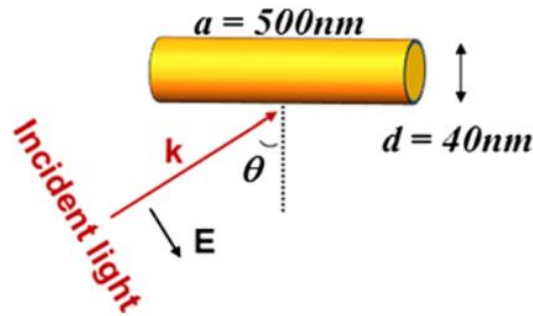


Figure 5-1. The configuration of the numerical modeling. The incident angle for the light is  $\theta$ , the length of the nanorod is  $a = 500\text{nm}$ , while the diameter is  $d = 40\text{nm}$ .

Figure 5-2 renders the extinction spectra of a gold nanorod at different excitation angles, which show three distinct extinction peaks, namely a dipole resonance at 2,060 nm, a quadrupole resonance at 1,030 nm, and a sextupole resonance at 734 nm, respectively. The mode nature of these three extinction resonances is unambiguously confirmed respectively by their near-field distribution (electric field amplitude) and far-field radiation patterns, as shown in Figure 5-3. The extinction spectra shown in Figure 5-2 also reveal that each resonance has an optimal excitation angle at which the extinction cross-section is a maximum. The normalized extinction intensity for each resonance is plotted as a function of the incident angle as shown in Figure 5-4. As expected, the dipole resonance is efficiently excited when the incident polarization is parallel to the nanorod axis. Interestingly, the quadrupole mode responds most strongly to an incident angle at  $40^\circ$ , while the sextupole mode shows double maxima at



excitation angles of  $0^\circ$  and  $55^\circ$ . In fact, these optimal angles correspond, respectively, to the maximum near-field amplitude and far-field radiation power for each resonance presented in Figure 5-3. Other higher order modes and the traverse mode can also be observed at the short wavelength limit, which is out of the scope of this work.

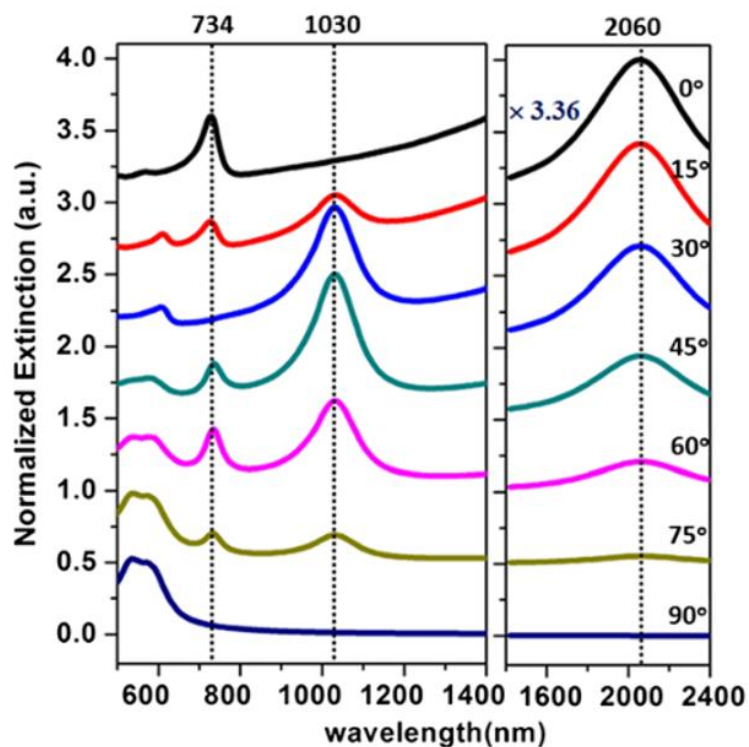


Figure 5-2. Simulated extinction spectra of the gold nanorod for different incident angles  $\theta$ ; the extinction value in the left panel is normalized to the quadrupole peak for  $\theta = 45^\circ$ , and in the right panel to the dipole peak for  $\theta = 0^\circ$  (with a scale 3.36 times larger than the left panel). Curves are plotted with offset for clarity.

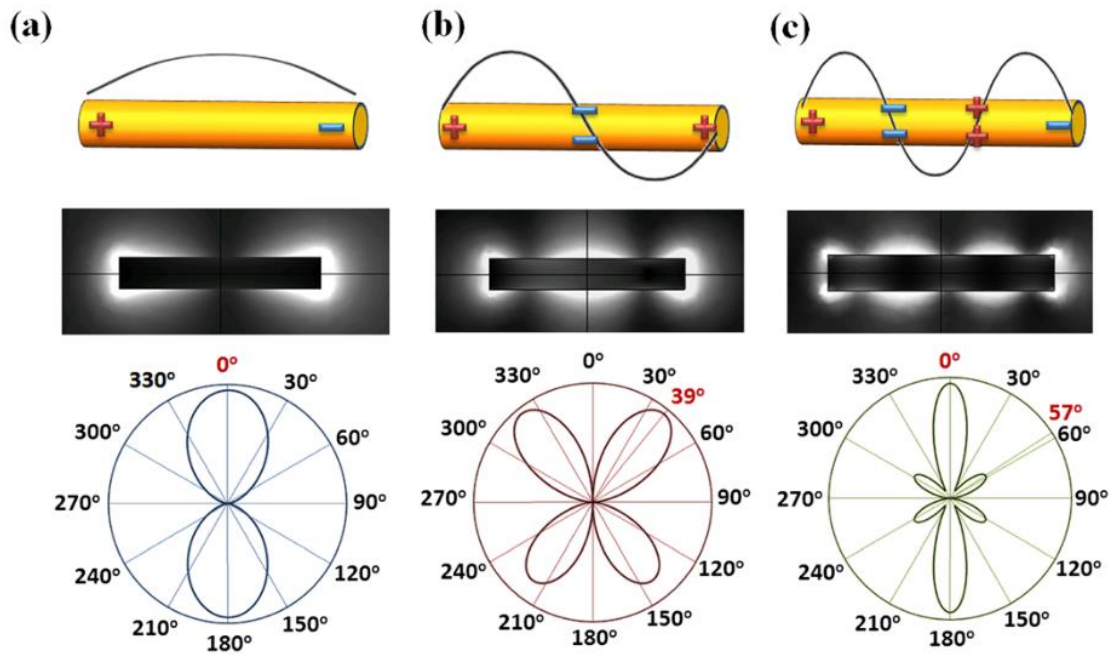


Figure 5-3 Schematic charge distribution, electric near-field amplitude distribution, and far-field scattering radiation pattern of a gold nanorod upon excitations of (a) its dipole mode (2,060 nm), (b) quadrupole mode (1,030 nm), and (c) sextupole mode (734 nm). Red numbers in the scattering patterns indicate the angles with maximal scattering power.

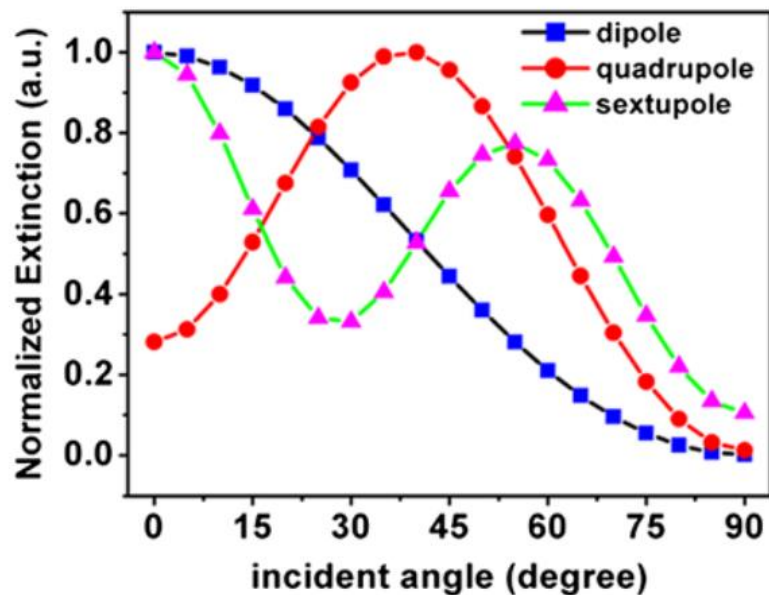


Figure 5-4 Angle-dependent peak extinction for the dipole, quadrupole, and sextupole resonance modes, normalized to the maximum values of each mode.



---

---

### 5.3 Sensitivities of quadrupole resonances

In the following, we will investigate the extinction response of four types of gold nanorods and compare their RI sensing performance. The structures under study are as follows: type A, gold nanorod with  $a = 200$  nm and  $d = 80$  nm; type B, gold nanorod with  $a = 500$  nm and  $d = 80$  nm; type C, gold nanobipyramid with  $a=200$  nm and  $d = 100$  nm; and type D, gold nanobipyramid with  $a = 200$  nm and  $d = 42.5$  nm. The dimensions of these nanorods are chosen such that the dipole resonance wave-length of types A and C and the quadrupole resonance wavelength of types B and D are all around 1,050 nm in order to compare their RI sensing sensitivities at the same wavelength. The geometry of nanobipyramids is selected because of its high FOM as reported previously [106]. To avoid numerical errors caused by the sharp tips and to be more realistic to the experimental samples, the edges of the two tips in nanobipyramids are blunted with a frustum shape.

By changing the RI of the surrounding medium from 1.33 to 1.37 (supposing a fixed incident angle =  $60^\circ$ ), the extinction peak ( $\lambda_{sp}$ ) of each nanorod gradually redshifts towards a longer wavelength, as shown in Figure 5-5 a,b,c,d. These results are summarized in Figure 5-6 in which the extinction peak for each nanorod is plotted as a function of the refractive index. It can be observed from Figure 5-6 that the slopes of the four curves - which directly represent the RI sensitivity  $d\lambda_{sp}/dn$  - are not substantially different from each other, in an obvious contradiction to previous reports [107]. This observation is due to the fact that the RI sensitivity of LSPRs is actually



---

---

wavelength dependent, which means that the RI sensitivity will not depend much on the mode resonance of choice or the structure geometry once the sensing wavelength is fixed (consistent with previous theoretical results by quasi-static approximation [108]). This also points out that it might be inappropriate to compare directly the RI sensitivities of LSPRs of different nanostructures at different wavelengths [109-111]. We also refer to the article [112], where the authors have argued that any single mode sensing of RIs such as LSPR sensing cannot surpass an upper limit of  $\lambda/n$ , where  $\lambda$  is the sensing wavelength and  $n$  is the surrounding RI – which means an upper limit of  $1,050\text{nm}/1.33=789.5$  nanometer per RI unit (nm/RIU) for our case. Therefore, further efforts to improve the RI sensitivity of LSPRs are probably not practical. Accordingly, some results above this theoretical limit obtained from some particular nanostructures such as nanostars [113] may be attributed to a collective excitation of multiple LSPR modes (though in single nanoparticles), or other chemically induced effects. Our calculations also show that the RI sensitivity is independent of  $\theta$  (results not shown here). Therefore, the conclusion from Figure 5-6 must hold true for any incident angles and also for random orientation of nanoparticles.

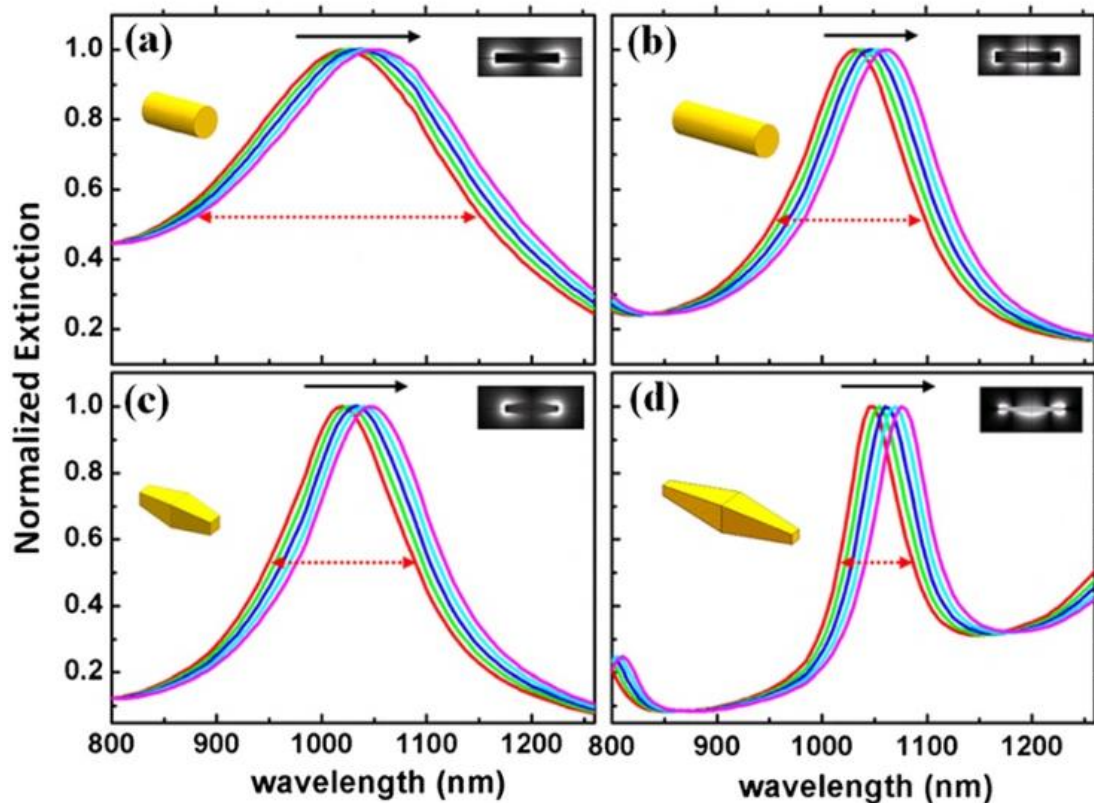


Figure 5-5. RI-dependent extinction spectra. Near the (a & c) dipole resonance mode of nanorods of types A and C and (b & d) quadrupole resonance mode of nanorods of types B and D, respectively, with all the structures in a surrounding medium of RI varying from 1.33 to 1.37. The black arrows represent the shifting direction of the resonance peak from the case RI=1.33 to RI=1.37. The red double arrows denote the linewidth of each peak. Insets are schematics of nanoparticle geometries and their electric near-field amplitude distributions at the corresponding LSPR wavelengths.

## 5.4 Linewidth of quadrupole resonances

As mentioned earlier, the resonance linewidth is the other important factor in determining the overall RI sensing performance of LSPRs [114]. Opposite to the RI sensitivity, the resonance linewidth of LSPRs largely depends on the incident angle, as demonstrated in Figure 5-1b. In addition, for LSPR sensing measurements with typical experimental setups [114], the characterization results are in fact collective effects arising from the total response of a mass of randomly oriented nanoparticles. Therefore, it is necessary to average the linewidth of the simulated extinction spectra at different



excitation angles for each structure.

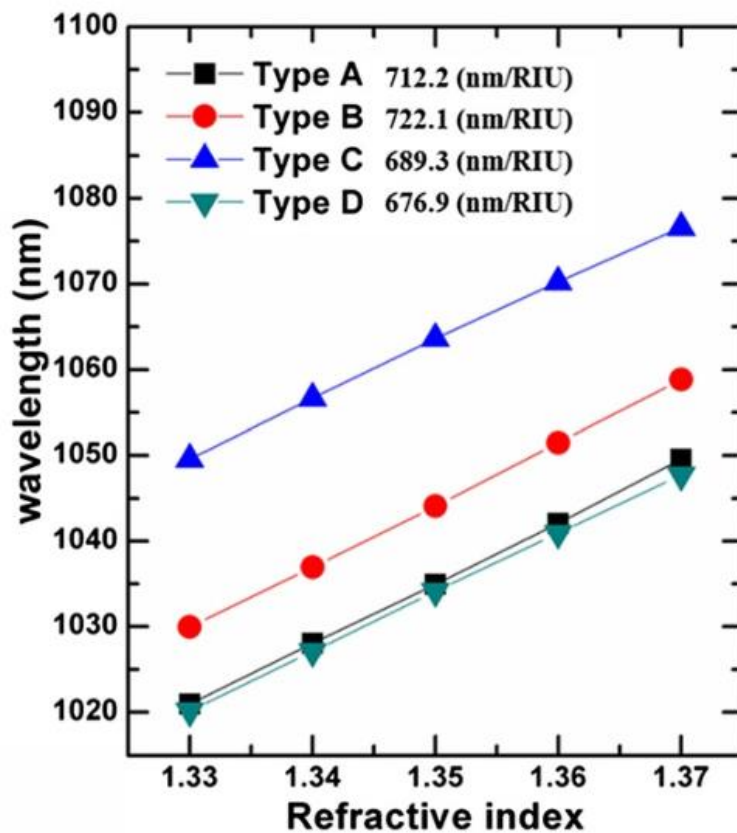


Figure 5-6. Peak wavelengths  $\lambda_{sp}$  as a function of the surrounding RI for different LSPR modes/shapes corresponding to Figure 5-5 (a) to (d). The RI sensitivities  $d\lambda_{sp}/dn$  of the four curves are 712.2, 722.1, 689.3, and 676.9, in the unit of nm/RIU, respectively.

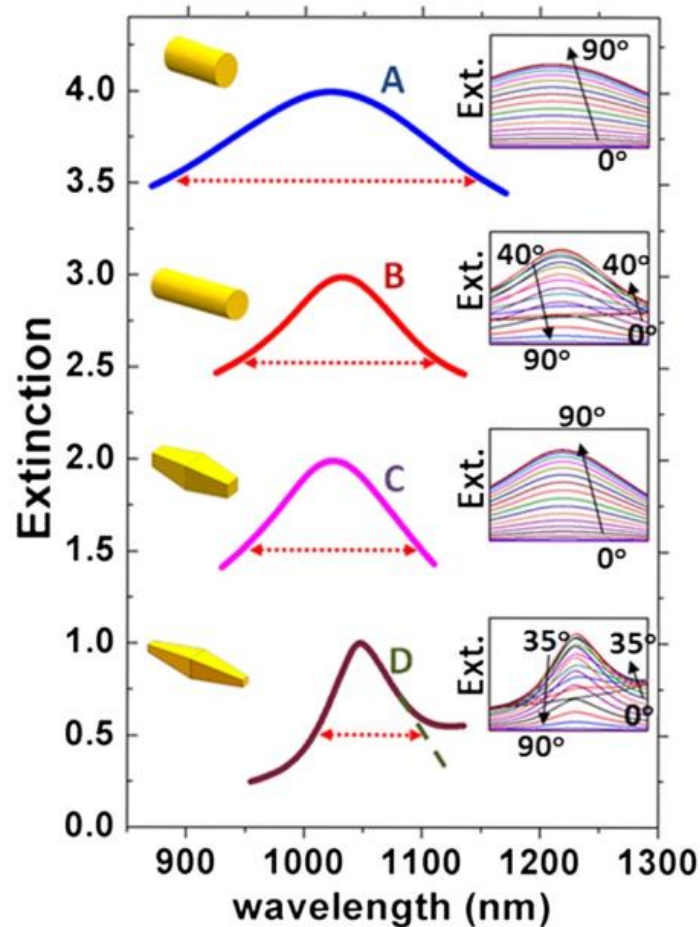


Figure 5-7. Incident angle-averaged extinction spectra. Normalized incident angle-averaged extinction spectra for nanorods of types A, B, C, and D in the wavelength of interest, with surrounding medium of RI=1.33. The red double arrows denote the fullwidth at half maximum linewidth of each peak. For the D curve, the extrapolation line is also shown. The curves are plotted in offset for clarity, with insets showing the schematics of the nanorods (left) and their angle-dependent extinction spectra (right).

The incident angle-dependent extinction spectra for the four types of Au nanorods are presented in the insets of Figure 5-7, and the curves in each inset are summed and averaged for calculating the average resonance linewidth, as shown in the main panel of Figure 5-7. It can be seen that the averaged extinction spectra for nanorods of type A, B, and C are all symmetric with a well-defined resonance linewidth (i.e., full width at half maximum), while the spectrum of type D nanorod exhibits a largely asymmetric profile and needs an extrapolation to extract the resonance linewidth. The resulting



---

---

resonance linewidths for the four nanorods are 278.6, 186.8, 154.1, and 91.7 nm, respectively. An obvious observation is that the resonance linewidth reduces from dipole modes (types A and C) to quadrupole modes (types B and D) and also from regular nanorod shapes to irregular nanobipyramid shapes. Note that the nanobipyramid of type D has the narrowest resonance linewidth, which is due mainly to the coupling between its quadrupole and dipole resonances that are close to each other in wavelength. This possesses similar characteristics to Fano resonances in which the electromagnetic coupling between a dark mode with narrow resonance linewidth and a bright mode with a broad resonance linewidth creates a sharp Fano dip in the spectrum, which can be used to enhance the sensing FOM [114]. A similar coupling effect has also been observed for propagating surface plasmons and waveguide modes in one-dimensional periodic metal grooves [115]. We have to point out that the linewidth reduction observed here may be the main contribution to the reported FOM enhancements [117].

## 5.5 FOM of quadrupole resonances

Finally, we calculated the overall sensing FOM in terms of the RI sensing sensitivity and the extracted resonance linewidth, with results summarized in Table 1 in which some data from literature are also added for reference. For plasmonic dipole modes, the FOM values derived from our numerical methods are partially consistent with previous experimental results. A slightly larger FOM observed for the nanorod dipole mode in our studies may be due to the sharp edges of the rod defined in our



simulation model. For quadrupole modes, we estimated an FOM of 3.9 for the nanorod of type B and 7.4 for the nanobipyramid of type D, both much larger than the FOM values [118] reported for dipole modes in the both structures, suggesting the great promise of using quadruple resonances in single-particle RI sensing.

Table 5-1. Comparison of RI sensing performance for different nanoparticles

| Type              | Mode | Size <sup>a</sup><br>(nm) | $\lambda_{sp}$<br>(nm) | $d\lambda_{sp}/dn^b$ | $\Delta\lambda$<br>(nm) | FOM |
|-------------------|------|---------------------------|------------------------|----------------------|-------------------------|-----|
| Nanorod (A)       | D    | 200/80                    | 1,020                  | 712.2                | 278.6                   | 2.6 |
| Nanorod (B)       | Q    | 500/80                    | 1,030                  | 722.1                | 186.8                   | 3.9 |
| Nanobipyramid (C) | D    | 200/100                   | 1,020                  | 689.3                | 154.1                   | 4.5 |
| Nanobipyramid (D) | Q    | 200/42.5                  | 1,045                  | 676.9                | 91.7                    | 7.4 |
| Nanorod [7]       | D    | 55/16                     | 728                    | 224                  |                         | 2.1 |
| Nanorod [11]      | D    | 50/15                     | 730                    | 170                  | 125                     | 1.3 |
| Nanobipyramid [7] | D    | 189/40                    | 1,098                  | 540                  |                         | 4.5 |
| Nanobipyramid [8] | D    | 90/30                     | 800                    | 352                  |                         | 4.5 |

a. The nanoparticle sizes are expressed in the form of length/diameter. B. The unit for RI sensitivity is nanometers per refractive index unit (nm/RIU). D, dipole mode; Q, quadrupole mode.

## 5.6 Summary

In conclusion, we have demonstrated an ultrahigh overall sensing figure of merit by using plasmonic quadrupole resonances in gold nanorods and nanobipyramids. Three important conclusions can be drawn from our detailed numerical studies: 1) The excitation efficiency of LSPRs in nanorods by plane waves exhibits an angle-dependent behavior, which is consistent with their electric near-field enhancements and far-field scattering radiation patterns. 2) The refractive index sensitivity of single-mode LSPR in nanoparticles is independent of the resonance mode of choice and the particle



---

geometry provided that the sensing wavelength is fixed. 3) The improved FOM observed for plasmonic quadrupole resonances in gold nanoparticles in the present work as well as in previous studies is due mainly to the reduction of resonance linewidth. Our results suggest that plasmonic quadrupole modes in gold nanorods are possibly the most promising choice to achieve the best sensing performance and that it is of particular importance to explore multipolar resonances for further sensing studies.



---

---

## Chapter 6. Conclusion and future work

### 6.1 Conclusion

In the course of this study, several aspects of metamaterials and applications in microwave engineering have been investigated both theoretically and experimentally, aiming to pursue the structure-electromagnetic performance relationship in these materials and develop metamaterials-based microwave devices. Through simulation and/or experiments, the following conclusions have been achieved:

1) Elastic tensors have been found to be more symmetric than their geometric counterparts – the elastic properties can exhibit cubic symmetry even though the original geometry is not cubic; the different elastic tensors of any models share the same type of elastic symmetry; for the WN model, auxeticity occurs only along specific directions.

2) We have made a comprehensive numerical study on the behavior of various elastic, dielectric and piezoelectric properties of different types of metamaterial designs on the variation of the relative density of the structure. Scaling behaviors have been found for the relation between Young's modulus  $E$  (and shear modulus  $G$ , dielectric constant  $\epsilon_3$ , piezoelectric constant (strain-charge form)) and  $\rho$ , while scaling exponent  $a$  is distributed between the values of 1 and 2, which indicates the a change of mechanism between “stretching-dominated” and “bending-dominated”. For other constants, include Poisson's ratio  $\nu$ , the anisotropic factor  $AU$ , and also the piezoelectric constant (stress-charge form)  $d_{33}$ . For the piezoelectric case, we have



---

---

analyzed two different types of poling condition “real-poling” and “z-poling”, where the electric field distribution inside the structure will change a lot. The  $d_{33}$  value changes a lot between the two types of poling, and by the “real-poling” we have found a super-high  $d_{33}$  value of 400 for the HN model.

3) We have performed THz-TDS study on a PMN–0.27PT single crystal. The dielectric constant of the material was found to be  $\sim 30$  at 1 THz. This result as well as the measurement methodology could be used as a reference for the future study of THz dielectric behaviors of ferroelectric materials. Besides, we have formed metamaterial patterns on the PMN-PT substrate which can alter the dielectric responses by 11%.

4) We have demonstrated an ultrahigh overall sensing figure of merit by using plasmonic quadrupole resonances in gold nanorods and nanobipyramids. The excitation efficiency of LSPRs in nanorods by plane waves exhibits an angle-dependent behavior, which is consistent with their electric near-field enhancements and far-field scattering radiation patterns. The refractive index sensitivity of single-mode LSPR in nanoparticles is independent of the resonance mode of choice and the particle geometry provided that the sensing wavelength is fixed. The improved FOM observed for plasmonic quadrupole resonances in gold nanoparticles in the present work as well as in previous studies is due mainly to the reduction of resonance linewidth.



---

---

## 6.2 Future work

Metamaterials is believed to be a promising science topic that is able to revolutionize the current technology. Despite of progress made in these years, a comprehensive picture for the structure-property relationship of different metamaterial designs is still unclear. The author would suggest that, in the future, based on the research work of the current thesis, the investigation about the structure-property relationship should be extended to a wider range of properties, such as thermal properties and thermoelectric properties for application in heat exchange and energy harvesting, chemical absorption properties for  $H_2$  or CO for energy storage,  $Li^+$  density for energy capacity, piezoelectric-ferromagnetic coupling properties for magnetic sensing, and also for dielectric constant/refractive index for exploration of extremes of optical tuning capacity. The study should also be extended to a wider range of structure types, including all types of regular or irregular shapes. For example, irregular shapes include conventional models of foams, fiber networks and aerogels, regular shapes include new origami designs, computer-aided digital designs, and various types of fractal designs.



---

---

## REFERENCE

- [1] Zheng, X. Y. et al. Ultralight, ultrastiff mechanical metamaterials. *Science* 344, 1373-1377 (2014)
- [2] Ashby, M. Hybrid materials to expand the boundaries of material-property space. *J. Am. Ceram. Soc.* 94, S3-S14 (2011).
- [3] Schaedler, T. A., Jacobsen, A. J. & Carter, A. J. Toward lighter, stiffer materials. *Science* 341, 1181-1182 (2013)
- [4] Schaedler, T. A. et al. Ultralight metallic microlattices. *Science* 334, 962-965 (2011).
- [5] Meza, L. R., Das, S. & Greer, J. R. Strong, lightweight, and recoverable three-dimensional ceramic nanolattices. *Science* 345, 1322-1326 (2014).
- [6] Bauer, J., Hengsbach, S., Tesari, I., Schwaiger, R. & Kraft, O. High-strength cellular ceramic composites with 3D microarchitecture. *PNAS* 111, 2453-2458 (2014).
- [7] Bababee, S. et al, 3D soft metamaterials with negative Poisson's ratio. *Adv. Mater.* 25, 5044-5049 (2013).
- [8] Valdevit, L., Jacobsen, A. J., Greer, J. R. & Carter, W. B. Protocols for the Optimal Design of Multi-Functional Cellular Structures: From Hypersonics to Micro-Architected Materials. *J. Amer. Ceram. Soc.* 94, 1-20 (2011).
- [9] Schaedler, T. A. et al. Designing metallic microlattices for energy absorber applications. *Adv. Eng. Mater.* 16, 276-283 (2014).



- 
- [10] <https://www.whitehouse.gov/mgi>
- [11] By “material configuration”, it means both the material composition (the actual )
- [12] de Jong, M. et al. Charting the complete elastic properties of inorganic crystalline compounds. *Sci. Data* 2, 150009 (2015).
- [13] de Jong, M. Chen, W. Geerlings, H. Asta, M & Persson, K. A. A database to enable discovery and design of piezoelectric materials. *Sci. Data* 2, 150053 (2015).
- [14] Liu, W. et al. Processing and properties of porous PZT ceramics from particle-stabilized foams via gel casting. *J. Am. Ceram. Soc.* 96, 1827 (2013).
- [15] Uchino, K. *Ferroelectric Devices* (2nd Edition), CRC Press Inc. (2009).
- [16] Taunaumang, H., Guy, I. L., Chan, H. L. W. Electromechanical properties of 1-3 piezoelectric ceramic/piezoelectric polymer composites. *J. Appl. Phys.* 76, 484 (1994).
- [17] Marselli, S. et al. Porous piezoelectric ceramic hydrophones. *J. Acoust. Soc. Am.* 106, 733 (1999).
- [18] Fan, H. Y. Modulus-density scaling behavior and framework architecture of nanoporous self-assembled silicas. *Nat. Mater.* 6, 418 (2007).
- [19] Deshpande, V. S., Fleck, N. A. & Ashby, M. F. Effective properties of the octet-truss lattice material. *J. Mech. Phys. Solids* 49, 1747 (2001).
- [20] Deshpande, V. S., Ashby, M. F., Fleck, N. A. Foam topology: bending versus stretching dominated architectures. *Acta Mater.* 49, 1035 (2001).
- [21] Roberts, A. P. & Garboczi, E. J. Elastic properties of porous ceramics, *J. Am.*



- 
- Ceram. Soc. 83, 3041-3048 (2000).
- [22] Turley, J. & Sines, G. The anisotropy of Young's modulus, shear modulus and Poisson's ratio in cubic materials. *J. Phys. D: Appl. Phys.* 4, 264-271 (1971).
- [23] Damjanovic, D., Budimir, M., Davis, M. & Setter, N. Piezoelectric anisotropy: enhanced piezoelectric response along nonpolar directions in perovskite crystals. *J. Mater. Sci.* 41, 65-76 (2006).
- [24]
- [25] Malgrange, C., Ricolleau, C. & Schlenker, M. *Symmetry and Physical Properties of Crystals*. Springer Netherlands (2014).
- [26] Greaves, G. N., Greer, A. L., Lakes, R. S. & Rouxel, T. *Nat. Mater.* 10, 823-837 (2011).
- [27] Smith, C. W., Grima, J. N. & Evans, K. E., *Acta Mater.* 48, 4349-4356 (2000).
- [28] Broedersz, C. P., Mao X., Lubensky, T. C. & MacKintosh, F. C. Criticality and isostaticity in fibre networks. *Nat. Phys.* 7, 983-987 (2011).
- [29] Wilhelm, J. & Frey E. Elasticity of stiff polymer networks. *Phys. Rev. Lett.* 91, 108103 (2003).
- [30] Hashin, Z. & Shtrikman, S. A variational approach to the elastic behavior of multiphase materials. *J. Mech. Phys. Solids.* 11, 127-140 (1963).
- [31] Bisegna, P. & Luciano, R. Variational bounds for the overall properties of piezoelectric composites. *J. Mech. Phys. Solids*, 44, 583-602 (1996).
- [32] Yin, J., Li, X., Zhou, J. & Guo, W. Ultralight three-dimensional boron nitride foam with ultralow permittivity and superelasticity. *Nano Lett.* 13, 3232-3236



---

(2013).

- [33] Krause, B. et al. Ultralow-k dielectrics made by supercritical foaming of thin polymer films. *Adv. Mater.* 14, 1041-1046 (2002).
- [34] Choy, T. C., *Effective Medium Theory: Principles and Applications* (2nd Edition), CPI Group (UK) Ltd. (2016).
- [35] Newnham, R. E, Skinner, D. P & Cross, L. E. Connectivity and piezoelectric-pyroelectric composites. *Mater. Res. Bulletin* 13, 525-536 (1978).
- [36] Pilgrim, S. M., Newnham, R. E. & Rohlfiing, L. L. An extension of the composite nomenclature scheme. *Mater. Res. Bulletin* 22, 677-684 (1987).
- [37] Curtarolo, S. et al. The high-throughput highway to computational materials design. *Nat. Mater.* 12, 191-201 (2013).
- [38] Jain, A. et al. Commentary: the materials project: a materials genome approach to accelerating materials innovation. *APL Mater.* 1, 011002 (2013).
- [39] AP Roberts, EJ Garboczi. Elastic properties of model random three-dimensional open-cell solids, *J. Mech. Phys. Solids* (2002) 50, 33
- [40] AP Roberts, EJ Garboczi. Elastic moduli of model random three-dimensional closed-cell cellular solids/ AP Roberts, EJ Garboczi, *Acta Mater.* (2001) 49, 189
- [41] “Mechanical structure-property relationship of aerogels,” HS Ma, AP Roberts, JH Prevost, R Jullien, GW Scherer, *J. Non-Cryst. Solids* (2000) 277, 127
- [42] “Mechanical behavior of ultralow-dielectric-constant mesoporous amorphous silica,” MR Gungor, JJ Watkins, D Maroudas, *Appl. Phys. Lett.* (2008) 92, 251903



- 
- [43] “High specific strength and stiffness structures produced using selective laser melting,” VJ Challis, X Xu, LC Zhang, AP Roberts, JF Grotowski, TB Sercombe, *Mater. Des.*, (2014) 63, 783
- [44] “Elastic properties of graphene nanomeshes,” C Carpenter, AM Christmann, L Hu, I Fampiou, AR Muniz, A Ramasubramaniam, D Maroudas, *Appl. Phys. Lett.* (2014) 104, 141911
- [45] “Origami interleaved tube cellular materials,” KC Cheung, T Tachi, S Calisch, K Miura, *Smart Mater. Struct.* (2014) 23, 094012
- [46] “Geometry-induced mechanical properties of carbon nanotube foams,” L Lattanzi, LD Nardo, JR Raney, C Daraio, *Adv. Eng. Mater.* (2014) 116, 1026
- [47] “Reversibly assembled cellular composite materials,” KC Cheung, N Gershesfeld, *Science* (2013) 341, 1219
- [48] “Biomimetic superelastic graphene-based monoliths,” L Qiu, JZ Liu, SLY Chang, YZ Wu, D Li, *Nat. Commun.* (2012) 3, 1241
- [49] “Mechanical behavior of ultralow-dielectric-constant mesoporous amorphous silica,” MR Gungor, JJ Watkins, D Maroudas, *Appl. Phys. Lett.* (2008) 92, 251903
- [50] “Super-compressibility of ultralow-density nanoporous silica,” SO Kucheyev, M Stadermann, SJ Shin, JH Satcher, SA Gammon, SA Letts, T van Buuren, AV Hamza, *Adv. Mater.* (2012) 24, 776
- [51] “Aerographite: ultra-lightweight, flexible nanowall, carbon microtube material with outstanding mechanical performance,” M Mecklenburg, A Schuchardt, YK



- 
- Mishra, S Kaps, R Adelung, A Lotnyk, L Kienle, K Shulte, *Adv. Mater.* (2012) 24, 3486
- [52] “Mechanically robust and electrically conductive carbon nanotube foams,” MA Worsley, SO Kucheyev, JH Satcher, AV Hamza, TF Baumann, *Appl. Phys Lett.* (2009) 94, 073115
- [53] “Nanoengineering mechanically robust aerogels via control of foam morphology,” SO Kucheyev, TF Baumann, CA Cox, YM Wang, JH Satcher, AV Hamza, JE Bradby, *Appl. Phys. Lett.* (2006) 89, 041911
- [54] “Nanoengineering strong silica aerogels,” N Leventis, CS Leventis, GH Zhang, AMM Rawashdeh, *Nano Lett.* (2002) 2, 957
- [55] D. J. Jackson, “Classical Electrodynamics”, Wiley, 1998.
- [56] C. G. Someda, “Electromagnetic Waves”, Taylor & Francis, 2006.
- [57] L. E. Cross, “Relaxor Ferroelectrics,” *Ferroelectrics*, 76, 241–67 (1987).
- [58] S. E. Park and T. R. ShROUT, “Ultrahigh Strain and Piezoelectric Behavior in Relaxor Based Ferroelectric Single Crystals,” *J. Appl. Phys.*, 41, 1804–11 (1997).
- [59] A. A. Bokov and Z. G. Ye, “Recent Progress in Relaxor Ferroelectrics with Perovskite Structure,” *J. Mat. Sci.*, 41, 31–52 (2006).
- [60] H. Fu and R. E. Cohen, “Polarization Rotation Mechanism for Ultrahigh Electromechanical Response in Single-Crystal Piezoelectrics,” *Nature*, 403, 281–3 (2000).
- [61] V. Westphal, W. Kleemann, and M. D. Glinchuk, “Diffuse Phase Transitions and



- 
- Random-Field-Induced Domain States of the ‘Relaxor’ Ferroelectric  $\text{PbMg}_{1/3}\text{Nb}_{2/3}\text{O}_3$ ,” *Phys. Rev. Lett.*, 68, 847–50 (1992).
- [62] B. Noheda, D. E. Cox, G. Shirane, J. Gao, and Z. G. Ye, “Phase Diagram of the Ferroelectric Relaxor  $(1-x)\text{PbMg}_{1/3}\text{Nb}_{2/3}\text{O}_3 - x\text{PbTiO}_3$ ,” *Phys. Rev. B*, 66, 054104–10 (2002).
- [63] R. A. Cowley, S. N. Gvasaliya, S. G. Lushnikov, B. Roessli, and G. M. Rotaru, “Relaxing with Relaxors: A Review of Relaxor Ferroelectrics,” *Adv. Phys.*, 60, 229–327 (2011).
- [64] D. Vieland, W. Wuttig, and L. E. Cross, “The Glassy Behavior of Relaxor Ferroelectrics,” *Ferroelectrics*, 120, 71–7 (1991).
- [65] W. Kleemann, “Random-Field Induced Antiferromagnetic, Ferroelectric and Structural Domain States,” *Int. J. Mod. Phys.*, 7, 2469–507 (1993).
- [66] P. Bonneau, P. Garnier, G. Calvarin, E. Husson, J. R. Gavarri, A. W. Hewat, and A. Morell, “X-ray and Neutron Diffraction Studies of the Diffuse Transition in  $\text{PbMg}_{1/3}\text{Nb}_{2/3}\text{O}_3$  Ceramics,” *J. Solid State Chem.*, 91, 350–61 (1991).
- [67] E. M. Sabolsky, S. Trolier-McKinstry, and G. L. Messing, “Dielectric and Piezoelectric Properties of  $\langle 001 \rangle$  Fiber-Textured  $0.675\text{Pb}(\text{Mg}_{1/3}\text{Nb}_{2/3})\text{O}_3 - 0.325\text{PbTiO}_3$  Ceramics,” *J. Appl. Phys.*, 93, 4072–80 (2003).
- [68] K. Uchino, *Piezoelectric Actuators and Ultrasonic Motors*. Kluwer Academic, Boston, 1996.
- [69] S. E. Park and T. R. Shrout, “Relaxor Based Ferroelectric Single Crystals for Electro-Mechanical Actuators,” *Mater. Res. Innovations*, 1, 20–5 (1997).



- 
- [70] D. Vieland, S. J. Jang, L. E. Cross, and M. Wuttig, “Deviation From Curie-Weiss Behavior in Relaxor Ferroelectrics,” *Phys. Rev. B*, 46, 8003–6 (1992).
- [71] A. K. Tagantsev, “Vogel-Fulcher Relationship for the Dielectric Permittivity of Relaxor Ferroelectrics,” *Phys. Rev. Lett.*, 72, 1100–3 (1994).
- [72] O. Noblanc, P. Gaucher, and G. Calvarin, “Structural and Dielectric Studies of  $\text{Pb}(\text{Mg}_{1/3}\text{Nb}_{2/3})\text{O}_3$ – $\text{PbTiO}_3$  Ferroelectric Solid Solutions Around the Morphotropic Boundary,” *J. Appl. Phys.*, 79, 4291–7 (1996).
- [73] S. Kamba, E. Buixaderas, J. Petzelt, F. Fousek, and J. Nosek, “Infrared and Raman Spectroscopy of  $[\text{Pb}(\text{Zn}_{1/3}\text{Nb}_{2/3})\text{O}_3]_{0.92}$ – $[\text{PbTiO}_3]_{0.08}$  and  $[\text{Pb}(\text{Mg}_{1/3}\text{Nb}_{2/3})\text{O}_3]_{0.71}$ – $[\text{PbTiO}_3]_{0.29}$  Single Crystals,” *J. Appl. Phys.*, 93, 933–8 (2003).
- [74] Y. Wang, Y. L. Cheng, K. C. Cheng, H. L. W. Chan, C. L. Choy, and Z. R. Liu, “In-Plane Dielectric Properties of Epitaxial  $0.65\text{Pb}(\text{Mg}_{1/3}\text{Nb}_{2/3})\text{O}_3$ – $0.35\text{PbTiO}_3$ ,” *Appl. Phys. Lett.*, 85, 1580–2 (2004).
- [75] V. Bovtun, S. Kamba, S. Veljko, D. Nuzhnyy, J. Kroupa, M. Savinov, P. Vanek, J. Petzelt, J. Holc, M. Kosec, H. Amarin, and M. Alguero, “Broad-band Dielectric Spectroscopy of Phonons and Polar Nanoclusters in  $\text{PbMg}_{1/3}\text{Nb}_{2/3}\text{O}_3$ – $35\%\text{PbTiO}_3$ ,” *Phys. Rev. B*, 79, 104111–12 (2009).
- [76] R. K. Zheng, Y. Wang, H. L. W. Chan, C. L. Choy, and H. S. Luo, “Determination of the Strain Dependence of Resistance in  $\text{La}_{0.7}\text{Sr}_{0.3}\text{MnO}_3$ /PMN–PT Using the Converse Piezoelectric Effect,” *Phys. Rev. B*, 75, 212102– (2007).
- [77] Q. M. Zhang, J. Zhao, and L. E. Cross, “Aging of the Dielectric and



- 
- Piezoelectric Properties of Relaxor Ferroelectric Lead Magnesium Niobate-Lead Titanate in the Electric Field Biased State,” *J. Appl. Phys.*, 79, 3181–7 (1996).
- [78] Z. Q. Wu, W. H. Duan, Y. Wang, B. L. Gu, and W. X. Zhang, “Effect of Defect-Induced Internal Field on the Aging of Relaxors,” *Phys. Rev. B*, 67, 052101–4 (2003).
- [79] B. Ferguson and X. C. Zhang, “Materials for Terahertz Science and Technology,” *Nat. Mater.*, 1, 26–33 (2002).
- [80] Y. Lee, *Principles of Terahertz Science and Technology*. Springer, New York, NY, 2009.
- [81] J. Hlinka, T. Ostapchuk, D. Nuzhnyy, J. Petzelt, P. Kuzel, C. Kadlec, P. Vanek, I. Ponomareva, and L. Bellaiche, “Coexistence of the Phonon and Relaxation Soft Modes in the Terahertz Dielectric Response of Tetragonal BaTiO<sub>3</sub>,” *Phys. Rev. Lett.*, 101, 167402–4 (2008).
- [82] M. Misra, K. Kotani, I. Kawayama, H. Murakami, and M. Tonouchi, “Observation of TO 1 Soft Mode in SrTiO<sub>3</sub> Films by Terahertz Time Domain Spectroscopy,” *Appl. Phys. Lett.*, 87, 182909–3 (2005).
- [83] J. Han, F. Wan, Z. Zhu, and W. Zhang, “Dielectric Response of Soft Mode in Ferroelectric SrTiO<sub>3</sub>,” *Appl. Phys. Lett.*, 90, 031104–3 (2007).
- [84] P. Kuzel, F. Kadlec, H. Nemeč, R. Ott, and E. Hollmann, “Dielectric Tunability of SrTiO<sub>3</sub> Thin Films in the Terahertz Range,” *Appl. Phys. Lett.*, 88, 102901–3 (2006).



- 
- [85] V. Skoromets, F. Kadlec, C. Kadlec, H. Nemeč, I. Rychetsky, G. Panaitov, V. Müller, D. Fattakhova-Rohlfing, P. Moch, and P. Kuzel, “Tuning of Dielectric Properties of SrTiO<sub>3</sub> in the Terahertz Range,” *Phys. Rev. B*, 84, 174121–10 (2011).
- [86] J. Z. Xin, K. L. Jim, J. Yang, X. J. Gong, L. Q. Chen, F. Gao, Y. H. Tsang, H. L. W. Chan, and C. W. Leung, “Strontium Titanate/Silicon-Based Terahertz Photonic Crystal Multilayer Stack,” *Appl. Phys. A*, 107, 109–15 (2012).
- [87] L. Duvillaret, F. Garet, and J. L. Coutaz, “A Reliable Method for Extraction of Material Parameters in Terahertz Time-Domain Spectroscopy,” *IEEE J. Quantum Electron.*, 2, 739–46 (1996).
- [88] D. Zekria, V. A. Shuvaeva, and A. M. Glazer, “Birefringence Imaging Measurements on the Phase Diagram of Pb(Mg<sub>1/3</sub>Nb<sub>2/3</sub>)O<sub>3</sub>–PbTiO<sub>3</sub>,” *J. Phys. Condens. Matter*, 17, 1593–600 (2005).
- [89] L. S. Kamzina, I. P. Raevskii, S. M. Emel’yanov, S. I. Raevskaya, and E. V. Sahkar, “Dielectric and Optical Properties of Pb(Mg<sub>1/3</sub>Nb<sub>2/3</sub>)<sub>0.8</sub>Ti<sub>0.2</sub>O<sub>3</sub>(PMNT<sub>0.2</sub>) Ferroelectric Relaxor Single Crystals,” *Phys. Solid State*, 46, 881–7 (2004).
- [90] J. S. McCloy, K. A. Korolev, Z. Li, M. N. Afsar, and S. K. Sundaram, “Millimeter-Wave Dielectric Properties of Single-Crystal Ferroelectric and Dielectric Materials,” *IEEE Trans. Ultrason. Ferroelectr. Freq. Control*, 58, 18–29 (2011).
- [91] Ozbay E: Plasmonics: merging photonics and electronics at nanoscale dimensions. *Science* 2006, 311:189–193.



- 
- [92] Anker JN, Hall WP, Lyandres O, Shah NC, Zhao J, van Duyne RP: Biosensing with plasmonic nanosensors. *Nat Mater* 2008, 7:442–453.
- [93] Mayer KM, Hafner JH: Localized surface plasmon resonance sensors. *Chem Rev* 2011, 111:3828–3857.
- [94] Sherry LJ, Chang SH, Schatz GC, van Duyne RP: Localized surface plasmon resonance spectroscopy of single silver nanocubes. *Nano Lett* 2005, 5:2034–2038.
- [95] Lee KS, El-Sayed MA: Gold and silver nanoparticles in sensing and sensitivity of plasmon response to size, shape, and metal composition. *J Phys Chem B* 2006, 110:19220–19225.
- [96] Nehl CL, Liao H, Hafner JH: Optical properties of star-shaped gold nanoparticles. *Nano Lett* 2006, 6:683–688.
- [97] Chen H, Kou X, Yang Z, Ni W, Wang J: Shape- and size-dependent refractive index sensitivity of gold nanoparticles. *Langmuir* 2008, 24:5233–5237.
- [98] Burgin J, Liu M, Guyot-Sionnest P: Dielectric sensing with deposited gold bipyramids. *J Phys Chem C* 2008, 112:19279–19282.
- [99] Barbosa S, Agrawal A, Rodríguez-Lorenzo L, Pastoriza-Santos I, Alvarez-Puebla RA, Kornowski A, Weller H, Liz-Marzán M: Tuning size and sensing properties in colloidal gold nanostars. *Langmuir* 2010, 26:14943–14950.
- [100] Grzelczak M, Pérez-Juste J, Mulvaney P, Liz-Marzán LM: Shape control in gold nanoparticle synthesis. *Chem Soc Rev* 2008, 37:1783–1791.
- [101] Huang X, Neretina S, El-Sayed MA: Gold nanorods: from synthesis and



- 
- properties to biological and biomedical applications. *Adv Mater* 2009, 21:4880–4910.
- [102] Yu X, Lei DY, Amin F, Hartmann R, Acuna GP, Guerrero-Martínez A, Maier SA, Tinnefeld P, Carregal-Romero S, Parak WJ: Distance control in-between plasmonic nanoparticles via biological and polymeric spacers. *Nano Today* 2013, 8:480–493.
- [103] Ameling R, Langguth L, Hentschel M, Mesch M, Braun PV, Giessen H: Cavity-enhanced localized plasmon resonance sensing. *Appl Phys Lett* 2010, 97:253116.
- [104] Schmidt MA, Lei DY, Wondraczek L, Nazabal V, Maier SA: Hybrid nanoparticle-microcavity-based plasmonic nanosensors with improved detection resolution and extended remote-sensing ability. *Nat Commun* 2012, 3:1108.
- [105] Tsai CY, Lu SP, Lin JW, Lee PT: High sensitivity plasmonic index sensor using slablike gold nanoring arrays. *Appl Phys Lett* 2011, 98:153108.
- [106] Rodríguez-Fortuño FJ, Martínez-Marco M, Tomás-Navarro B, Ortuño R, Martí, J, Martínez A, Rodríguez-Cantó: High-sensitive chemical detection in the infrared regime using plasmonic gold nanocrosses. *Appl Phys Lett* 2011, 98:133118.
- [107] Evlyukhin AB, Reinhardt C, Zywietz U, Chichkov BN: Collective resonances in metal nanoparticle arrays with dipole-quadrupole interactions. *Phys Rev B* 2012, 85:245411.



- 
- [108] Luk'yanchuk B, Zheludev NI, Maier SA, Halas NJ, Nordlander P, Giessen H, Chong CT: The Fano resonance in plasmonic nanostructures and metamaterials. *Nat Mater* 2010, 9:707–715.
- [109] Leveque G, Martin OJF: Optical interactions in a plasmonic particle coupled to a metallic film. *Opt Express* 2006, 14:9971.
- [110] Ye J, Shioi M, Lodewijks K, Lagae L, Kawamura T, Van Dorpe P: Tuning plasmonic interaction between Au nanorings and a gold film for surface-enhanced Raman scattering. *Appl Phys Lett* 2010, 97:163106.
- [111] Knight MW, Halas NJ: Nanoshells to nanoeggs to nanocups: optical properties of reduced symmetry core-shell nanoparticles beyond the quasistatic limit. *New J Phys* 2008, 10:105006.
- [112] Lei DY, Fernández-Domínguez AI, Sonnefraud Y, Appavoo K, Haglund RF, Pendry JB, Maier SA: Revealing plasmonic gap modes in particle-on-film systems using dark-field spectroscopy. *ACS Nano* 2012, 6:1380–1386.
- [113] Zhan Y, Lei DY, Li X, Maier SA: Plasmonic Fano resonances in nanohole quadrumers for ultra-sensitive refractive index sensing. *Nanoscale* 2014. doi:10.1039/C3NR06024A.
- [114] Johnson PB, Christy RW: Optical constants of the noble metals. *Phys Rev B* 1972, 6:4370–4379.
- [115] Miller MM, Lazarides AA: Sensitivity of metal nanoparticle surface plasmon resonance to the dielectric environment. *J Phys Chem B* 2005, 109:21556–21565.



- 
- [116] Jakab A, Rosman C, Khalayka Y, Becker J, Trügler A, Hohenester U, Sönnichsen C: High sensitivity plasmonic silver nanorods. *ACS Nano* 2011, 5:6880–6885.
- [117] Yu Z, Fan S: Extraordinarily high spectral sensitivity in refractive index sensors using multiple optical modes. *Opt Express* 2011, 19:10029–10040.
- [118] Hu M, Novo C, Funston A, Wang H, Staleva H, Zou S, Mulvaney P, Xia Y, Hartland GV: Dark-field microscopy studies of single metal nanoparticles: understanding the factors that influence the linewidth of the localized surface plasmon resonance. *J Mater Chem* 2008, 18:1949–1960.
- [119] Lei DY, Wan JTK, Ong HC: Numerical and analytical evaluations of the sensing sensitivity of waveguide mode in one-dimensional metallic gratings. *Nanotechnology* 2012, 23:275501